HU-EP-09/25
MPP-2009-153
PSI-PR-09-11
SFB/CPP-09-45

NLO QCD corrections to $pp/p\bar{p} \to WW + jet + X$ including leptonic W-boson decays

S. Dittmaier[1,2], S. Kallweit[2,3] and P. Uwer[4]

[1] *Albert-Ludwigs-Universität Freiburg, Physikalisches Institut, D-79104 Freiburg, Germany*

[2] *Max-Planck-Institut für Physik (Werner-Heisenberg-Institut), D-80805 München, Germany*

[3] *Paul Scherrer Institut, Würenlingen und Villigen, CH-5232 Villigen PSI, Switzerland*

[4] *Institut für Physik, Humboldt-Universität zu Berlin, D-10099 Berlin, Germany*

Abstract: We report on the calculation of the next-to-leading order QCD corrections to the production of W-boson pairs in association with a hard jet at the Tevatron and the LHC, which is an important source of background for Higgs and new-physics searches. Leptonic decays of the W bosons are included by applying an improved version of the narrow-width approximation that treats the W bosons as on-shell particles, but keeps the information on the W spin. Contributions from external bottom quarks are neglected, because they are either numerically suppressed or should be attributed to different processes such as Wt or $t\bar{t}$ production. A survey of differential NLO QCD cross sections is provided both for the LHC and the Tevatron. The QCD corrections stabilize the leading-order prediction for the cross section with respect to scale variations. However, the scale dependence of the next-to-leading order results for the LHC is only reduced considerably if a veto against the emission of a second hard jet is applied. In general, the corrections do not simply rescale the differential leading-order cross sections. In particular, their shapes are distorted if an additional energy scale is involved.

August 2009

1 Introduction

The search for new-physics particles—including the Standard Model Higgs boson—will be the primary task in high-energy physics in the era of the LHC. The extremely complicated hadron collider environment does not only require sufficiently precise predictions for new-physics signals, but also for many complicated background reactions that cannot entirely be measured from data. Among such background processes, several involve three, four, or even more particles in the final state, rendering the necessary next-to-leading-order (NLO) calculations in QCD very complicated. This problem lead to the creation of an "experimenters' wishlist for NLO calculations" [1–3] that were still missing at that time, but are required for successful LHC analyses. The process $pp \to W^+W^-+\text{jet}+X$ made it to the top of this list. Meanwhile the $2 \to 3$ particle processes on the list have been evaluated at NLO QCD, and we further contribute to and extend that part in this paper; most notably also some of the $2 \to 4$ processes have been calculated to NLO recently, viz. for the production of $t\bar{t}b\bar{b}$ [4] and $W+3\text{jets}$ final states [5]. Moreover, benchmark results for the virtual corrections have been presented for a specific phase-space point for all $2 \to 4$ processes on the list in Ref. [6].

The process of WW+jet production is an important source for background to the production of a Higgs boson that subsequently decays into a W-boson pair, where additional jet activity might arise from the production. In particular, it has been shown recently that the sensitivity of the Tevatron experiments CDF and D0 concerning the discovery of a Standard Model Higgs boson in the mass range $135-190\,\text{GeV}$ could improve significantly by studying $H \to W^+W^- \to l^+l^-\not{p}_T$ together with an additional jet [7].

WW+jet production delivers also potential background to new-physics searches, such as supersymmetric particles, because of leptons and missing transverse momentum from the W decays. Besides the process is interesting in its own right, since W-pair production processes enable a direct analysis of the non-abelian gauge-boson self-interactions, and a large fraction of W pairs will show up with additional jet activity at the LHC. Last but not least WW+jet at NLO also delivers the real–virtual contributions to the next-to-next-to-leading-order (NNLO) calculation of W-pair production, for which further building blocks are presented in Ref. [8].

Here we report on the calculation of the process $pp/p\bar{p} \to W^+W^-+\text{jet}+X$ in NLO QCD including leptonic W-boson decays. Results of this calculation on integrated cross sections, which are not sensitive to the W decays, have already been published in Ref. [9]. Parallel to our work, another NLO study [10] of $pp \to W^+W^-+\text{jet}+X$ at the LHC appeared, where also the W decays have been taken into account. Moreover, a third calculation focusing on WW+jet production is still in progress [11]. In Ref. [3] the three different approaches are briefly described, and a detailed comparison of the virtual corrections at a single phase-space point is presented, revealing mutual agreement.

The paper is organized as follows. In Section 2 we describe the general setup of the calculation, paying particular attention to the treatment of the various quark flavours. Section 3 provides details of the NLO calculation, and Section 4 describes the methods to include the W decays. Our detailed discussion of numerical results is presented in Section 5, which covers both integrated and differential cross sections. In Section 6 we give our conclusions, and the Appendix contains a derivation of the improved narrow-width approximation.

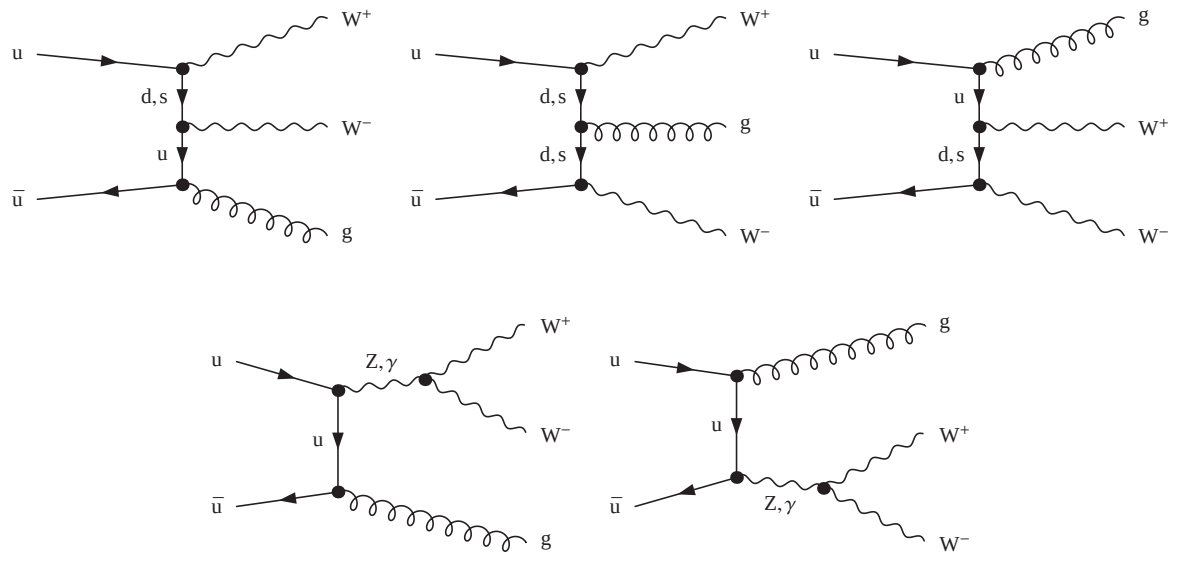

Figure 1: Diagrams contributing to one specific LO subprocess: The two W bosons couple directly to the fermion chain (upper diagrams) or by means of an intermediate neutral gauge boson (lower diagrams).

2 Leading-order calculation and calculational framework

At leading order (LO), hadronic WW+jet production receives contributions from the partonic processes $q\bar{q} \to W^+W^-g$, $qg \to W^+W^-q$, and $g\bar{q} \to W^+W^-\bar{q}$, where q stands for up- or down-type quarks. Note that the amplitudes for $q = u, d$ are not the same, even for vanishing light-quark masses. All three channels are related by crossing symmetry. The LO diagrams for the sample process $u\bar{u} \to W^+W^-g$ are shown in Figure 1.

2.1 Quark-mixing effects

To very good approximation the Cabibbo–Kobayashi–Maskawa (CKM) matrix can be assumed to be of block-diagonal form allowing mixing only between the two light generations, namely

$$V_{\mathrm{CKM}} = \begin{pmatrix} V_{\mathrm{ud}} & V_{\mathrm{us}} & 0 \\ V_{\mathrm{cd}} & V_{\mathrm{cs}} & 0 \\ 0 & 0 & 1 \end{pmatrix} = \begin{pmatrix} \cos\theta_{\mathrm{C}} & \sin\theta_{\mathrm{C}} & 0 \\ -\sin\theta_{\mathrm{C}} & \cos\theta_{\mathrm{C}} & 0 \\ 0 & 0 & 1 \end{pmatrix}, \tag{2.1}$$

where θ_{C} denotes the Cabibbo angle. The approximation is justified by the fact that the neglected off-diagonal matrix elements are very small. Moreover, ignoring the masses of the light quarks, the dependence on the CKM matrix drops out for a remarkable set of subprocesses. For $pp/p\bar{p} \to WW + \mathrm{jet} + X$, this happens if both W bosons couple to the same fermion chain, as illustrated in Figure 2. Independent of gluonic couplings to this fermion chain, which do not affect the electroweak structure, the unitarity of the CKM matrix leads to

$$\sum_{\mathrm{D=d,s}} V_{\mathrm{U'D}} V^*_{\mathrm{UD}} = \sum_{\mathrm{D=d,s}} V_{\mathrm{U'D}} V^\dagger_{\mathrm{DU}} = \delta_{\mathrm{UU'}}\,, \quad \sum_{\mathrm{U=u,c}} V^*_{\mathrm{UD'}} V_{\mathrm{UD}} = \sum_{\mathrm{U=u,c}} V^\dagger_{\mathrm{D'U}} V_{\mathrm{UD}} = \delta_{\mathrm{DD'}}\,, \tag{2.2}$$

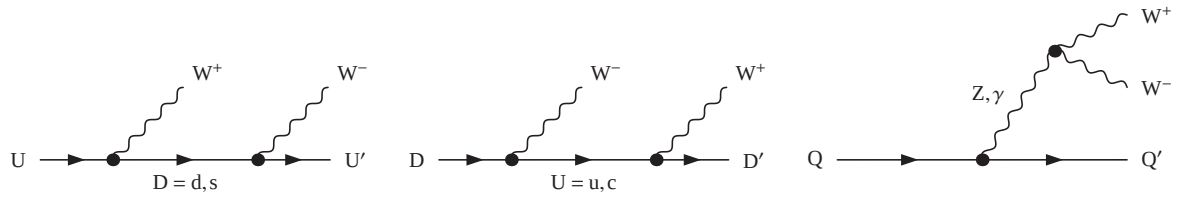

Figure 2: Electroweak part of diagrams with two W bosons coupling directly to the same fermion chain (left and central diagram): With light-quark masses neglected, all contributions with $U \neq U'$ or $D \neq D'$ vanish in the block-diagonal approximation of the CKM matrix due to cancellations between diagrams with different intermediate states. The contributions with $U = U'$ or $D = D'$ behave as in the case of a trivial (unit) CKM matrix. Diagrams with an intermediate neutral electroweak vector boson (right diagram) do not depend on the CKM matrix, and thus $Q = Q'$ holds.

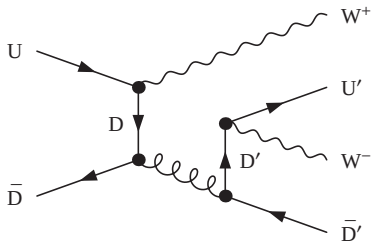

Figure 3: A sample diagram with two W bosons coupling to different fermion chains: Contributions of this kind yield a non-trivial dependence on the CKM matrix elements.

with the nomenclature of Figure 2, when the intermediate quark state is summed over. Diagrams with the W-boson pair coupling to the fermion chain by means of an intermediate vector boson are independent of the CKM matrix anyway. Therefore, a remarkable set of subprocesses of $pp/p\bar{p} \to WW + \text{jet} + X$ is not influenced by the explicit entries of the CKM matrix due to its unitarity.

The only subprocesses contributing to $pp/p\bar{p} \to WW + \text{jet} + X$ that depend on the explicit entries of the CKM matrix are those containing two fermion chains with the two W bosons coupling to different fermion chains at least in some diagrams. These are the real-emission subprocesses including both two external up-type and two down-type (anti-)quarks. A sample diagram is shown in Figure 3.

2.2 Treatment of bottom (anti-)quarks

The situation of a hard jet resulting from an outgoing bottom (anti-)quark has to be considered with care: The long bottom lifetime results in a resolvable second vertex that is displaced from the primary interaction point, allowing in principle to tag the bottom flavour. This, however, does not imply that all events involving outgoing bottom quarks can be separated. For instance, in real-emission subprocesses only one of the two outgoing jets must be detected: This can be the light jet as well, while the b-jet leaves the detector unseen in direction of the beam axis. Moreover, the b-tagging efficiency is below 100%, so that not all "b-jet events"

can be isolated. The influence of incoming bottom (anti-)quarks on the hadronic cross section is suppressed with respect to other incoming (anti-)quarks by the small bottom PDFs in the colliding hadrons.

In the process class $pp/p\bar{p} \to WW + jet + X$, however, the suppression of subprocesses with external bottom (anti-)quarks may be overcompensated by top resonances, always showing up along with final-state bottom (anti-)quarks. Moreover, outgoing $b\bar{b}$ pairs appearing in real-emission subprocesses even contain two potentially resonant top-quark propagators in some diagrams without PDF suppression. These subprocesses should, however, in general not be assigned to WW+jet production, since they are actually off-shell continuations of $t\bar{t}$ production. From this point of view, the subprocesses with only one outgoing bottom (anti-)quark can be seen as contributions to W^-t production or $W^+\bar{t}$ production, with the off-shell decay of the top (anti-)quark included. In our approach, precisely described in the following, we exclude these resonance reactions upon omitting contributions from channels involving external bottom (anti-)quarks. Thus, if desired, contributions from these channels could be easily added, but their calculation requires a consistent treatment of top (anti-)quarks as unstable particles, as for instance provided by the complex-mass scheme [19, 20].

For the calculation of cross sections, we follow two different strategies regarding the treatment of bottom (anti-)quarks:

(i) Five-flavour scheme

In the first approach, bottom (anti-)quarks are treated as massless particles, so five-flavour PDFs and a five-flavour running of α_s are used. In this framework, the strategy is to neglect all contributions containing external bottom (anti-)quarks. For the initial state, this approach is justified by the smallness of their PDFs. Final-state bottom (anti-)quarks are excluded by the assumption that their signal can be distinguished from that of a light-quark jet by means of b-tagging.

An advantage of this procedure can be seen in the fact that the influence of the off-shell continuations of $t\bar{t}$, W^-t, and $W^+\bar{t}$ production, which is explained in the foregoing passage, is simply left away. The respective contributions should be added to dedicated calculations for these processes. Note, however, that the naive application of this procedure would lead to an ill-defined cross section containing mass singularities. The problem is due to the $g \to b\bar{b}$ splitting which by anti-b-tagging would be removed from the real corrections. This contribution is required to cancel the mass singularities from the bottom-quark loop in the gluon self-energy contributing to the virtual corrections. We treat this case similar to what has been done in Ref. [21] and is also discussed in Ref. [22]. If the two bottom quarks are combined according to the applied jet algorithm the resulting jet carries no (net) b-charge and is thus counted as a "light" jet. On the other hand if the two bottom quarks form two individual jets we assume them as tagged and ignore this configuration. Applying this procedure restricts the phase-space integration to the collinear configurations which are needed to cancel the mass singularities in the virtual corrections. Within the dipole subtraction formalism we combine the corresponding integrated dipoles with the virtual corrections to obtain a finite result. In addition one obtains a contribution from the real matrix element with the unintegrated dipoles subtracted. However this contribution is only integrated over the collinear phase space region. Since in this region the unintegrated dipoles approximate the real matrix elements we can ignore this contribution to very good approximation. The case in which the bottom-quark pair is not produced via gluon

splitting is highly suppressed by anti-b-tagging. The neglected contribution only delivers sizeable contributions from diagrams including resonant top quarks. Exactly these contributions, however, are meant to be left out, because they should actually be assigned to different process classes.

(ii) "Four-flavour scheme"

In the second approach, the bottom (anti-)quarks are understood as massive particles. We use four-flavour PDF's to describe the parton contents of the proton. Here, no top resonances show up, since no bottom-(anti-)quark densities are taken into account and no mixing between the two light and the third generation takes place in the chosen approximation of the CKM matrix. As a consequence no single outgoing bottom (anti-)quarks appear. No $\mathrm{b\bar{b}}$ pairs are taken into account in final states which is justified by assuming anti-b-tagging. The running of α_s is driven only by the four remaining light quarks with both bottom- and top-quark loops in the gluon self-energies subtracted at zero momentum. As explained in Section 3, no large corrections arise from terms proportional to $\alpha_\mathrm{s} \ln m_\mathrm{b}$, because counterterms always contribute in the combination $\frac{1}{2}\delta Z_\mathrm{A} + \delta Z_{g_\mathrm{s}}$. Thus, the $\alpha_\mathrm{s} \ln m_\mathrm{b}$ term from the renormalization of the strong coupling cancels against the corresponding term from the wave-function renormalization of the gluon. In this scheme, such a cancellation always takes place if the number of external gluons is equal to the number of strong couplings in the considered LO process.

3 Details of the NLO calculation

In order to prove the correctness of our results we have evaluated each ingredient twice using independent calculations based—as far as possible—on different methods, yielding results in mutual agreement.

3.1 Virtual corrections

The virtual corrections modify the partonic processes that are already present at LO. At NLO these corrections are induced by self-energy, vertex, box (4-point), and pentagon (5-point) corrections. For illustration the pentagon graphs, which are the most complicated diagrams, are shown in Figure 4 for one partonic channel. At one-loop level WW+jet production also serves as an off-shell continuation of the loop-induced process of Higgs+jet production with the Higgs boson decaying into a W-boson pair. In these diagrams the off-shell Higgs boson is coupled via a heavy-quark loop to two gluons; the graphs for this mechanism are shown in Figure 5 together with vertex-correction diagrams with an intermediate electroweak vector boson. The Higgs resonance is included in our calculation upon employing a fixed decay width Γ_H, i.e. by replacing the propagator denominator $(p_\mathrm{H}^2 - M_\mathrm{H}^2)$ by $(p_\mathrm{H}^2 - M_\mathrm{H}^2 + \mathrm{i}M_\mathrm{H}\Gamma_\mathrm{H})$, where p_H and M_H denote the momentum and the mass of the Higgs boson. The box contributions to the fermionic corrections are depicted in Figure 6.

An on-shell renormalization is performed for the wave functions of the external QCD partons and an $\overline{\mathrm{MS}}$ renormalization for the strong coupling with the massive-quark loops in the

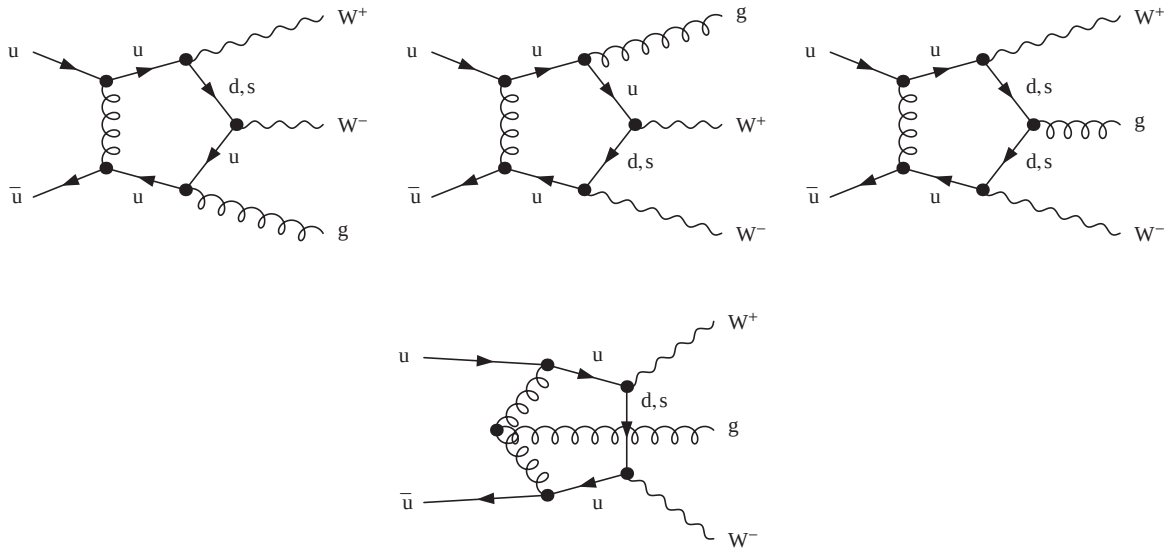

Figure 4: Pentagon diagrams for $u\bar{u} \to W^+W^-g$.

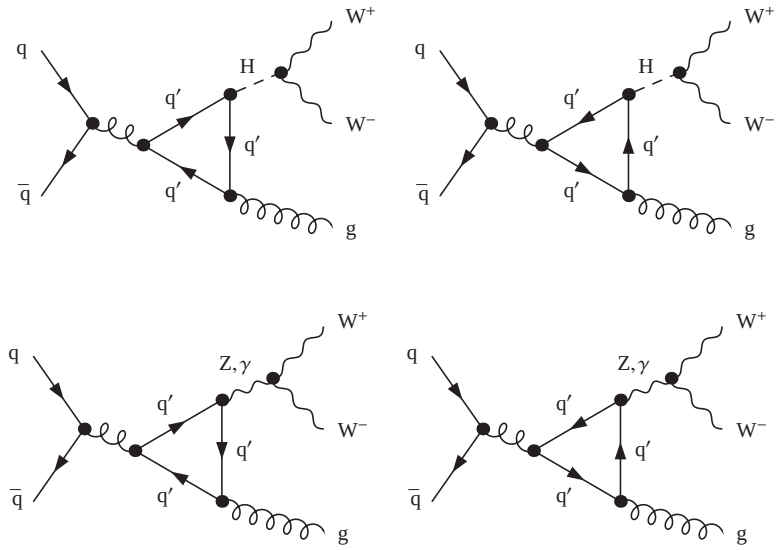

Figure 5: Fermionic vertex-correction diagrams with intermediate electroweak bosons for $q\bar{q} \to W^+W^-g$.

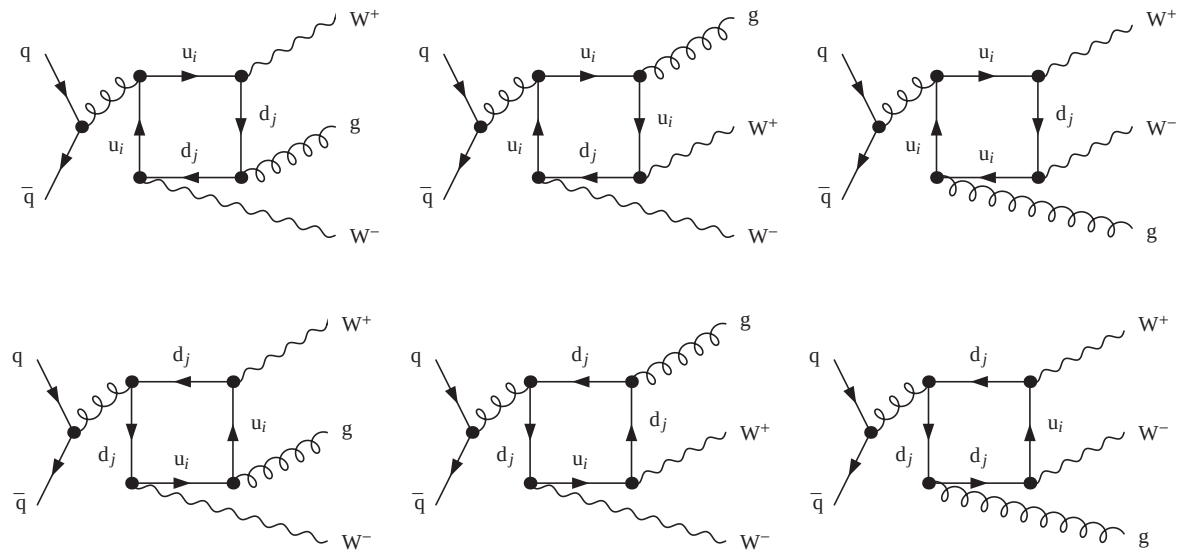

Figure 6: Fermionic box diagrams for $q\bar{q} \to W^+W^-g$.

gluon self-energy subtracted at zero momentum. Since only massless external quarks are involved, the whole counterterm amplitude can be written as

$$\mathcal{M}_{\rm ct} = \left(\delta Z_{\rm q} + \frac{1}{2}\delta Z_{\rm A} + \delta Z_{g_{\rm s}} \right) \mathcal{M}_{\rm LO} \,, \tag{3.1}$$

where the renormalization constants are calculated as follows,

$$\delta Z_{\rm q} = -\frac{\alpha_{\rm s}}{3\pi} \left[\Delta_1^{\rm UV}(\mu) - \Delta_1^{\rm IR}(\mu) \right] \,, \tag{3.2}$$

$$\delta Z_{\rm A} = -\frac{\alpha_{\rm s}}{2\pi} \left[\left(\frac{N_{\rm f}}{3} - \frac{5}{2} \right) \left(\Delta_1^{\rm UV}(\mu) - \Delta_1^{\rm IR}(\mu) \right) + \frac{1}{3} \sum_{\substack{\rm q \\ m_{\rm q} \neq 0}} \left(\Delta_1^{\rm UV}(\mu) + \ln \frac{M_{\rm W}^2}{m_{\rm q}^2} \right) \right] , \tag{3.3}$$

$$\delta Z_{g_{\rm s}} = \frac{\alpha_{\rm s}}{4\pi} \left[\left(\frac{N_{\rm f}}{3} - \frac{11}{2} \right) \left(\Delta_1^{\rm UV}(\mu) - \ln \frac{\mu_{\rm ren}^2}{M_{\rm W}^2} \right) + \frac{1}{3} \sum_{\substack{\rm q \\ m_{\rm q} \neq 0}} \left(\Delta_1^{\rm UV}(\mu) + \ln \frac{M_{\rm W}^2}{m_{\rm q}^2} \right) \right] . \tag{3.4}$$

The sum over q runs over all massive quarks, namely q = t in the five-flavour scheme ($N_{\rm f} = 5$) and q = b, t in the four-flavour scheme ($N_{\rm f} = 4$). Both UV and IR (soft and collinear) divergences are regularized in $D = 4 - 2\epsilon$ dimensions, and the divergences arising as poles in ϵ are quantified by

$$\Delta_k(\mu) = \left(\frac{4\pi\mu^2}{M_{\rm W}^2} \right)^{\epsilon} \frac{\Gamma(1+\epsilon)}{\epsilon^k}, \qquad k = 1, 2, \tag{3.5}$$

where μ is the arbitrary reference scale of dimensional regularization. Superscripts "UV" or "IR" on $\Delta_k(\mu)$ indicate the origin of the divergences.

As is well known, the use of the Dirac matrix γ_5 deserves some care within dimensional regularization, because the Dirac algebra with γ_5 does not admit a straightforward analytical

continuation to $D \neq 4$ dimensions. In both calculations of the virtual corrections we use a simple recipe with a γ_5 that anticommutes with all other Dirac matrices but nevertheless obeys the usual trace relations from four dimensions.[1] Although this approach is, of course, not fully consistent from the mathematical point of view, it is well known that it delivers the correct results at NLO as long as closed fermions loops are calculated "generically", i.e. they are calculated for general fermion flavours followed by a subsequent summation over all fermions by only changing the quantum numbers. The arguments supporting this scheme in the presence of UV divergences can be found in Ref. [41] (see also references therein). In view of dimensionally regularized IR divergences, the situation is much simpler because of their factorization off tree-level structures. As long as it is guaranteed that these residual tree structures are treated in the same way in the virtual and real corrections, between which the cancellations of IR divergences take place, the IR-finite sum is well defined. In fact for the compensation of IR divergences no (anti-)commutation rules involving γ_5 are needed at all. Since the naive scheme described above does not induce any spurios terms from the regularization, it automatically delivers the correct IR-finite sum of virtual and real corrections.

Version 1 of the virtual corrections is essentially obtained as for the related processes of $t\bar{t}H$ [23] and $t\bar{t}$+jet [24] production. Feynman diagrams and amplitudes are generated with *FeynArts* 1.0 [25] and further processed with in-house *Mathematica* routines, which automatically create an output in *Fortran*. The IR divergences (soft and collinear) are analytically separated from the finite remainder in terms of triangle subdiagrams, as described in Refs. [23, 26]. This separation, in particular, allows for a transparent evaluation of so-called rational terms that originate from D-dependent terms multiplying IR divergences, which appear as single or double poles in ϵ. As generally shown in Ref. [4], after properly separating IR from UV divergences such rational terms originating from IR divergences completely cancel; this general result is confirmed in our explicit calculation. For the results presented in Ref. [9], the pentagon tensor integrals were directly reduced to box integrals following Ref. [27], while box and lower-point integrals were reduced à la Passarino–Veltman [28] to scalar integrals. This procedure completely avoids inverse Gram determinants of external momenta in the reduction step from 5-point to 4-point integrals, but the reduction of box and lower-point tensor integrals involves such inverse determinants via the Passarino–Veltman algorithm. Although these inverse determinants jeopardize the numerical stability in regions where such determinants are small, sufficient numerical stability was already achieved. Meanwhile the tensor reduction has been further improved using the methods of Ref. [32]. In detail the reduction of pentagons is performed by the more recent procedure of Ref. [32] (similar to a method proposed in Ref. [33]), and the Passarino–Veltman reduction for 4-point integrals, etc., is supplemented by the dedicated expansions for small Gram and kinematical determinants in the regions where these determinants become small.[2] The scalar one-loop integrals are either calculated analytically or using the results of Refs. [29–31].

Version 2 of the evaluation of loop diagrams starts with the generation of diagrams and amplitudes via *FeynArts* 3.4 [35] which are then further manipulated with *FormCalc* 6.0 [36] and eventually automatically translated into *Fortran* code. The whole reduction of tensor to

[1] The authors of Ref. [11] adopted the more rigorous, but cumbersome approach of 't Hooft and Veltman [40], where γ_5 is split into an anticommuting four-dimensional part and a commuting remainder, and find full agreement with our result (see also Ref. [3] for some details).

[2] Similar procedures based on expansions in small determinants have also been proposed in Ref. [34].

scalar integrals is done with the help of the *LoopTools* library [36], which employs the method of Ref. [27] for the 5-point tensor integrals, Passarino–Veltman [28] reduction for the lower-point tensors, and the *FF* package [37, 38] for the evaluation of regular scalar integrals. The dimensionally regularized soft or collinear singular 3- and 4-point integrals had to be added to this library. To this end, the explicit results of Ref. [26] for the vertex and of Ref. [39] for the box integrals (with appropriate analytical continuations) are taken. Actually the *FormCalc* package assumes a four-dimensional regularization scheme for IR divergences (such as the concept of an infinitesimal photon mass in QED), i.e. rational terms of IR origin are neglected by *FormCalc*. However, as mentioned above, in Ref. [4] it was generally shown that such rational terms consistently cancel if UV and IR divergences are properly separated. Owing to this property the algebraic result of *FormCalc* for the unrenormalized amplitudes could be used without any modification, apart from supplementing the needed IR-singular scalar integrals.

3.2 Real corrections

The matrix elements for the real corrections are given by the processes $0 \to W^+W^-q\bar{q}gg$ and $0 \to W^+W^-q\bar{q}q'\bar{q}'$ with a large variety of flavour insertions for the light quarks q and q′. The partonic processes are obtained from these matrix elements by all possible crossings of quarks and gluons into the initial state. The evaluation of the real-emission amplitudes is performed in two independent ways. Both evaluations employ (independent implementations of) the dipole subtraction formalism [42] for the extraction of IR singularities and for their combination with the virtual corrections.

Version 1 employs the Weyl–van-der-Waerden formalism (as described in Ref. [43]) for the calculation of the helicity amplitudes. The phase-space integration is performed by a multi-channel Monte Carlo integrator [44] with weight optimization [45] written in *C++*, which is constructed similar to *RacoonWW* [19,46]. The results for cross sections with two resolved hard jets have been checked against results obtained with *Whizard* 1.50 [47] and *Sherpa* 1.0.8 [48]. Details on this part of the calculation can be found in Ref. [49]. In order to improve the integration, additional channels are included for the integration of the difference of the real-emission matrix elements and the subtraction terms.

Version 2 is based on scattering amplitudes calculated with *Madgraph* [50] generated code. The code has been modified to allow for a non-diagonal quark mixing matrix and the extraction of the required colour and spin structures. The latter enter the evaluation of the dipoles in the Catani–Seymour subtraction method. The evaluation of the individual dipoles was performed using a *C++* library developed during the calculation of the NLO corrections for $t\bar{t}$+jet [24]. For the phase-space integration a simple mapping has been used where the phase space is generated from a sequential splitting.

In the Catani–Seymour dipole subtraction formalism all the IR divergent pieces with LO kinematics are collected in the so-called $\mathcal{I}$-operator—for details we refer to Ref. [42]. Since the IR finiteness of the virtual corrections combined with the IR singularities obtained from the real corrections provides an important check of the calculation, we reproduce here the explicit form of the $\mathcal{I}$-operator,

$$\mathcal{I}(p_a,p_b;\ldots,p_i) = \int_1 d\sigma^{\mathrm{A}}_{ab}(p_a,p_b;\ldots p_i) = -\frac{\alpha_{\mathrm{s}}}{2\pi}\,\overline{|\mathcal{A}_{\mathrm{LO},ab}(p_a,p_b;\ldots,p_i)|^2}$$

$$
\begin{aligned}
&\times\Bigg\{-4T_{\mathrm{R}}C_{\mathrm{A}}\left[4\Delta_2^{\mathrm{IR}}(\mu)+2\Delta_1^{\mathrm{IR}}(\mu)\left(\frac{10}{3}-\ln\frac{2p_ap_i}{M_{\mathrm{W}}^2}-\ln\frac{2p_bp_i}{M_{\mathrm{W}}^2}\right)\right.\\
&\qquad\left.+\ln^2\frac{2p_ap_i}{M_{\mathrm{W}}^2}+\ln^2\frac{2p_bp_i}{M_{\mathrm{W}}^2}-\frac{10}{3}\left(\ln\frac{2p_ap_i}{M_{\mathrm{W}}^2}+\ln\frac{2p_bp_i}{M_{\mathrm{W}}^2}\right)+\frac{190}{9}-\frac{8\pi^2}{3}\right]\\
&\quad+4T_{\mathrm{R}}(C_{\mathrm{A}}-2C_{\mathrm{F}})\left[2\Delta_2^{\mathrm{IR}}(\mu)+\Delta_1^{\mathrm{IR}}(\mu)\left(3-2\ln\frac{2p_ap_b}{M_{\mathrm{W}}^2}\right)+\ln^2\frac{2p_ap_b}{M_{\mathrm{W}}^2}-3\ln\frac{2p_ap_b}{M_{\mathrm{W}}^2}+10-\frac{4\pi^2}{3}\right]\\
&\quad-4T_{\mathrm{R}}^2N_f\left[-\frac{4}{3}\Delta_1^{\mathrm{IR}}(\mu)+\frac{2}{3}\left(\ln\frac{2p_ap_i}{M_{\mathrm{W}}^2}+\ln\frac{2p_bp_i}{M_{\mathrm{W}}^2}\right)-\frac{32}{9}\right]\Bigg\}+\mathcal{O}(\epsilon),
\end{aligned}
\tag{3.6}
$$

where $\mathcal{A}_{\mathrm{LO},ab}$ denotes the colour-stripped LO amplitude for the incoming quark–antiquark pair ab and the outgoing gluon i. Due to the simple colour structure the $\mathcal{I}$-operator does not involve non-trivial colour correlations. The $\mathcal{I}$-operators for the remaining subprocesses are obtained by exchanging the respective momenta and using the crossed matrix elements.

4 Inclusion of gauge-boson decays

Since the produced W bosons are unstable particles, their decays should be included into the analysis. In this context, especially the case of both gauge bosons decaying leptonically is of interest due to its clean signature in the detector. Therefore, only leptonic gauge-boson decays are considered here. The inclusion of the decays is performed following three different strategies for the LO processes, which are presented in the following paragraphs. The improved narrow-width approximation—the on-shell approximation together with the exact treatment of the W-polarization—delivers an appropriate compromise between the complexity of the calculations and the accuracy of the results, which is demonstrated in a comparison of LO results presented in Section 5.3.1. Therefore, the NLO calculation is performed by means of the improved narrow-width approximation.

4.1 Full calculation with off-shell W bosons

The diagrams contributing to $\mathrm{pp/p\bar{p}}\to\ell\bar{\ell}'\nu_{\ell'}\bar{\nu}_\ell+\mathrm{jet}+\mathrm{X}$ can be subdivided into two classes, namely diagrams showing two gauge-boson propagators that can become resonant and other diagrams containing only one W resonance. The doubly-resonant diagrams comprise all the WW+jet-production diagrams of Figure 7 with the two massive gauge bosons decaying into leptons.

Aside from this doubly-resonant group, a number of diagrams that in general contain only one possibly resonant gauge-boson propagator contributes. Their topologies are characterized by the situation that one neutral gauge boson decays to a lepton–antilepton pair with the second pair attached to this leptonic fermion chain via a W boson. All diagrams for this configuration are given in Figure 8 for one specific partonic channel. The configuration with both the Z and the W propagator being resonant is kinematically allowed, but does not significantly contribute, since the corresponding phase-space region is too small.

The singularities appearing at the poles of the LO gauge-boson propagators are treated by introducing decay widths in the propagators. More precisely, the gauge-boson widths are intro-

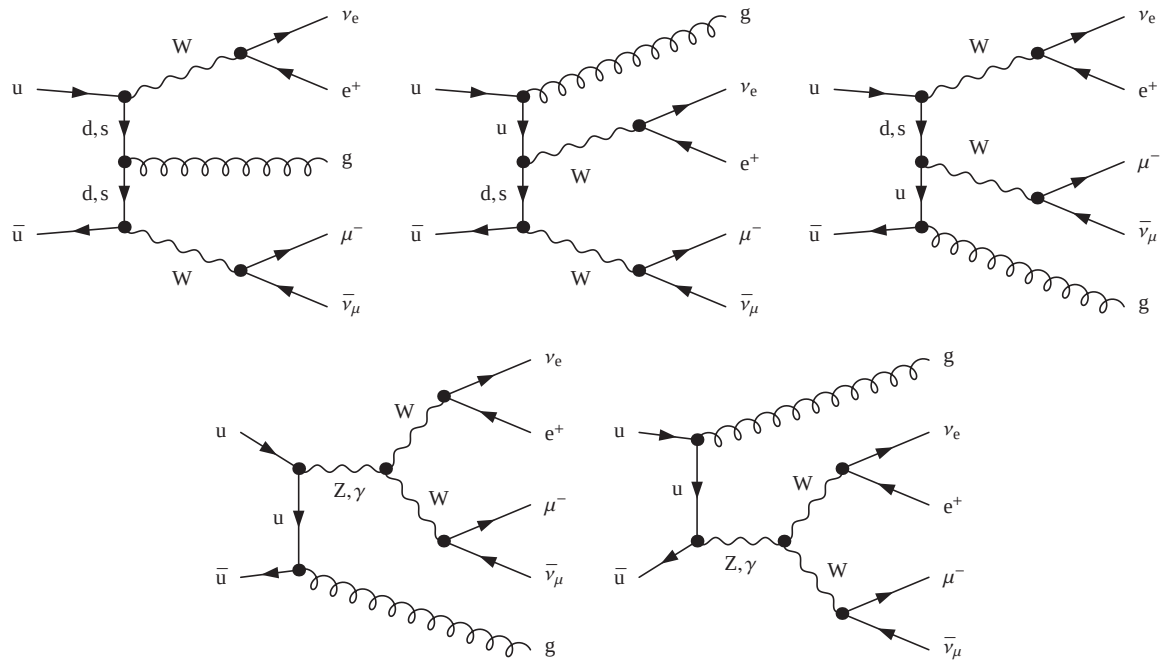

Figure 7: Diagrams with two resonant W propagators in the partonic subprocess $\mathrm{u}\bar{\mathrm{u}} \to \nu_\mathrm{e}\mathrm{e}^+\mu^-\bar{\nu}_\mu\mathrm{g}$.

duced in terms of complex gauge-boson masses according to the complex-mass scheme at LO, which is described in Refs. [19, 20]. Thus, in the LO amplitudes we perform the substitutions

$$M_\mathrm{W}^2 \to M_\mathrm{W}^2 - \mathrm{i}\Gamma_\mathrm{W} M_\mathrm{W}\,, \qquad M_\mathrm{Z}^2 \to M_\mathrm{Z}^2 - \mathrm{i}\Gamma_\mathrm{Z} M_\mathrm{Z}\,. \tag{4.1}$$

To preserve gauge invariance, the gauge-boson masses have to be treated as complex quantities everywhere, in particular in the definition of the weak mixing angle,

$$\cos^2\theta_\mathrm{W} = \frac{M_\mathrm{W}^2}{M_\mathrm{Z}^2} \to \frac{M_\mathrm{W}^2 - \mathrm{i}\Gamma_\mathrm{W} M_\mathrm{W}}{M_\mathrm{Z}^2 - \mathrm{i}\Gamma_\mathrm{Z} M_\mathrm{Z}}\,, \tag{4.2}$$

which renders all couplings complex that are derived from this quantity. The values of the gauge-boson widths are calculated at NLO QCD level with vanishing fermion masses,

$$\Gamma_\mathrm{W} = \frac{\alpha}{6} M_\mathrm{W} \left[\sum_\mathrm{l} (g^-_{\mathrm{W}\nu_\mathrm{l}})^2 + N_\mathrm{c} \sum_{\mathrm{u,d}} (g^-_{\mathrm{Wud}})^2 \left(1 + \frac{\alpha_\mathrm{s}(M_\mathrm{Z})}{\pi}\right)\right], \tag{4.3}$$

$$\begin{aligned}\Gamma_\mathrm{Z} = \frac{\alpha}{6} M_\mathrm{Z} \Bigg[& \sum_\mathrm{l} \left((g^+_{\mathrm{Zll}})^2 + (g^-_{\mathrm{Zll}})^2 + (g^-_{\mathrm{Z}\nu_\mathrm{l}\nu_\mathrm{l}})^2 \right) \\ & + N_\mathrm{c} \sum_{\mathrm{q}\neq\mathrm{t}} \left((g^+_{\mathrm{Zqq}})^2 + (g^-_{\mathrm{Zqq}})^2 \right) \left(1 + \frac{\alpha_\mathrm{s}(M_\mathrm{Z})}{\pi}\right)\Bigg],\end{aligned} \tag{4.4}$$

where $N_\mathrm{c} = 3$ is the number of quark colours and $g^\pm_{\mathrm{V}ff'}$ denote the chiral couplings of $\mathrm{V} = \gamma, \mathrm{Z}, \mathrm{W}$ to the fermions f, f',

$$g^\sigma_{\gamma ff} = -Q_f, \qquad g^\sigma_{\mathrm{Z}ff} = \frac{\delta_{\sigma-} I^3_{\mathrm{W},f} - \sin^2\theta_\mathrm{W} Q_f}{\sin\theta_\mathrm{W}\cos\theta_\mathrm{W}}, \qquad g^\sigma_{\mathrm{W}ff'} = \frac{\delta_{\sigma-}}{\sqrt{2}\sin\theta_\mathrm{W}}. \tag{4.5}$$

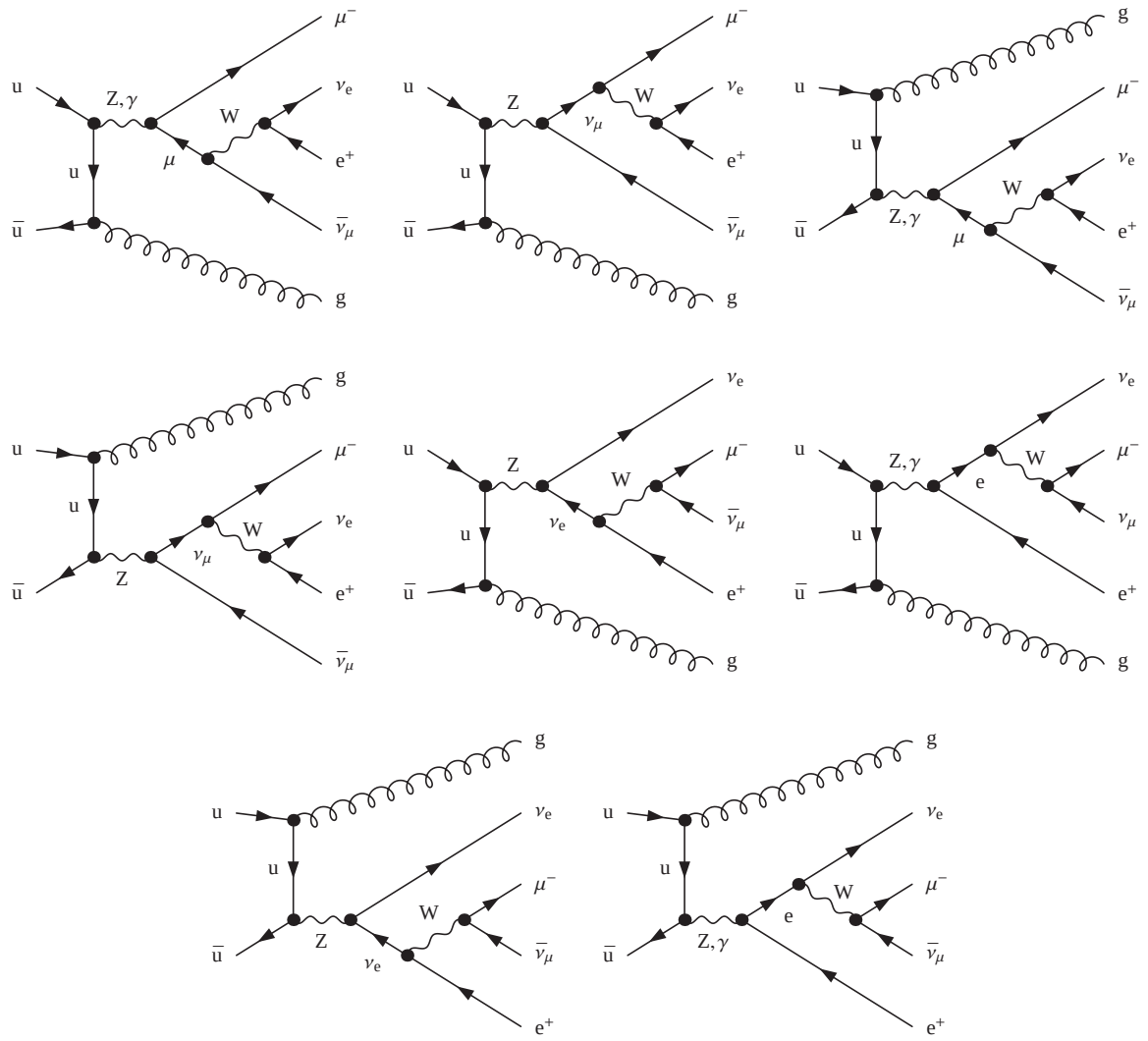

Figure 8: Diagrams with only one resonant W propagator in the partonic subprocess $\mathrm{u}\bar{\mathrm{u}} \to \nu_\mathrm{e}\mathrm{e}^+\mu^-\bar{\nu}_\mu\mathrm{g}$.

Here Q_f and $I^3_{\mathrm{W},f} = \pm\frac{1}{2}$ are the relative electric charge and the third component of the weak isospin of f, respectively. In (4.3), the sums run over all three lepton generations and the two light-quark families, in (4.4) over the three charged leptons and neutrinos and the five light quarks. The W and Z decay widths are calculated using real masses M_W and M_Z, and the strong coupling is set to the measured value $\alpha_\mathrm{s}(M_\mathrm{Z})$ quoted below. Further improvements would go beyond NLO QCD accuracy.

4.2 Narrow-width approximation

In the naive narrow-width approximation (NWA), the produced W bosons are treated as on-shell particles in the production process. The leptonic decays are assumed to be isotropic in the rest frames of the respective W bosons, because their spin information from the production process is dropped. Therefore, the squared matrix elements of the WW+jet-production

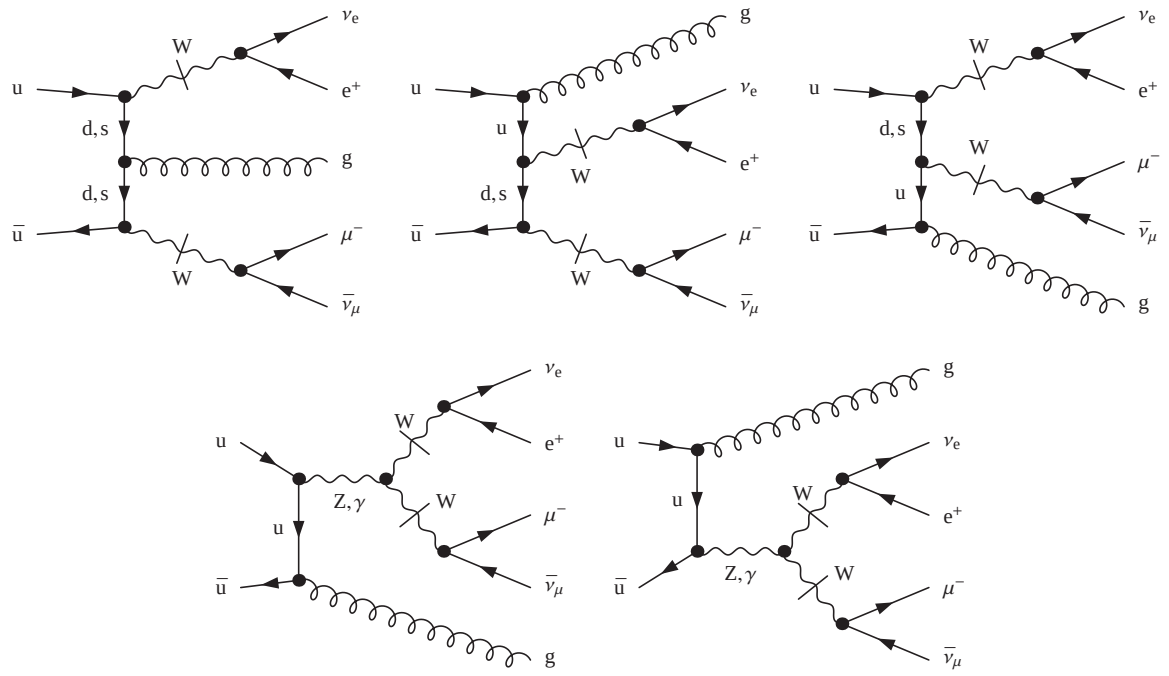

Figure 9: NWA diagrams with two on-shell gauge-boson propagators for the partonic process $u\bar{u} \to \nu_e e^+ \mu^- \bar{\nu}_\mu g$ at LO. The on-shell propagators are denoted by slashed propagator lines.

subprocesses can be used without modifications by only multiplying them with the respective branching ratios for the W-boson decays, which are given by

$$\mathrm{BR}_{\mathrm{W}^+\to\nu_l l^+} = \frac{\Gamma_{\mathrm{W}^+\to\nu_l l^+}}{\Gamma_{\mathrm{W}}}\,, \quad \mathrm{BR}_{\mathrm{W}^-\to l^-\bar{\nu}_l} = \frac{\Gamma_{\mathrm{W}^-\to l^-\bar{\nu}_l}}{\Gamma_{\mathrm{W}}}\,. \tag{4.6}$$

The partial widths for leptonic W decays are

$$\Gamma_{\mathrm{W}^+\to\nu_l l^+} = \Gamma_{\mathrm{W}^-\to l^-\bar{\nu}_l} = \frac{\alpha}{6} M_{\mathrm{W}} (g^{-}_{\mathrm{W}\nu_l l})^2\,, \tag{4.7}$$

since the leptonic decays do not receive NLO QCD corrections.

Consequently, the approximation of on-shell gauge bosons restricts the diagrams contributing to the subprocesses to those containing two resonant W propagators, which stand in one-to-one correspondence to the pure gauge-boson pair-production diagrams in Figure 7. The analogous NWA diagrams are collected in Figure 9 for one LO subprocess.

4.3 Improved narrow-width approximation

In the comparison that is presented in Section 5.3.1 for LO calculations, the naive NWA turns out to be not satisfactory. While the integrated cross sections show modest deviations between the full amplitude calculation and the naive NWA, large discrepancies arise in some phase-space regions if differential cross sections are considered.

An appropriate compromise between the full calculation and the naive NWA is obtained by an improved NWA (iNWA). Here, the gauge bosons are still treated as on-shell particles, but their spin information is kept. It is used to improve the description of the leptonic W-boson decays, which are not isotropic in the respective W-boson rest frames owing to the $V-A$

structure of the decay. Details on how to keep the spin information of the decaying gauge bosons are provided in App. A.

The diagrams that are relevant for the iNWA are the same as for the NWA, which are shown in Figure 9 for one specific channel in LO. The modification of amplitudes is essentially the same for LO subprocesses and all contributions to the NLO QCD cross section: the polarization vector of each of the outgoing gauge bosons is replaced by the leptonic currents of its decay products. For the rest of the production amplitude, the momenta of the gauge bosons are set on shell. The Breit–Wigner propagators arising in the absolute square of the amplitudes are separated. They are replaced by delta functions with an appropriate normalization obtained by integrating over the Breit–Wigner propagator in the limit $\Gamma_V \to 0$.

Since the iNWA turns out to reproduce the full calculation to sufficient accuracy in the LO comparison of Section 5.3.1, this strategy for describing the leptonic decays is applied for the NLO QCD calculations.

5 Numerical results

5.1 Setup and input parameters

For the numerical evaluations, the following SM parameters [51] are used,

$$\begin{aligned} M_W &= 80.425\,\text{GeV}\,, \quad M_Z = 91.1876\,\text{GeV}\,, \quad G_\mu = 1.16637\times10^{-5}\,\text{GeV}^{-2}\,, \\ M_H &= 150\,\text{GeV}\,, \quad \Gamma_H = 0.017\,\text{GeV}\,, \quad m_t = 174.3\,\text{GeV}\,. \end{aligned} \tag{5.1}$$

The total Higgs-boson width Γ_H has been calculated with *Hdecay* [52]. The only contribution from a Higgs boson at NLO QCD is given by the loop diagams in Figure 5. Since these diagrams turn out to contribute less than 0.3% to the cross sections for the chosen Higgs mass, their impact is not investigated further.[3] The electromagnetic coupling α is evaluated from (5.1) via

$$\alpha = \alpha_{G_\mu} = \frac{\sqrt{2}G_\mu M_W^2\left(1-\frac{M_W^2}{M_Z^2}\right)}{\pi}\,. \tag{5.2}$$

This choice of α absorbs some universal corrections to the electroweak coupling (running of α to the electroweak scale, leading corrections to the ρ-parameter), as is explained, e.g., in Ref. [53]. The widths of the weak gauge bosons are calculated according to Eqs. (4.3) and (4.4)—in case of the production of stable weak gauge bosons they are, of course, set to zero—from all decay channels at NLO QCD with the fermion masses neglected. With the value of the strong coupling at the scale M_Z taken from Ref. [54],

$$\alpha_s(M_Z) = 0.1176\,, \tag{5.3}$$

the calculated widths are

$$\Gamma_W = 2.0996\,\text{GeV}\,, \quad \Gamma_Z = 2.5097\,\text{GeV}\,. \tag{5.4}$$

[3] For $M_H > 2M_W$ the included Higgs-boson effects account for the interference between a H($\to$ WW) + jet signal and the coherent irreducible WW + jet background. A proper description of the signal requires, of course, also the squared resonance diagrams and contributions from gg fusion with the corresponding radiative corrections.

The SM parameters already used in the publications on WW+jet production [3, 9, 55, 56] are not replaced by the more recent values [54] in order to facilitate comparisons; the numerical impact of the slightly changed measured value of M_W is negligible anyway at the required accuracy.

The values for the strong coupling in the amplitude calculation are evaluated according to a 1-loop-running at LO and a 2-loop-running at NLO as described in Ref. [57],

$$\alpha_{s,1-loop}(\mu_{ren}) = \frac{1}{\frac{33-2N_f}{12\pi} \ln \frac{\mu_{ren}^2}{\Lambda_{QCD}^2}}, \tag{5.5}$$

$$\alpha_{s,2-loop}(\mu_{ren}) = \alpha_{s,1-loop}(\mu_{ren}) \left(1 - \frac{6(153-19N_f)}{(33-2N_f)^2} \frac{\ln\left(\ln \frac{\mu_{ren}^2}{\Lambda_{QCD}^2}\right)}{\ln \frac{\mu_{ren}^2}{\Lambda_{QCD}^2}} \right), \tag{5.6}$$

where μ_{ren} is the renormalization scale, N_f the number of active light-quark flavours, and Λ_{QCD} the QCD scale parameter. The values of Λ_{QCD} are chosen as prescribed by the applied PDF sets: In the five-flavour scheme, the PDFs of CTEQ6 [58,59] are used with $N_f = 5$, namely CTEQ6L1 with $\Lambda_{QCD} = 165\,\text{MeV}$ at LO and CTEQ6M with $\Lambda_{QCD} = 226\,\text{MeV}$ at NLO. In the four-flavour scheme, the PDFs of MRST2004 [60] with $N_f = 4$ are taken, namely MRST2004F4LO with $\Lambda_{QCD} = 220\,\text{MeV}$ at LO and MRST2004F4NLO with $\Lambda_{QCD} = 347\,\text{MeV}$ at NLO. The renormalization of α_s is performed as described in Section 3.1, i.e. with the heavy-quark loops in the gluon self-energy decoupled: In the five-flavour scheme only the top-quark loop is decoupled, in the four-flavour scheme both the top- and the bottom-quark loops are decoupled.

The Cabbibo angle in the approximation (2.1) for the CKM matrix is set to

$$\theta_C = 0.227\,, \tag{5.7}$$

the explicit entries are calculated from this.

To give an IR-safe definition of the cross section we apply the successive-combination jet algorithm of Ref. [61] with $R = 1$ to decide whether two final-state partons can be resolved as two separated jets or whether they have to be combined to only one jet. A dependence on the specific jet algorithm only arises through the real-emission subprocesses, because the LO and all other NLO contributions contain only one parton in the final state which is identified with the jet. To resolve the additional hadronic jet, a cut on the transverse momentum is applied. This renders the cross section also IR safe which would otherwise diverge already at LO. Different values are used for $p_{T,jet,cut}$ which are explicitly given for the respective results.

If the weak-gauge-boson decays are included, a set of additional cuts is applied which is in general not necessary for the finiteness of cross sections, but provides results that are closer to the experimental situation. These additional cuts are

$$|\eta_{jet}| < 4.5\,, \quad p_{T,lepton} > 25\,\text{GeV}\,, \quad |\eta_{lepton}| < 2.5\,, \tag{5.8}$$

where η is the pseudo-rapidity and p_T the transverse momentum of the respective particle. All leptonic cuts are applied only to charged leptons, of course. As an additional condition the missing transverse momentum, which is deduced from the sum of the neutrino momenta, is required to obey

$$p_{T,miss} > 25\,\text{GeV}\,. \tag{5.9}$$

The missing transverse momentum is particularly of interest if WW+jet is considered as a background process for SUSY searches. Here, the missing transverse momentum mimics the lightest supersymmetric particle that also leaves the detector undetected.

Furthermore, isolation cuts are applied in order to separate all visible leptons from each other and from hadronic jets,

$$R_{\text{lepton,jet}} > 0.4\,, \quad R_{\text{lepton,lepton}} > 0.2\,, \tag{5.10}$$

where $R_{ab} = \sqrt{(\Delta\varphi_{ab})^2 + (\Delta\eta_{ab})^2}$. The angular distance between the two particles a, b in the transverse plane is denoted by $\Delta\varphi_{ab}$, and $\Delta\eta_{ab}$ is the difference of their pseudo-rapidities.

5.2 Results on integrated cross sections

We start our discussion of numerical results with integrated cross sections. In order to render these cross sections insensitive to the decay of the W bosons, we do not apply the cuts on the decay leptons specified in Eqs. (5.8)–(5.10) in this section.

5.2.1 LO cross sections

The LO cross sections get contributions from $\mathrm{q}\bar{\mathrm{q}}$, qg, and $\mathrm{g}\bar{\mathrm{q}}$initial states. In this section, the relevance of the respective partonic channels is discussed both for results on proton–proton collisions at $\sqrt{s} = 14\,\text{TeV}$ (LHC setup) and on proton–antiproton collisions at $\sqrt{s} = 1.96\,\text{TeV}$ (Tevatron setup). Scale variations of a factor 10 around the central scale, which is chosen to be M_{W}, are considered. Here and in the following sections, the common scale $\mu = \mu_{\text{ren}} = \mu_{\text{fact}}$ is used, i.e. renormalization and factorization scales are set equal and are varied simultaneously.

Figure 10 shows the results for the various partonic contributions to WW+jet production, evaluated in the five-flavour scheme. At the LHC, each partonic process involves at most one valence quark. Therefore, the gluon flux, which is essentially larger at the LHC compared to Tevatron, in general leads to larger contributions from qg channels compared to $\mathrm{q}\bar{\mathrm{q}}$ annihilation, whereas the $\mathrm{g}\bar{\mathrm{q}}$ initial states contribute significantly less since no valence partons are involved here. The situation at Tevatron is different, because the proton–antiproton collisions provide $\mathrm{q}\bar{\mathrm{q}}$ contributions with two valence partons that dominate the cross sections. The scale dependence of the cross sections at Tevatron turns out to be stronger than at LHC, which is due to the factorization-scale variation. While the renormalization-scale variation only reflects the running of the strong coupling α_{s}, which is the same in both cases, the factorization scale dependence is quite flat for nearly all channels at LHC in the considered range. At Tevatron, however, an increase of roughly the same order as the one arising from the renormalization-scale dependence is found in the direction of lower scales. A detailed analysis of the scale dependence of LO cross sections to WW+jet production is provided in Ref. [49].

In case of the LHC, the partonic contributions with up-type quarks dominate over those with down-type quarks, which can be understood by comparing the valence-quark PDFs in the protons. The antiquark PDFs of the lightest generation result in an inverted order of the $\mathrm{g}\bar{\mathrm{q}}$ channels at the LHC where the $\mathrm{g}\bar{\mathrm{d}}$ channel prevails the $\mathrm{g}\bar{\mathrm{u}}$ contribution. For Tevatron, the described valence-PDF effect occurs twice in the $\mathrm{q}\bar{\mathrm{q}}$ channel, leading roughly to a factor 4 between $\mathrm{u}\bar{\mathrm{u}}$ and $\mathrm{d}\bar{\mathrm{d}}$. The channels qg and $\mathrm{g}\bar{\mathrm{q}}$ deliver exactly the same contribution to the integrated cross sections due to the charge-conjugation-invariant hadronic initial state. Naturally, the channels

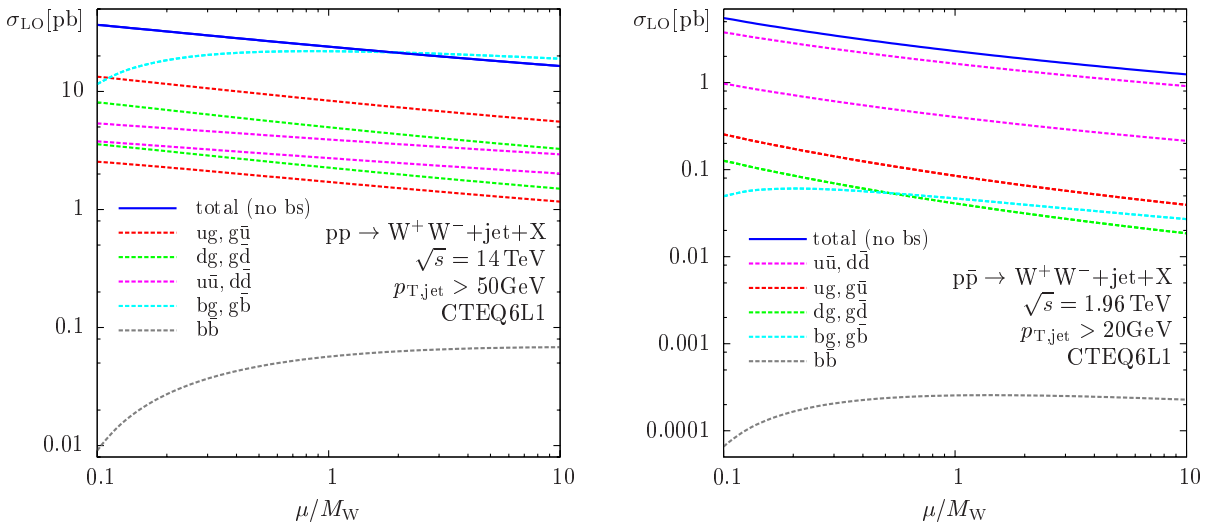

Figure 10: Partonic contributions to the LO cross sections of WW+jet at the LHC (l.h.s.) and the Tevatron (r.h.s.): The variation of the common scale $\mu = \mu_{\mathrm{fact}} = \mu_{\mathrm{ren}}$ is shown for all channels. If more than one curve with identical colours is given, the first one mentioned in the key corresponds to the upper curve. The contribution named "total" does not contain contributions from external bottom quarks.

involving valence-(anti-)quarks dominate, and therefore the described PDF effect leads again to larger contributions from $\mathrm{ug/g\bar{u}}$ compared to $\mathrm{d\bar{g}/g\bar{d}}$.

In addition, for both colliders the channels involving bottom flavours are shown in Figure 10. As expected, $\mathrm{b\bar{b}}$ annihilation is numerically negligible in both cases, whereas the bg channel and the $\mathrm{g\bar{b}}$ channel—whose contributions to the integrated cross section are the same—each account roughly for the same amount as all the subprocesses involving (anti-)quarks of the two light generations at the LHC. As already explained in Section 2.2, this is due to the fact that these subprocesses actually describe resonant and non-resonant $\mathrm{W^-t}$ and $\mathrm{W^+\bar{t}}$ production, respectively, with the top decays included. In addition the bottom PDF is due to the gluon splitting $\mathrm{g \to b\bar{b}}$. The bg-flux is thus rather large at the LHC due to the large gluon lumionsity. As mentioned earlier the corresponding contributions should be attributed to different processes, therefore these channels and the respective NLO corrections are not taken into account. For Tevatron, their numerical impact is not that large, since the centre-of-mass (CM) energy to produce top resonances in addition to a W boson is rarely available and the gluon flux is small. The respective channels are, however, treated in the same way as for the LHC. The different shapes of the scale-variation curves with bottom flavours result from a strong decrease of the bottom PDFs for smaller values of the factorization scale.

5.2.2 NLO QCD cross sections

After analyzing the individual contributions to the LO cross sections in the previous section, the effects of NLO QCD corrections on the WW+jet cross sections are discussed here. For the numerical results of this and the following sections, two different definitions of the NLO observables are used. The one observable is defined more inclusively by only requiring at least

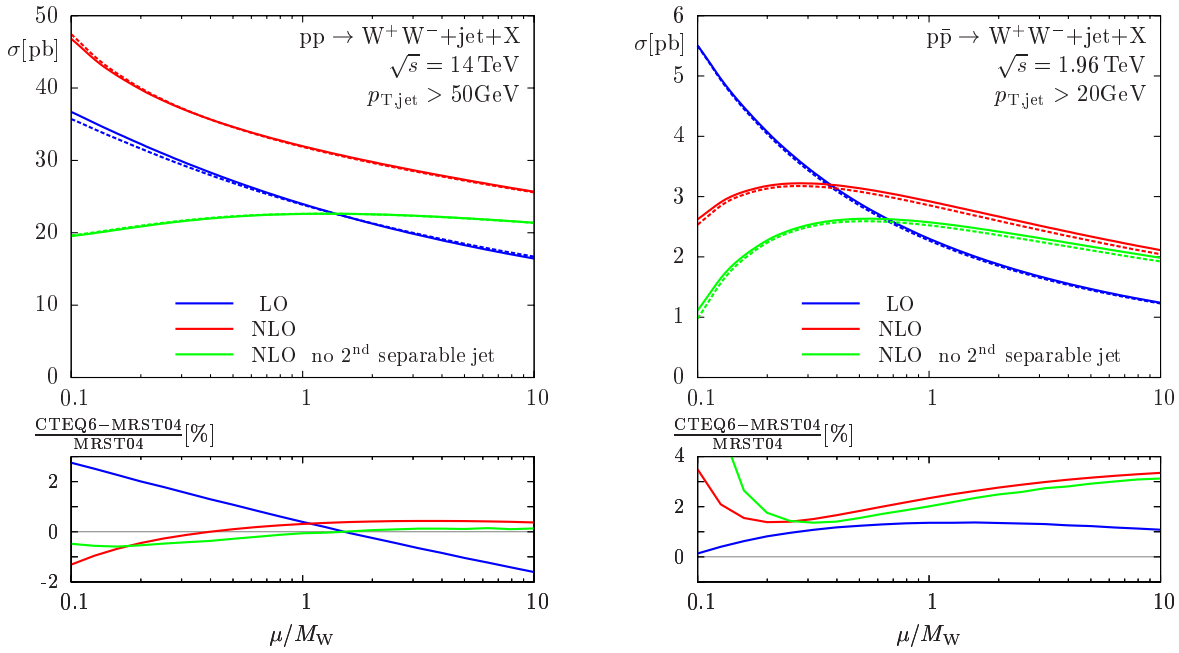

Figure 11: Comparison of WW+jet production cross sections in the LHC setup with $p_{\mathrm{T,jet}} > 50\,\mathrm{GeV}$ and for Tevatron with $p_{\mathrm{T,jet}} > 20\,\mathrm{GeV}$: The straight lines show the results calculated with the five-flavour PDFs of CTEQ6, the dashed lines those calculated with the four-flavour PDFs of MRST2004F4. Contributions from external bottom (anti-)quarks are omitted, as described in Section 2.2.

one hard jet with a minimum transverse momentum after application of the jet algorithm. The more exclusively defined observable applies a veto on a second separable hard jet and describes therefore genuine WW+jet production. To this end, real-correction events with two jets that fulfill the $p_{\mathrm{T,jet,cut}}$ condition and are not combined by the jet algorithm are not counted in the more exclusive observable. The phase-space regions in the real-correction subprocesses that are relevant for curing infrared singularities from the virtual corrections are not influenced, since the applied restriction only refers to genuine WW+2jets events. Therefore, the difference between the results for the two NLO observables is precisely given by the respective LO observable of WW+2jets production—evaluated, however, in the NLO setup (NLO PDFs, 2-loop running of α_{s}).

(i) Four-flavour versus five-flavour scheme and scale dependence of NLO QCD cross sections

We start the discussion of the scale dependence of the NLO cross sections with a comparison between the results obtained in the four-flavour and the five-flavour schemes, respectively, as described in Section 2.2. The NLO QCD cross sections for WW+jet production are presented in Figure 11 for the LHC setup with $p_{\mathrm{T,jet,cut}} = 50\,\mathrm{GeV}$ and for the Tevatron setup with $p_{\mathrm{T,jet,cut}} = 20\,\mathrm{GeV}$, both for the four-flavour calculations with MRST2004F4 PDFs and the five-flavour calculations with CTEQ6 PDFs. In the four-flavour calculation, loop diagrams involving (massive) 3rd-generation quarks are included. However, their contributions account for less than 0.2% to the integrated cross sections.

In case of the LHC, the relative deviations between the NLO cross sections in the two schemes behave as follows: while the deviation significantly increases in direction of lower scales at LO, which leads, however, to relative deviations of less than 3% in the whole range, it is nearly flat for both NLO observables where the results deviate by less than 2%. For the Tevatron, the comparison between the two approaches reveals deviations of less than 2% at LO over the full range of scale variations. The NLO cross sections turn out to be slightly larger in the CTEQ6 approach, but on a level of less than 4% for the whole range of interest. The smallest scales depicted may be ignored, because they obviously describe a region where the NLO calculation is not a good approximation anymore, as one can see from the steep decline of the absolute values for the NLO cross sections in that range of scales.

Since the results evaluated with different PDF sets can in general not be expected to agree exactly—not only in the present case where different descriptions of the bottom (anti-)quark are applied—this analysis can be seen as a confirmation that the approximation that is applied in the five-flavour calculation delivers fully acceptable results. Moreover, the deviations between the two approaches are far below the expected experimental errors. The good agreement has been further confirmed by performing the same comparison for $p_{\mathrm{T,jet,cut}} = 100\,\mathrm{GeV}$ at LHC and for $p_{\mathrm{T,jet,cut}} = 50\,\mathrm{GeV}$ at Tevatron, yielding the same level of agreement. In addition, also differential cross sections have been compared with no significant deviations showing up in any phase-space regions. Numerical results of these further comparisons are omitted here, because they are not supposed to provide new insight. In the following, only the five-flavour scheme with CTEQ6 PDFs is used.

Considering the scale dependence in the transition from LO to NLO at the LHC (see Figure 11), only a modest reduction is observed if W-boson pairs in association with two hard jets are taken into account. This large residual scale dependence is mainly due to the qg channels, followed by those contributions with two valence quarks in the initial state that are present in the real corrections, but not at LO. The scale dependence can be significantly suppressed upon applying the veto of having "no 2$^{\mathrm{nd}}$ separable jet". The relevance of a jet veto in order to suppress the scale dependence at NLO was also realized for genuine W-pair production at hadron colliders [62]. A reduction of the difference between the two curves, which represents—as mentioned in the beginning of this section—the contribution of genuine WW+2jets events, is also achieved by increasing the value of the cut on $p_{\mathrm{T,jet}}$, which is illustrated in Figure 12 for WW+jet production with $p_{\mathrm{T,jet,cut}} > 100\,\mathrm{GeV}$ in the LHC setup and $p_{\mathrm{T,jet,cut}} > 50\,\mathrm{GeV}$ for the Tevatron. Explicit numbers for the cross sections—both with and without leptonic W decays—are collected in Tables 1 – 4.

In general, the influence of the restriction on genuine WW+jet production via the described jet veto is not that large in the Tevatron setup (see Figure 11). This can be understood from the lower CM energy at the Tevatron: The energy for producing a second hard jet is available less frequently here, so that a stronger suppression of WW+2jets events is obtained. The fact that the difference between the two NLO observables strongly decreases when going to higher $p_{\mathrm{T,jet,cut}}$ values—as shown on the right-hand side of Figure 12—confirms this interpretation.

In Figure 13, the respective plots are shown with the W decays included via the iNWA and with further cuts applied according to Eqs. (5.8) – (5.10). Qualitatively, the features discussed above can be observed as well.

$pp \to W^+W^- + \text{jet} + X$ @ 14 TeV			
$\mu = \mu_{\text{ren}} = \mu_{\text{fact}}$	σ_{LO}[pb]	$\sigma_{\text{NLO,excl}}$[pb]	$\sigma_{\text{NLO,incl}}$[pb]
$0.5\,M_W$	27.17638(89)	22.216(15)	34.641(14)
$1\,M_W$	23.97398(79)	22.606(12)	31.970(11)
$2\,M_W$	21.26027(70)	22.5646(97)	29.7959(89)
$pp \to W^+(\to \nu_e e^+)W^-(\to \mu^- \bar{\nu}_\mu) + \text{jet} + X$ @ 14 TeV			
$\mu = \mu_{\text{ren}} = \mu_{\text{fact}}$	σ_{LO}[fb]	$\sigma_{\text{NLO,excl}}$[fb]	$\sigma_{\text{NLO,incl}}$[fb]
$0.5\,M_W$	118.849(11)	89.227(99)	148.826(68)
$1\,M_W$	104.9482(94)	93.789(76)	138.808(56)
$2\,M_W$	93.1789(83)	95.493(60)	130.401(57)

Table 1: WW+jet cross sections at the LHC, calculated in the five-flavour scheme with CTEQ6 PDFs. The cut on the transverse momentum of the jet is set to 50 GeV. In the lower part of the table where the decays of the W bosons are included further cuts according to Eqs. (5.8) – (5.10) are applied.

$pp \to W^+W^- + \text{jet} + X$ @ 14 TeV			
$\mu = \mu_{\text{ren}} = \mu_{\text{fact}}$	σ_{LO}[pb]	$\sigma_{\text{NLO,excl}}$[pb]	$\sigma_{\text{NLO,incl}}$[pb]
$0.5\,M_W$	12.01935(44)	11.8943(76)	16.2377(73)
$1\,M_W$	10.37216(39)	11.4827(57)	14.6889(57)
$2\,M_W$	9.02371(34)	11.0114(46)	13.4405(44)
$pp \to W^+(\to \nu_e e^+)W^-(\to \mu^- \bar{\nu}_\mu) + \text{jet} + X$ @ 14 TeV			
$\mu = \mu_{\text{ren}} = \mu_{\text{fact}}$	σ_{LO}[fb]	$\sigma_{\text{NLO,excl}}$[fb]	$\sigma_{\text{NLO,incl}}$[fb]
$0.5\,M_W$	61.6020(66)	57.471(40)	79.722(45)
$1\,M_W$	53.2170(57)	56.734(47)	73.199(39)
$2\,M_W$	46.3585(50)	55.192(38)	67.680(28)

Table 2: As in Table 1, but with $p_{\text{T,jet,cut}} = 100$ GeV.

$p\bar{p} \to W^+W^- + \text{jet} + X$ @ 1.96 TeV			
$\mu = \mu_{\text{ren}} = \mu_{\text{fact}}$	σ_{LO}[pb]	$\sigma_{\text{NLO,excl}}$[pb]	$\sigma_{\text{NLO,incl}}$[pb]
$0.5\,M_W$	2.88967(29)	2.6343(32)	3.1417(30)
$1\,M_W$	2.30259(24)	2.5761(24)	2.9257(21)
$2\,M_W$	1.87503(20)	2.4208(18)	2.6688(16)
$p\bar{p} \to W^+(\to \nu_e e^+)W^-(\to \mu^-\bar{\nu}_\mu) + \text{jet} + X$ @ 1.96 TeV			
$\mu = \mu_{\text{ren}} = \mu_{\text{fact}}$	σ_{LO}[fb]	$\sigma_{\text{NLO,excl}}$[fb]	$\sigma_{\text{NLO,incl}}$[fb]
$0.5\,M_W$	13.7407(21)	12.2366(88)	14.8002(91)
$1\,M_W$	10.9245(17)	12.0582(72)	13.8052(73)
$2\,M_W$	8.8789(14)	11.3695(68)	12.6152(68)

Table 3: As in Table 1, but at the Tevatron with $p_{\text{T,jet,cut}} = 20\,\text{GeV}$.

$p\bar{p} \to W^+W^- + \text{jet} + X$ @ 1.96 TeV			
$\mu = \mu_{\text{ren}} = \mu_{\text{fact}}$	σ_{LO}[fb]	$\sigma_{\text{NLO,excl}}$[fb]	$\sigma_{\text{NLO,incl}}$[fb]
$0.5\,M_W$	0.843556(80)	0.76867(81)	0.83508(80)
$1\,M_W$	0.657787(64)	0.74241(58)	0.78664(55)
$2\,M_W$	0.525619(52)	0.68820(44)	0.71884(44)
$p\bar{p} \to W^+(\to \nu_e e^+)W^-(\to \mu^-\bar{\nu}_\mu) + \text{jet} + X$ @ 1.96 TeV			
$\mu = \mu_{\text{ren}} = \mu_{\text{fact}}$	σ_{LO}[fb]	$\sigma_{\text{NLO,excl}}$[fb]	$\sigma_{\text{NLO,incl}}$[fb]
$0.5\,M_W$	4.55105(67)	4.0799(36)	4.4484(36)
$1\,M_W$	3.54156(53)	3.9594(27)	4.2037(27)
$2\,M_W$	2.82493(43)	3.6774(21)	3.8466(21)

Table 4: As in Table 1, but at the Tevatron with $p_{\text{T,jet,cut}} = 50\,\text{GeV}$.

(ii) Dependence on the transverse-momentum cut on the jet

To close the discussion of the NLO cross sections for WW+jet that are not sensitive to the decays of the W bosons, the dependence on the cut applied to the transverse momentum of the jet is considered here. In Figure 14, the $p_{\text{T,jet,cut}}$ dependence is shown for the LHC and the Tevatron setup, respectively. In order to introduce a measure for the scale uncertainties of the cross sections, bands are depicted that correspond to a variation of $\mu = \mu_{\text{ren}} = \mu_{\text{fact}}$ by a factor 2 around the central scale. A crossing of the curves for differing scale values leads to vanishing band widths at some points, which is an artifact of how the results are depicted and should not be misinterpreted as a vanishing scale uncertainty. In the plots of Figure 14, the band corresponding to the more inclusive cross section is partially covered by the more exclusive one. Both curves are, however, shown here in order to confirm the statement that the effect of genuine WW+2jets events decreases with an increasing value of $p_{\text{T,jet,cut}}$. This becomes manifest in the overlap of the two bands especially for large cut values at the Tevatron, but is also evident in

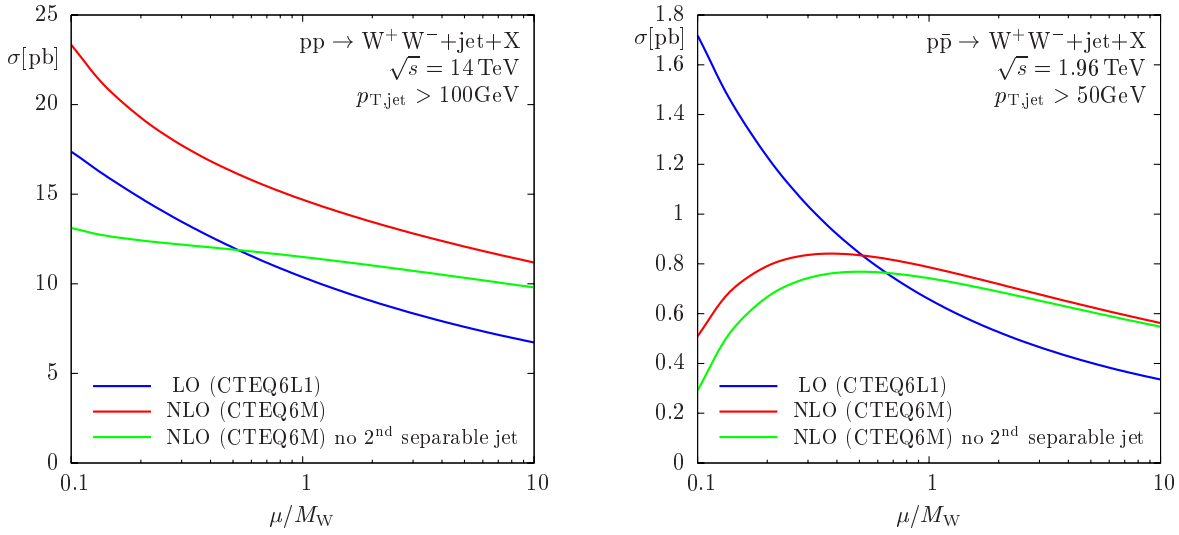

Figure 12: Scale dependence of the WW+jet cross sections with $\mu = \mu_{\text{fact}} = \mu_{\text{ren}}$, where $p_{\text{T,jet}} > 100\,\text{GeV}$ is applied for the LHC, and $p_{\text{T,jet}} > 50\,\text{GeV}$ for the Tevatron.

the plots for the LHC setup from the convergence of the two NLO bands when going to larger values for $p_{\text{T,jet,cut}}$. Eventually, the $p_{\text{T,jet,cut}}$ variation reflects the behaviour discussed in the previous paragraph: For Tevatron, a considerable reduction of the scale uncertainty is achieved when going from LO to NLO, whereas this reduction is only mild for LHC unless WW+2jets events are vetoed.

5.3 Results on differential cross sections

Now we mainly focus on differential distributions in observables defined from the W decay products, i.e. the cuts on the decay leptons specified in Eqs. (5.8)–(5.10) are applied.

5.3.1 LO analysis of the different decay descriptions

The integrated WW+jet cross section as defined above is not sensitive to the decays of the W bosons. An inclusion of leptonic decays into the calculation of WW+jet production can be performed in different ways. In this section, a comparison of LO results for the three strategies discussed in Section 4 is performed, which are a full amplitude calculation within the complex-mass scheme, the naive NWA, and its improved version iNWA that treats the W bosons as on-shell particles, but keeps spin correlations. The aim of this discussion is to find an adequate approximation in order to avoid performing the full amplitude calculation but still to obtain an appropriate description of the decays.

Considering only integrated cross sections, both approximations reproduce the full results in the LHC setup at the expected accuracy of $O(\Gamma_{\text{V}}/M_{\text{V}})$. More precisely, we find a deviation of about 3% for the naive NWA and of less than 1% for the improved version with $p_{\text{T,jet,cut}} = 50, 100\,\text{GeV}$. In the Tevatron setup, the naive NWA predicts cross sections deviating by roughly 15% (9%) for $p_{\text{T,jet,cut}} = 20\,\text{GeV}$ (50 GeV), while the iNWA is good within 1%. The differences between the two approximations are due to the ignored spin correlations in the naive NWA, which lead to different distributions of the decay leptons over the phase space. These changes

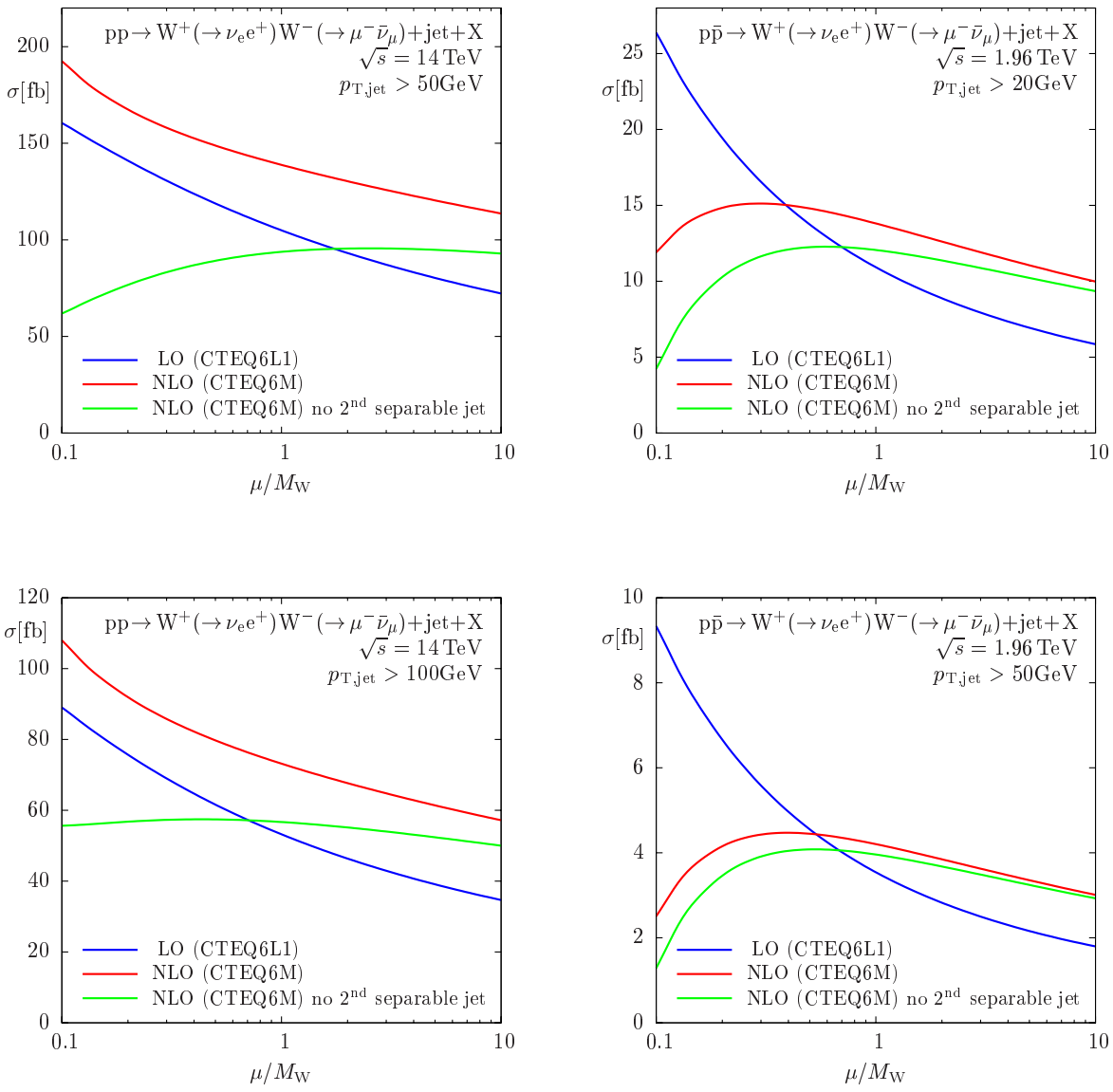

Figure 13: Scale dependence of the WW+jet cross sections with W decays included and further cuts applied according to Eqs. (5.8) – (5.10). The five-flavour scheme with CTEQ6 PDFs is used. In the LHC setup, the results are given for $p_{T,\text{jet,cut}} = 50\,\text{GeV}$ (upper left plot) and for $p_{T,\text{jet,cut}} = 100\,\text{GeV}$ (lower left plot). For the Tevatron we show results for $p_{T,\text{jet,cut}} = 20\,\text{GeV}$ (upper right plot) and for $p_{T,\text{jet,cut}} = 50\,\text{GeV}$ (lower right plot).

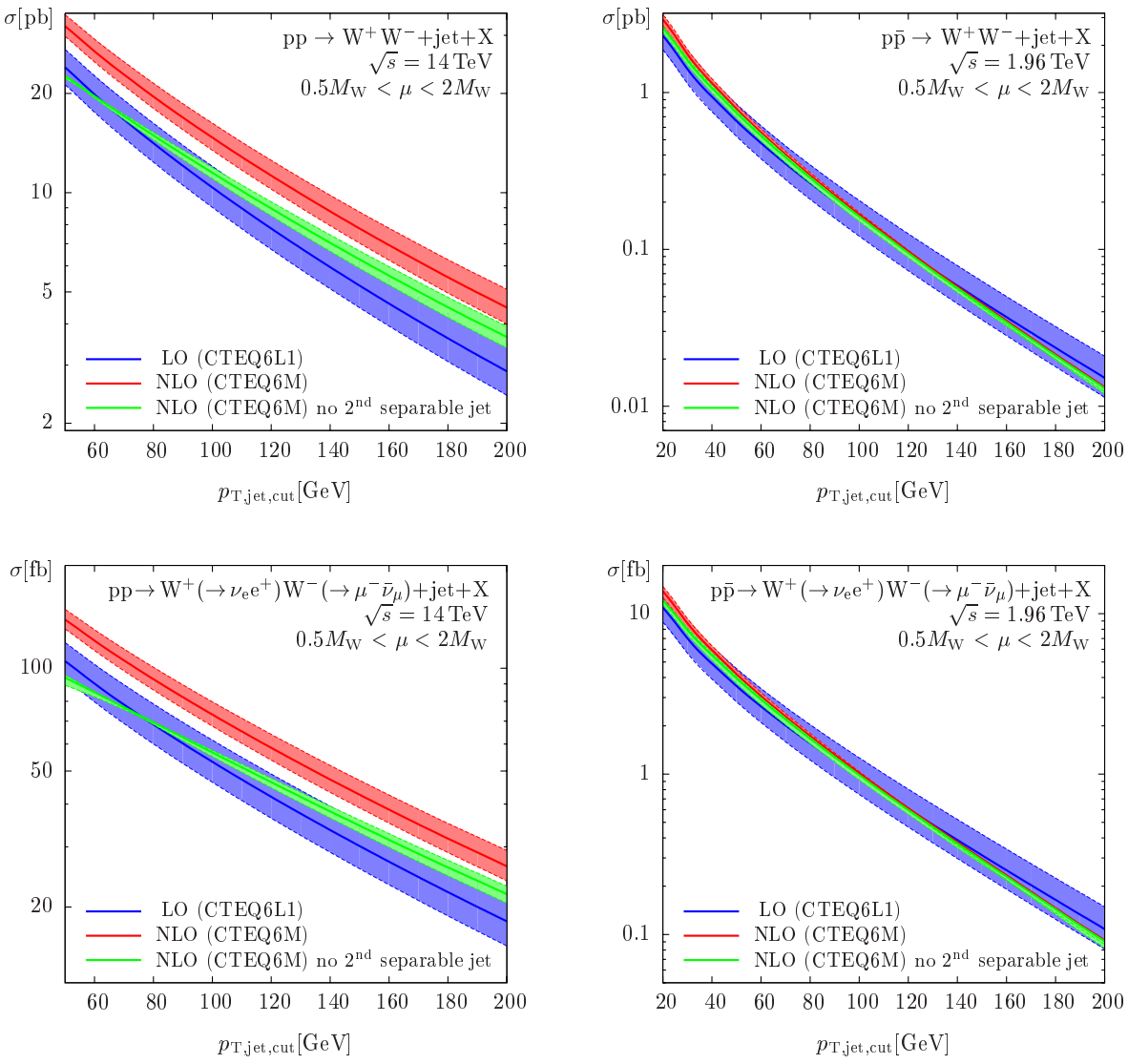

Figure 14: Variation of the WW+jet cross sections with $p_{\mathrm{T,jet,cut}}$ at the LHC (l.h.s.) and at the Tevatron (r.h.s.): The bands correspond to a scale variation, again with $\mu = \mu_{\mathrm{fact}} = \mu_{\mathrm{ren}}$, by a factor 2 around the central scale. The red and the green curves correspond to the different definitions of the NLO observable, where the red one depicts the more inclusive quantity. The upper plots correspond to stable W's, the lower plots include leptonic W decays with the additional cuts of Eqs. (5.8) – (5.10) applied.

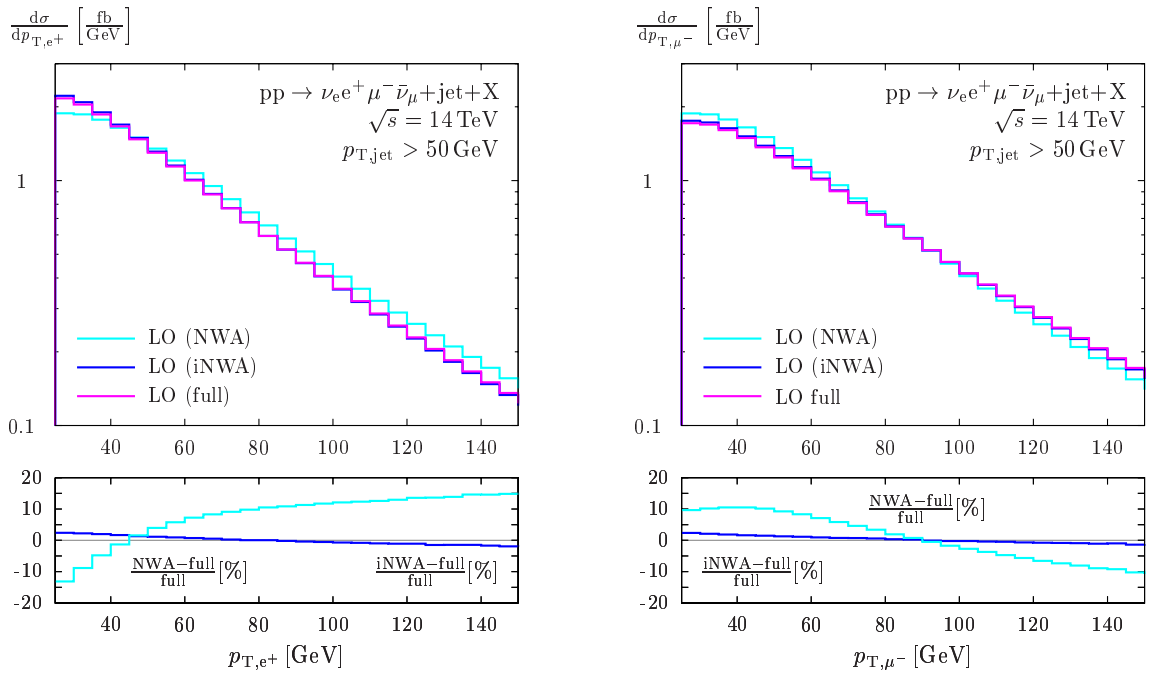

Figure 15: Comparison of different W-decay descriptions in the p_T distributions of each of the two decay leptons. The LO cross sections are evaluated at $\mu = \mu_{\text{fact}} = \mu_{\text{ren}} = M_W$ for the full amplitude calculation, the naive NWA, and the improved NWA.

become manifest in the integrated cross sections if cuts on the decay products are applied. In general, both the naive and the improved version of the NWA give the same integrated cross sections if no leptonic cuts are applied. This is due to the fact that taking the spin correlations into account only causes a (W-polarization-dependent) redistribution of the momenta of the decay leptons, which does not influence the result as long as the full decay phase spaces are integrated over.

Distributions in specific variables are, however, strongly affected, which can be seen from the differential cross sections for the LHC given in Figures 15, 16, and 17. Only the distributions for decay leptons are shown there, because these are, naturally, mainly affected by the different decay descriptions. Considering the distributions of transverse momentum p_T and pseudo-rapidity η of each of the two decay leptons, the improved NWA delivers a very accurate reproduction of the full calculation, whereas the naive version deviates by up to 15% in some phase-space regions. The distributions of the angles between the two leptons—φ denotes the angle in the transverse plane and $\cos\theta$ the cosine of the angle between the two leptons—resulting from the full amplitude calculation are also in general reproduced more precisely by the improved NWA. At the Tevatron the situation is quite similar, which can be read off Figures 18 and 19: While the improved NWA reproduces the full result quite well, the predictions of the naive NWA deviate quite strongly—in particular in case of the pseudo-rapidity distributions of the leptons.

The analysis of this section justifies the application of the improved NWA for the NLO QCD calculations to $pp/p\bar{p} \to WW + \text{jet} + X$ with leptonic decays.

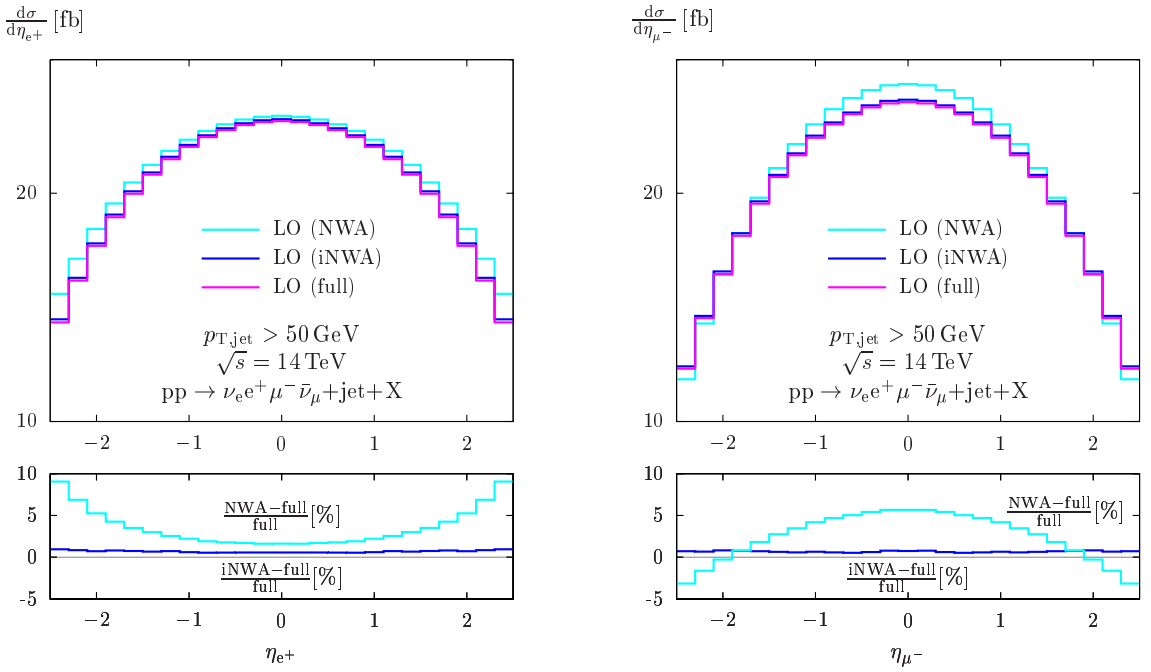

Figure 16: As in Figure 15, but for the η distributions of the two decay leptons.

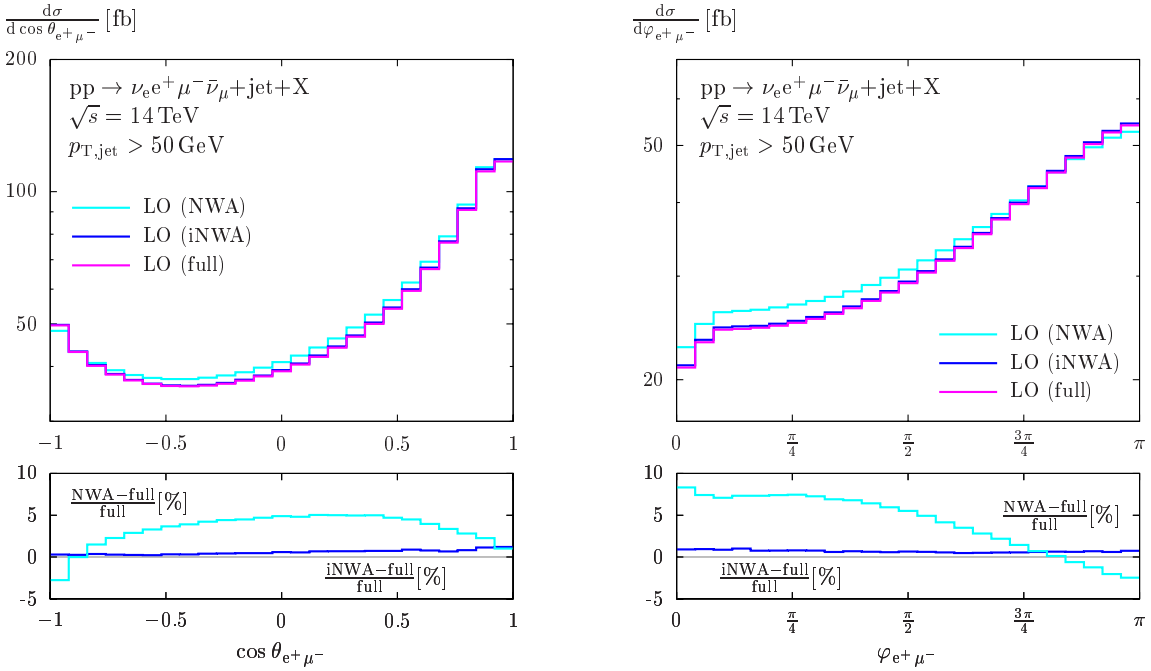

Figure 17: As in Figure 15, but for the cosine of the opening angle, $\cos\theta$, and the angle φ in the transverse plane between the two leptons.

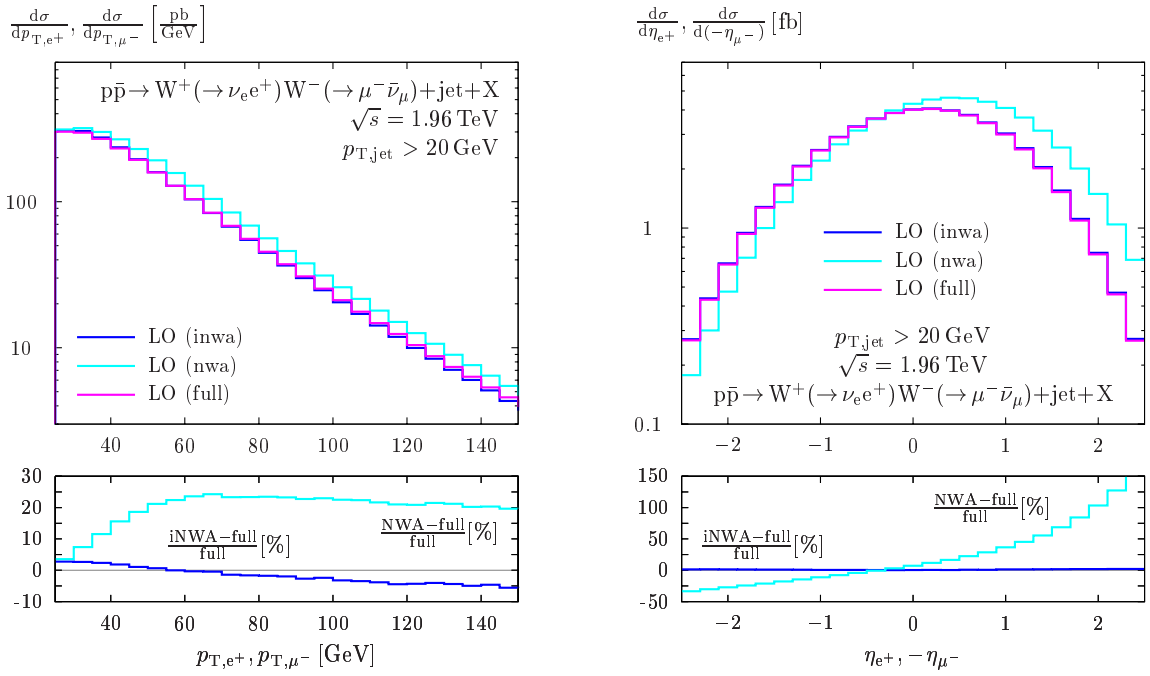

Figure 18: Comparison of different W-decay descriptions in the p_T and η distributions of each of the two decay leptons. The LO cross sections are evaluated at $\mu = \mu_{fact} = \mu_{ren} = M_W$ for the full amplitude calculation, the naive NWA, and the improved NWA at the Tevatron.

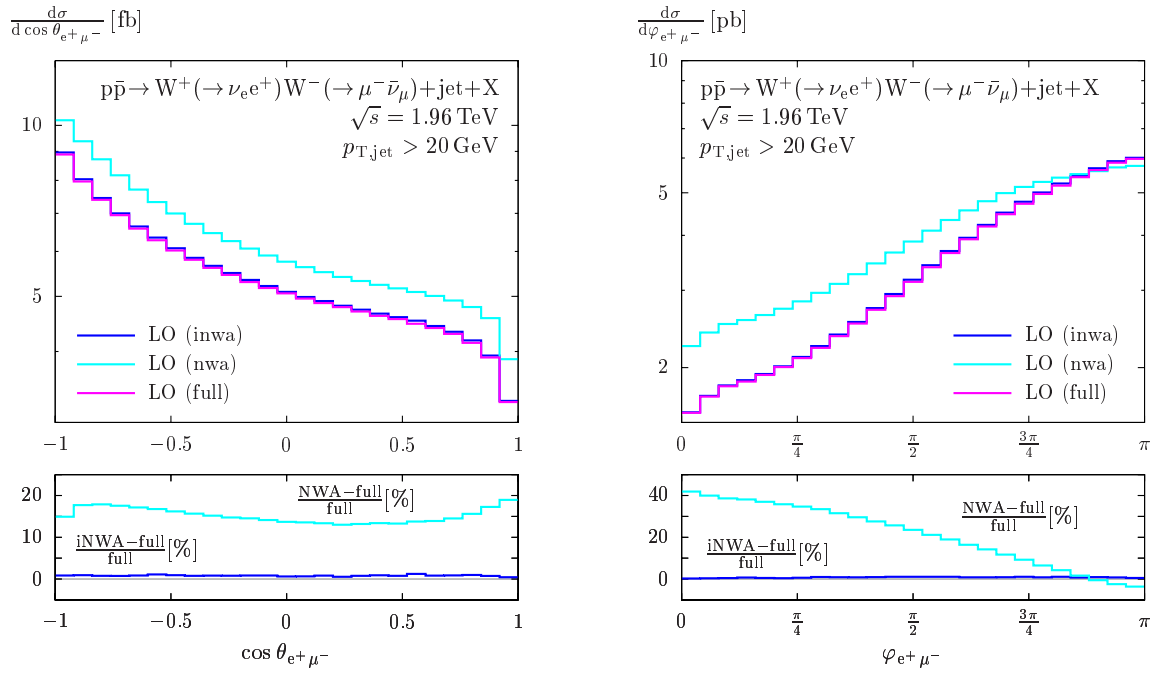

Figure 19: As in Figure 18, but for the cosine of the opening angle, $\cos\theta$, and the angle φ in the transverse plane between the two leptons.

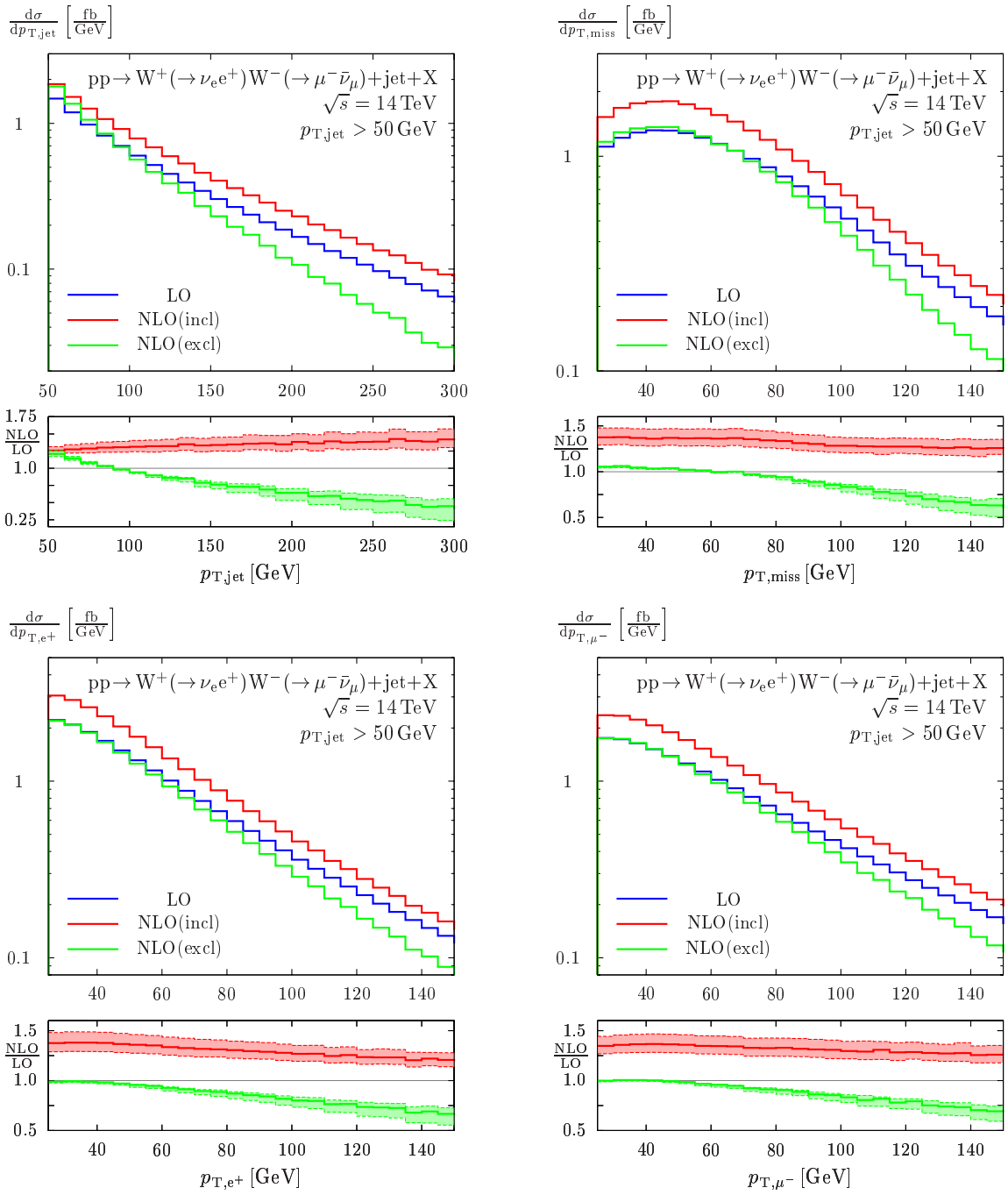

Figure 20: Differential cross sections for WW+jet with decays included in the improved NWA at the LHC: The LO and NLO distributions are shown for $\mu = \mu_{\text{fact}} = \mu_{\text{ren}} = M_W$. The distributions for the transverse momenta p_T of the jet and of the decay leptons, and for the missing transverse momentum $p_{T,\text{miss}}$ are depicted. The bands in the K-factors are precisely defined in the text.

5.3.2 *Differential NLO cross sections at the LHC*

A survey of distributions for differential WW+jet cross sections with leptonic W decays is given in Figures 20 – 22 for the LHC setup with $p_{\mathrm{T,jet,cut}} = 50\,\mathrm{GeV}$ and $\mu = \mu_{\mathrm{ren}} = \mu_{\mathrm{fact}} = M_{\mathrm{W}}$. The relative size of the NLO corrections is represented in terms of a K-factor. The depicted bands correspond to a variation of the scale μ by a factor of 2 in the NLO quantities only, i.e. we show $\sigma_{\mathrm{NLO}}(\mu)/\sigma_{\mathrm{LO}}(M_{\mathrm{W}})$ with $0.5M_{\mathrm{W}} < \mu < 2M_{\mathrm{W}}$.

The jet distributions are understood as distributions of the hardest jet. Figure 20 provides transverse-momentum distributions of the hadronic jet, of the missing transverse momentum due to (anti-)neutrinos leaving the detector undetected (upper plots), and of the two charged decay leptons (lower plots). For all p_{T} distributions, a tendency of the more exclusive NLO cross section to decrease faster than the LO cross section when going to higher values is evident. To a large extent this is due to the fact that a fixed value is used for the renormalization scale. Instead, the transverse momentum of the jet seems a more appropriate scale in the high-p_{T} tail, since the only arising strong coupling concerns this jet. Using $\alpha_{\mathrm{s}}(M_{\mathrm{W}})$ in the LO calculation overestimates the contributions for large $p_{\mathrm{T,jet}}$ values due to the ignored decrease of the QCD coupling. In other words, the large $p_{\mathrm{T,jet}}$ introduces an additional scale which is responsible for a large logarithmic enhancement. These corrections may be absorbed into the running of the strong coupling constant (and thus resummed to all orders) by using a more appropriate renormalization scale, i.e. a scale that is set through $p_{\mathrm{T,jet}}$. Similar arguments can explain part of the behaviour at small p_{T} observed in the respective plots of Figure 20, but of course the theoretical description in regions of small transverse momenta should eventually be improved by dedicated resummations of higher-order QCD corrections.

Since the leptonic transverse momenta are connected to $p_{\mathrm{T,jet}}$ by momentum conservation, the same argumentation also holds for these distributions. The effects are, however, much stronger for the jet compared to the leptons due to the tendency of coloured particles to collinearly radiate further QCD partons. For the more inclusive NLO observable, this effect is overcompensated by genuine WW+2jets events which are—being actually LO contributions—also influenced by this effect. In the p_{T} distributions for the two decay leptons, a slight tendency to higher p_{T} can be found for the lepton. That a difference between lepton and antilepton arises at all can be understood from the defined order of the W bosons coupling to the fermion chain, because t-channel-like emissions of the W bosons cause large contributions. Whereas a t-channel-like emission of a W^+ can only arise in case of an incoming up quark or down antiquark, an analogous emission of a W^- always stems from an incoming down quark or up antiquark. The antilepton always results from the W^+ decay and the lepton from the W^- decay. Due to the difference of the involved PDFs, the antilepton prefers lower transverse momenta compared to the lepton.

An important impact of this effect can also be seen in the upper plots of Figure 21 where distributions of the pseudo-rapidities of the leptons are depicted. Here, the antilepton shows a slightly larger tendency to small angles against the beam axes than the lepton. Naturally, due to the symmetric hadronic initial state in proton–proton collisions the pseudo-rapidity distributions are symmetric. The size of the relative NLO corrections turns out to be nearly independent of these quantities—well described by a constant K-factor. The symmetry property still holds for the pseudo-rapidity of the hadronic jet, which is shown in the lower plot of Figure 21. The NLO corrections to this quantity, however, increase for larger pseudo-rapidities. These large positive corrections in the region of large pseudo-rapidities can be understood by a simple statistical

effect: NLO corrections in general redistribute events via radiation. Since most events show jets in the region of lower pseudo-rapidities, it is just more likely to redistribute events from the low-pseudo-rapidity region to the high-pseudo-rapidity region than vice versa. Apart from this small phase-space region, which is negligible anyway if the total amount of events is considered, the NLO corrections turn out to be nearly independent of the jet pseudo-rapidity as well.

The invariant-mass distribution of the charged leptons, which is shown in the lower right plot of Figure 21, depicts the typical behaviour of two particles that are not resonantly produced: while the steep increase at low invarint masses is mainly due to the lepton-separation cut and the transverse-momentum cuts on the individual particles, the decrease to higher values reflects the behaviour of all variables involving a new energy scale, according to the dependence of hadronic cross sections on the partonic centre-of-mass energy.

The two distributions in Figure 22 depict the angular correlations between the two decay leptons. The angle between the two leptons in the transverse plane is represented by φ, which is a quantity invariant under boosts along the beam direction. By θ the opening angle between these two leptons in the laboratory frame is denoted. Considering the φ distribution, i.e. ignoring the boost effect along the beam axes, the two charged leptons turn out to fly preferentially into opposite directions. This is not surprising, since momentum conservation forces the two W bosons at least to show a tendency to opposite directions which is mediated to their decay products by boost effects. The angle between the leptons is, however, important for the distinction of the background process WW+jet from the signal process H($\to$ WW*)+jet in Higgs searches. This is due to the fact that the decay leptons of a W-boson pair arising from the decay of a scalar Higgs particle show the—on the first view non-intuitive—tendency to fly into the same direction. This property results from the spin correlation of the W^+W^- system, which is discussed in detail in Ref. [63]: Since, in the rest frame of the Higgs boson, the helicities of the W bosons are correlated, and only a left-handed charged lepton and a right-handed charged antilepton can arise from the W decays, their emission in the same direction is favoured. This correlation effect is, of course, smeared in H($\to$ WW*)+jet, since the Higgs boson is in general boosted, but a remainder of the effect should still be measurable.

For WW+jet production, however, the helicities of the two W bosons are not correlated in this way, as depicted in Figure 22, but tend to opposite directions. In the $\cos\theta$ distribution, this preference is overcompensated by the boost effect along the beam axes, leading to a tendency in direction of small opening angles. The dependence of the size of NLO corrections on both angles turns out to be of the order of 10–20%.

5.3.3 Differential NLO cross sections at the Tevatron

Considering the same quantities for WW+jet production in the Tevatron setup, most of the effects can be explained by the fact that proton–antiproton collisions take place here instead of proton–proton collisions. Besides, the lower CM energy compared to the LHC plays an important role. We start again with the discussion of transverse-momentum distributions of the hard jet and the decay leptons, and of the missing transverse momentum, which are shown in Figure 23. Here, the behaviour of the more exclusive NLO observables can in principle be explained in the same way as for LHC: the LO results overestimate the cross section at high scales and underestimate it at low scales due to the fixed renormalization scale used in the calculation. As already observed when considering integrated cross sections, the difference between the two NLO observables is quite small at the Tevatron, which can be understood

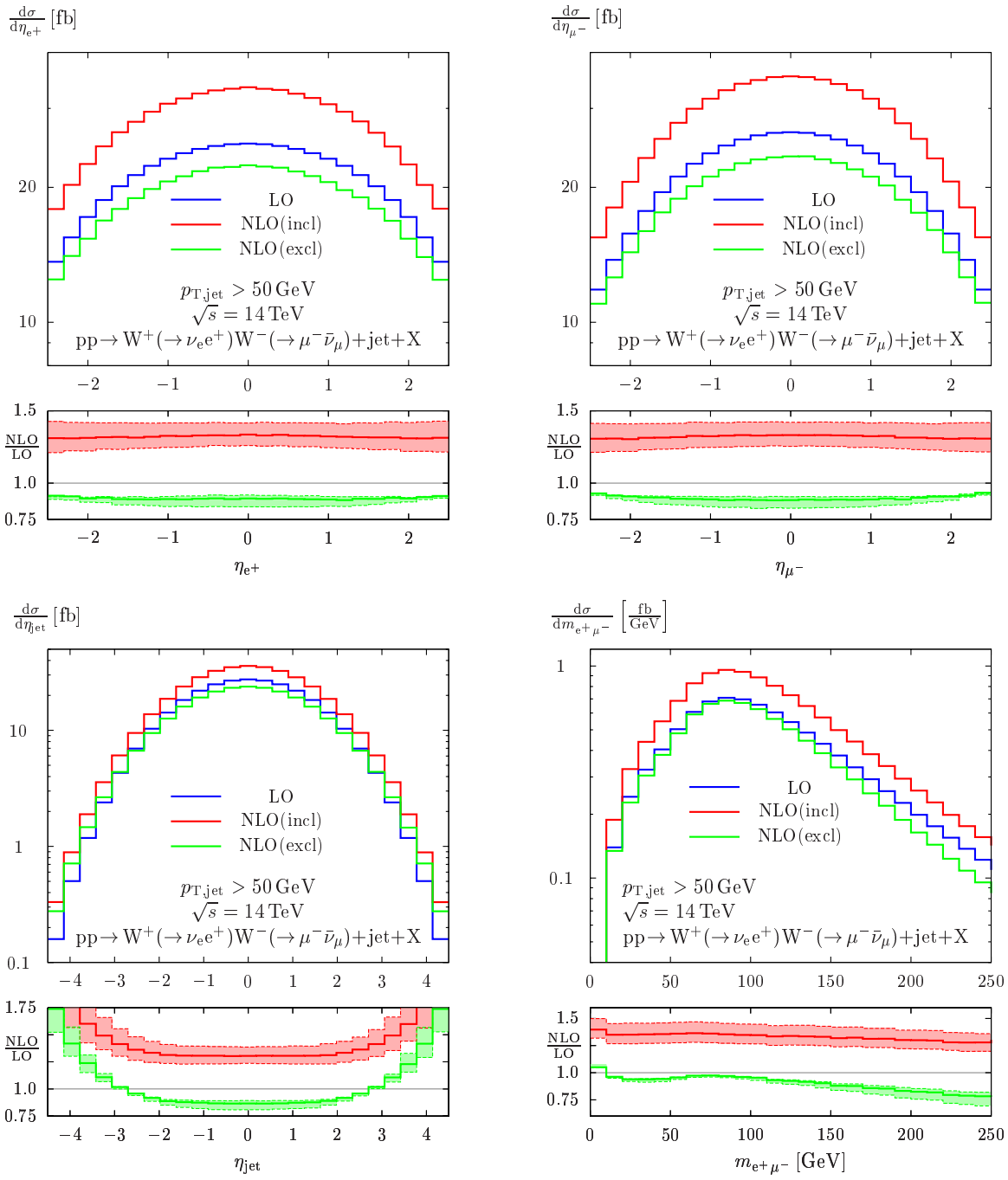

Figure 21: As in Figure 20, but for the pseudo-rapidity η of the charged decay leptons (upper plots), the pseudo-rapidity of the jet (lower left plot), and the invariant mass of the charged leptons (lower right plot).

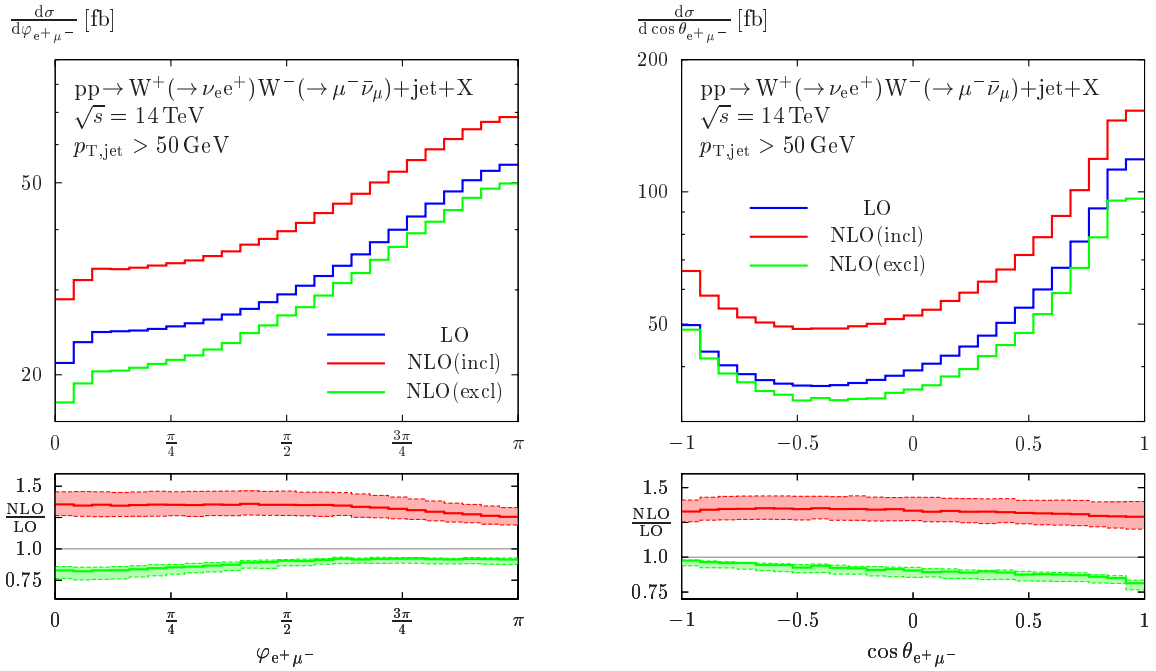

Figure 22: As in Figure 20, but for the angle φ in the transverse plane and the cosine of the opening angle θ between the two leptons.

from the smaller CM energy: In most cases, not enough energy is available for the production of a second hard jet. Therefore, the LO contributions of $p\bar{p} \to WW + 2jets + X$ contained in the more inclusive NLO observable only weaken the effect of negative corrections at large p_T, but do not overcompensate it as for the LHC setup. The p_T distributions of the two decay leptons are identical up to numerical fluctuations. This results from the fact that the hadronic process $p\bar{p} \to WW + jet + X$ and the underlying model (SM without $\mathcal{CP}$-violating phases) are invariant under $\mathcal{CP}$ transformation. Having not introduced any such $\mathcal{CP}$ violating contributions, we thus expect that the final state is also even under $\mathcal{CP}$ transformation. Thus, in contrast to proton–proton collisions, PDF effects do not cause differences between the p_T distributions of the leptons, since the quark PDFs of the proton equal the antiquark PDFs of the antiproton.

The distributions of the pseudo-rapidities η of the leptons, which are depicted in Figure 24, are not symmetric with respect to $\eta = 0$ due to the asymmetric hadronic initial state. Instead, the distributions of the lepton and the antilepton are identical if one of the distributions is mirrored around the $\eta = 0$ axes. In the Tevatron setup, the positive beam axes corresponds to the direction of the proton beam, and the negative axes to the antiproton beam. Correspondingly, positive η values describe momenta tending in the direction of the proton beam and vice versa.

Considering the non-symmetric pseudo-rapidity distributions, a tendency of the antilepton to the positive beam direction and, correspondingly, of the lepton to the negative beam direction is evident. To explain this, the argument of t-channel-like emission of W bosons can again be applied. As discussed in the LHC case, the W^+ boson, and consequently the antilepton, can only be emitted in this way from an up quark or a down antiquark. Since the $q\bar{q}$ channels dominate at the Tevatron, only these have to be taken into account for a qualitative discussion. On the average, these subprocesses do not produce boosted events in a distinguished direction due to the fact that the quark PDFs in the proton are equal to the respective antiquark PDFs in the antiproton. The contributions $u_p(p_1)\bar{u}_{\bar{p}}(p_2)$ and $d_p(p_1)\bar{d}_{\bar{p}}(p_2)$ dominate over the contributions

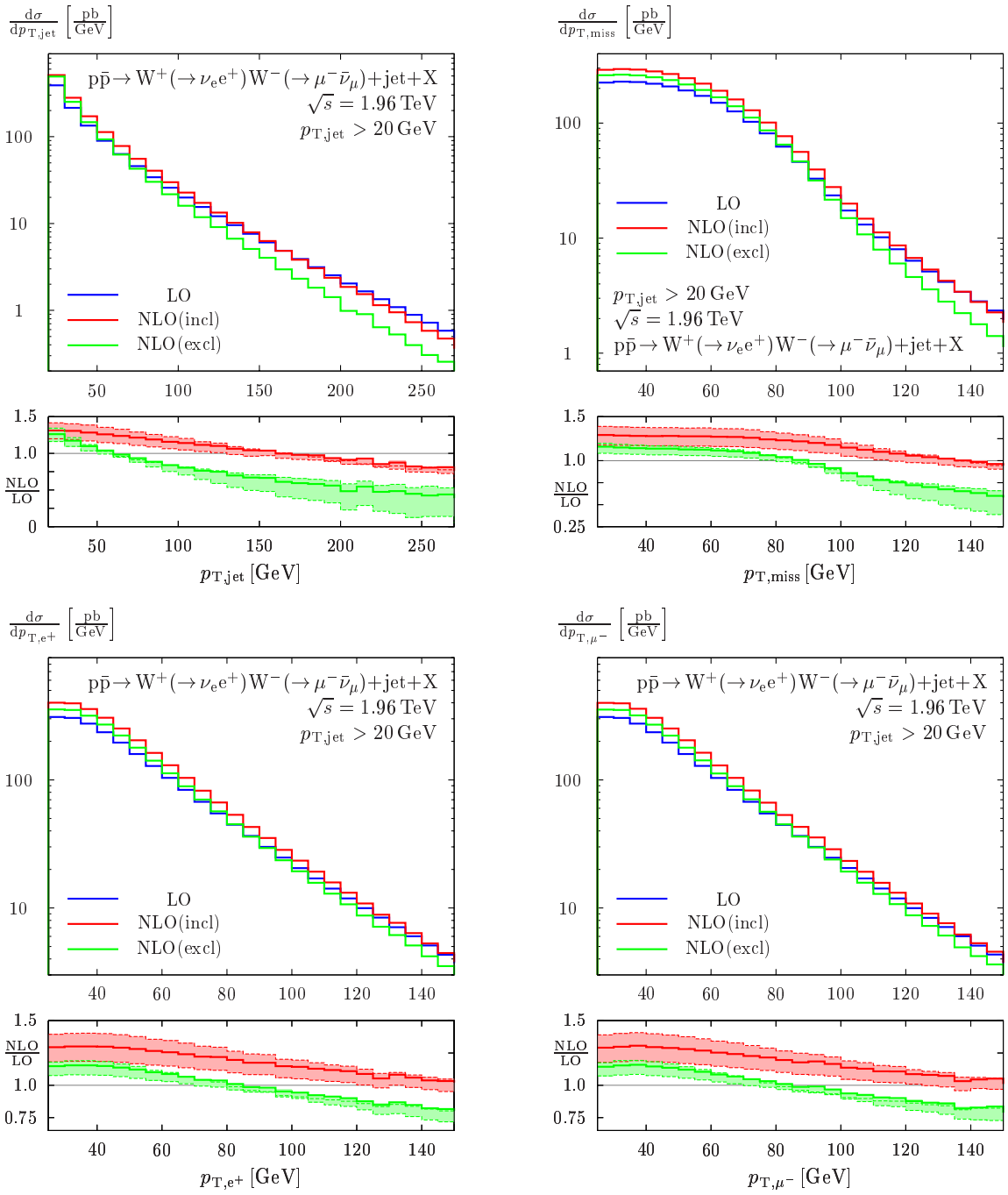

Figure 23: Differential cross sections for WW+jet with decays included in the improved NWA at the Tevatron: The LO and NLO distributions are shown for $\mu = \mu_{fact} = \mu_{ren} = M_W$. The distributions for the transverse momenta p_T of the jet and of the decay leptons, and for the missing transverse momentum $p_{T,miss}$ are depicted. The bands in the K-factors are defined as in the LHC case.

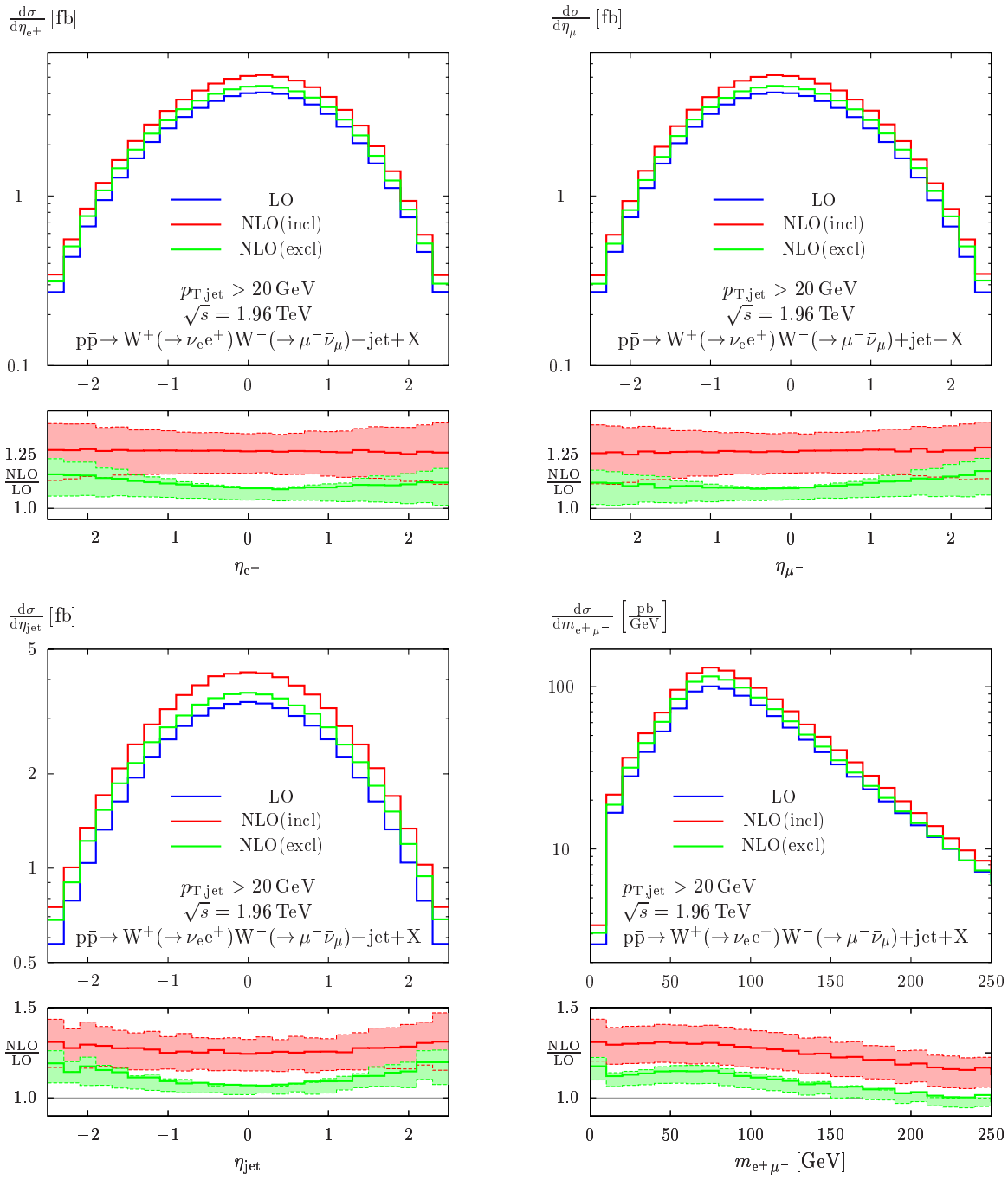

Figure 24: As in Figure 23, but for the pseudo-rapidity η of the charged decay leptons (upper plots), the pseudo-rapidity of the jet (lower left plot), and the invariant mass of the charged leptons (lower right plot).

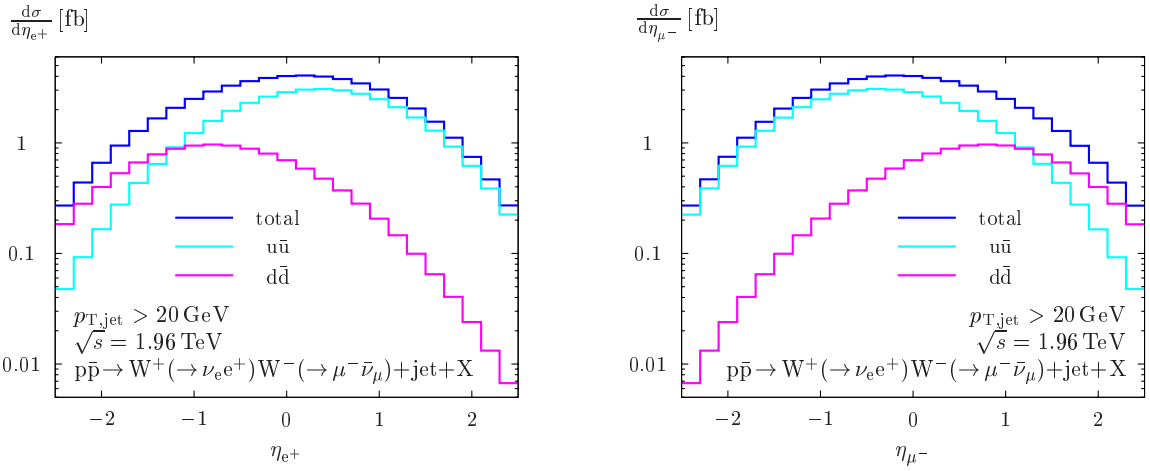

Figure 25: As in Figure 24, but only the LO distributions for the pseudo-rapidities η of the lepton and the antilepton are depicted. In addition, the two dominating partonic contributions $u\bar{u}$ and $d\bar{d}$ to the hadronic cross section are shown.

$\bar{u}_p(p_1)u_{\bar{p}}(p_2)$ and $\bar{d}_p(p_1)d_{\bar{p}}(p_2)$. Due to the effect of t-channel-like W^+ emission, the first tends to antilepton emission in the positive beam direction, the latter to the negative direction, as depicted in Figure 25. Since the $u\bar{u}$ channel exceeds the $d\bar{d}$ channel roughly by a factor 4 in total, a tendency to the positive beam direction results. The same argumentation holds, mutatis mutandis, for the lepton and the W^- boson.

The pseudo-rapidity of the jet, which is depicted in the lower left plot of Figure 24, is symmetric with respect to $\eta = 0$. This is due to the fact that no distinction can be made between hadronic jets arising from gluons, quarks, or antiquarks. Therefore, the sum over all contributions, which are $\mathcal{CP}$ symmetric in pairs, yields a symmetric distribution. As in the case of LHC, the dependence of the NLO corrections on the pseudo-rapidities of the jet and the leptons is moderate. Considering the absolute pseudo-rapidity dependence of the cross sections, a tendency to events that are not strongly boosted in the direction of the beam axes is observed. This can be understood from the fact that the dominating partonic channels with initial states of valence quark and valence antiquark are not strongly boosted in general.

The behaviour of the invariant-mass distribution of the two charged leptons, which is depicted in the lower right plot of Figure 24, can be explained analogously to the LHC case.

Finally, the angle correlations between the two decay leptons are considered. The angle in the transverse plane is again labelled by φ, and θ is the opening angle between the two leptons. The corresponding distributions are depicted in Figure 26. These angle correlations are very important also at Tevatron to distinguish the background process WW+jet from the signal process $H(\to WW^*)$+jet. Details on this topic are given in the discussion of the respective LHC distributions. Also in the Tevatron setup, the two leptons tend to fly into opposite directions in the transverse plane. In contrast to the situation at the LHC, this tendency is still observed in the $\cos\theta$ distribution of the opening angle θ, i.e. the effect is not overcompensated by boost effects. This is again understood from the fact that no tendency to strongly boosted events arises in the dominant partonic channels at the Tevatron.

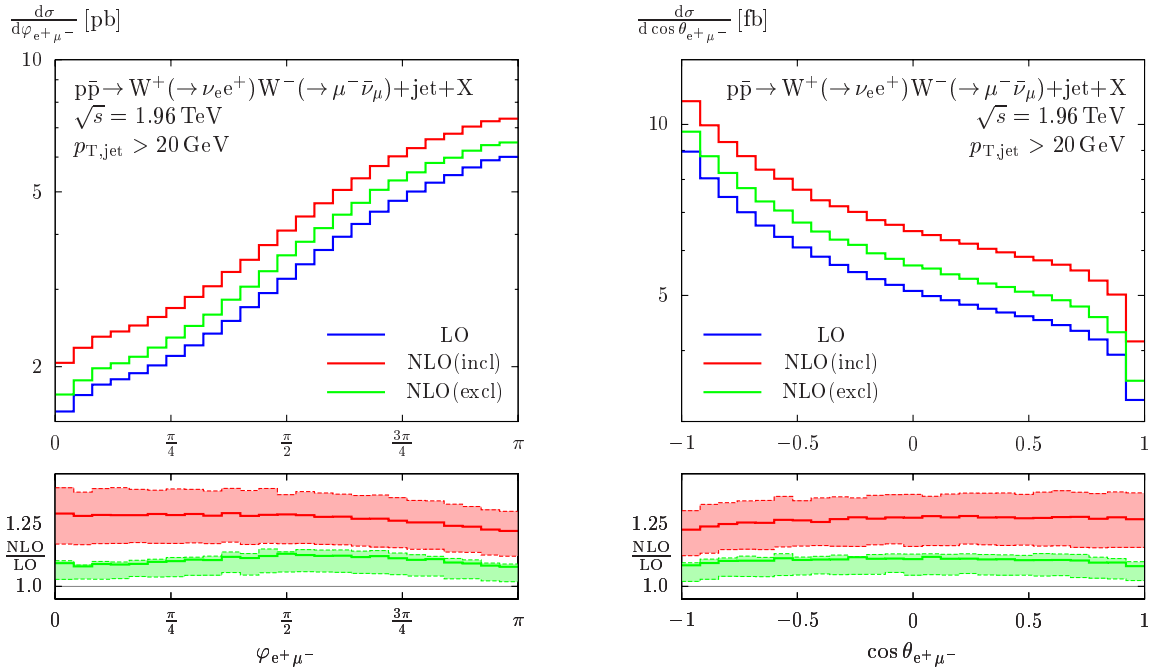

Figure 26: As in Figure 23, but for the angle φ in the transverse plane and the cosine of the opening angle θ between the two leptons.

5.4 Benchmark results and comparison to results of other groups

Independently of our calculation described in Ref. [9], two further groups have performed NLO QCD calculations on WW+jet production. The results of one of these groups are given in Ref. [10], while those of the second group are not published yet [11]. In Ref. [3], a tuned comparison of the three calculations is provided for the integrated LO cross section, which agree again within statistical errors, and of the virtual corrections at one specific phase-space point. There, the renormalized matrix elements are subdivided into bosonic and fermionic corrections with only the two light generations included in closed quark loops. The results are given in terms of the coefficients to the poles $\frac{1}{\epsilon^2}$ and $\frac{1}{\epsilon}$, and the finite part, i.e. in a way that is independent of the specific method for cancelling the infrared singularities.[4] A comparison of results for the third-generation loops has not been performed so far. Agreement is achieved between the results of the three groups at an accuracy level comparable to our internal checks.

6 Conclusions

The production of W-boson pairs in association with a hard jet is an important source for background to Higgs and new-physics searches both at the Tevatron and at the LHC. A proper

[4]Unfortunately an important detail was not explicitly stated in Ref. [10]: In the dipole subtraction method the IR divergences are usually factorized from D-dimenional LO structures ("conventional dimensional regularization"). In the comparison shown in Ref. [10], however, absolute numbers on the corrections to the squared matrix elements are given where the D-dimenional LO structures are evaluated in four dimensions (without expanding around $D = 4$). This procedure is legitimate, because the same replacement of D-dimensional by four-dimensional LO structures is done in the IR-divergent part of the real corrections. The numbers given in Ref. [10] are, thus, equivalent to results in the "'t Hooft–Veltman scheme" for dimensional regularization where only particles in loops or in singular splittings are extended to D dimensions.

theoretical prediction for this process requires at least the inclusion of perturbative QCD corrections at the next-to-leading order.

Continuing previous work, we have described in detail the calculation of these corrections, which takes into account leptonic decays of the W bosons. To this end, we employ an improved narrow-width approximation that treats the W bosons as on-shell particles, but keeps the W-spin information. While the naive narrow-width approximation, which neglects the information on the W spins, is only good within 5–10% in differential distributions, the improved version roughly reaches percent accuracy. This is the result of a comparison of leading-order predictions in these two approximations with results of a calculation fully based on off-shell W bosons.

The treatment of bottom quarks in the initial or final states deserves particular attention. Numerically such contributions only play a significant role if the top-quark propagator present in this case becomes resonant. The contributions are thus essentially the off-shell continuations of $W^+\bar{t}$, W^-t, or $t\bar{t}$ production including the subsequent decay of the top-quarks. These subprocesses, however, should not be counted as part of WW+jet production. Therefore, we have excluded contributions from external bottom quarks. The reliability of our procedure has been verified in a comparison of next-to-leading-order results obtained in two different schemes, where one is based on four, another on five active quark flavours in the proton.

Our detailed discussion of numerical results shows that the QCD corrections stabilize the leading-order prediction for the WW+jet cross section considerably with respect to a variation of the factorization and renormalization scales which we identify with each other. At the LHC, this stabilization of the prediction, however, requires a veto on a second hard jet. Otherwise the production of final states with WW+2jets, which yields a leading-order component of the next-to-leading-order correction, introduces again a large scale dependence. As far as the differential distributions are concerned the corrections are typically of the order of about 25%. For a remarkable number of distributions the K-factor is only mildly dependent on the kinematical region. At the LHC the η distributions in the dominant region and also the distributions in the angles between the two charged leptons have an almost constant K-factor of about 1.3 (inclusive cross-section definition); for the exclusive cross-section definition the corrections are even smaller and rather close to 1. The p_T spectra, on the other hand, show a much more phase-space-dependent K-factor with the exclusive cross-section definition showing an even larger dependence than the inclusive one. This is not surprising since the p_T introduces an additional scale which could introduce potentially large logarithms which are badly treated by a constant renormalization scale. At the Tevatron our findings are similar. Again the η and angular distributions receive corrections in form of an almost constant K-factor of about 1.3 (exclusive definition). The corrections for the exclusive cross-section definition are again smaller than for the inclusive definition. In case of the p_T spectra we observe again a phase-space-dependent K-factor. We note that the almost constant K-factor which holds for a remarkable number of distributions has also been observed by Campbell, Ellis and Zanderighi [10].

The QCD corrections to the related processes of ZZ+jet and WZ+jet production can be obtained in an analogous way as presented here for WW+jet. The corresponding calculations are in progress.

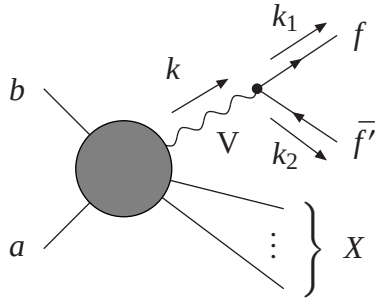

Figure 27: Schematic diagram for the process $ab \to \mathrm{V}X \to f\bar{f}'X$.

Acknowledgements

This work is supported in part by the European Community's Marie-Curie Research Training Network under contract MRTN-CT-2006-035505 "Tools and Precision Calculations for Physics Discoveries at Colliders" and by Deutsche Forschungsgemeinschaft (DFG) through SFB-TR 9 "Computational Theoretical Particle Physics". P.U. acknowledges the support of the Initiative and Networking Fund of the Helmholtz Association, contract HA-101 ("Physics at the Terascale").

Appendix

A Decaying on-shell gauge bosons

In this appendix we describe a simple method to include gauge-boson decays with the correct spin correlations in processes for which the helicity amplitudes for on-shell gauge bosons are already known. Specifically we consider the situation illustrated in Figure 27 where the vector boson V with momentum k decays into the pair $f(k_1)\bar{f}'(k_2)$ of massless fermions with momenta $k_{1,2}$. We start with the expression for the cross section

$$\sigma_{ab\to \mathrm{V}X\to f\bar{f}'X} = \frac{1}{2s_{ab}} \int \mathrm{d}\Phi_{f\bar{f}'X} \left|\mathcal{M}_{ab\to \mathrm{V}X\to f\bar{f}'X}\right|^2 \tag{A.1}$$

for the full reaction $ab \to \mathrm{V}X \to f\bar{f}'X$ integrated over its phase space $\Phi_{f\bar{f}'X}$ at the CM energy $\sqrt{s_{ab}}$. Of course, not only diagrams with a V resonance, as shown in Figure 27, contribute to the full amplitude $\mathcal{M}_{ab\to \mathrm{V}X\to f\bar{f}'X}$. We are, however, interested in the resonant diagrams which factorize according to

$$\mathcal{M}^{(\mathrm{res})}_{ab\to \mathrm{V}X\to f\bar{f}'X} = T_\mu(k) \frac{-1}{k^2 - M_\mathrm{V}^2 + \mathrm{i}M_\mathrm{V}\Gamma_\mathrm{V}} j^\mu(k_1,k_2), \tag{A.2}$$

where $T_\mu(k)$ describes the production of an off-shell V and $j^\mu(k_1,k_2)$ is the current of the V decay. For small decay widths Γ_V of V the phase-space integral (A.1) is dominated by the resonant diagrams with momenta near the mass shell of V. In order to extract the resonant terms, we factorize the phase space into V production and decay as follows,

$$\int \mathrm{d}\Phi_{f\bar{f}'X} \frac{1}{|k^2 - M_\mathrm{V}^2 + \mathrm{i}M_\mathrm{V}\Gamma_\mathrm{V}|^2} \cdots$$

$$
\begin{aligned}
&= \int \frac{\mathrm{d}k^2}{2\pi}\,\frac{1}{|k^2 - M_\mathrm{V}^2 + \mathrm{i}M_\mathrm{V}\Gamma_\mathrm{V}|^2}\int \mathrm{d}\Phi_{\mathrm{V}X}(k)\int \mathrm{d}\Phi_{f\bar{f}'}(k_1,k_2)\cdots \\
&\xrightarrow{\Gamma_\mathrm{V}\to 0} \int \frac{\mathrm{d}k^2}{2\pi}\,\frac{\pi}{M_\mathrm{V}\Gamma_\mathrm{V}}\,\delta(k^2 - M_\mathrm{V}^2)\int \mathrm{d}\Phi_{\mathrm{V}X}(k)\int \mathrm{d}\Phi_{f\bar{f}'}(k_1,k_2)\cdots \\
&= \frac{1}{2M_\mathrm{V}\Gamma_\mathrm{V}}\int \mathrm{d}\Phi_{\mathrm{V}X}(\hat{k})\int \mathrm{d}\Phi_{f\bar{f}'}(\hat{k}_1,\hat{k}_2)\cdots, \qquad \text{(A.3)}
\end{aligned}
$$

where the hats over the momenta indicate that the on-shell condition $\hat{k}^2 = (\hat{k}_1+\hat{k}_2)^2 = M_\mathrm{V}^2$ is fulfilled. On resonance we can decompose the contraction $T_\mu j^\mu$ into helicity amplitudes $\mathcal{M}_{ab\to\mathrm{V}X}$ and $\mathcal{M}_{\mathrm{V}\to f\bar{f}'}$ for the V production and decay upon inserting the completeness relation for the V polarization vectors $\varepsilon^\mu(\lambda)$,

$$
\begin{aligned}
-T_\mu(\hat{k})j^\mu(\hat{k}_1,\hat{k}_2) &= T_\mu(\hat{k})\left(\sum_{\lambda=0,\pm1}\varepsilon_\mathrm{V}^\mu(\lambda)^*\varepsilon_\mathrm{V}^\nu(\lambda) - \frac{\hat{k}^\mu\hat{k}^\nu}{M_\mathrm{V}^2}\right) j_\nu(\hat{k}_1,\hat{k}_2) \\
&= \sum_{\lambda=0,\pm1}\mathcal{M}_{ab\to\mathrm{V}X}(\lambda)\,\mathcal{M}_{\mathrm{V}\to f\bar{f}'}(\lambda) \qquad \text{(A.4)}
\end{aligned}
$$

where we have used current conservation $\hat{k}^\nu j_\nu(\hat{k}_1,\hat{k}_2) = 0$ (for massless fermions) and identified

$$
\mathcal{M}_{ab\to\mathrm{V}X}(\lambda) = T_\mu(\hat{k})\varepsilon_\mathrm{V}^\mu(\lambda)^*, \qquad \mathcal{M}_{\mathrm{V}\to f\bar{f}'}(\lambda) = \varepsilon_\mathrm{V}^\nu(\lambda)\,j_\nu(\hat{k}_1,\hat{k}_2). \qquad \text{(A.5)}
$$

In summary, the cross section in resonance approximation reads

$$
\begin{aligned}
\sigma_{ab\to\mathrm{V}X\to f\bar{f}'X} \xrightarrow{\Gamma_\mathrm{V}\to 0} &\frac{1}{2s_{ab}}\int \mathrm{d}\Phi_{\mathrm{V}X}(\hat{k})\sum_{\lambda,\lambda'=0,\pm1}\mathcal{M}_{ab\to\mathrm{V}X}(\lambda')^*\mathcal{M}_{ab\to\mathrm{V}X}(\lambda) \\
&\times\frac{1}{2M_\mathrm{V}\Gamma_\mathrm{V}}\int \mathrm{d}\Phi_{f\bar{f}'}(\hat{k}_1,\hat{k}_2)\,\mathcal{M}_{\mathrm{V}\to f\bar{f}'}(\lambda')^*\mathcal{M}_{\mathrm{V}\to f\bar{f}'}(\lambda). \qquad \text{(A.6)}
\end{aligned}
$$

If the phase space of the decay fermions is integrated over completely, rotational invariance implies that

$$
\frac{1}{2M_\mathrm{V}}\int \mathrm{d}\Phi_{f\bar{f}'}(\hat{k}_1,\hat{k}_2)\,\mathcal{M}_{\mathrm{V}\to f\bar{f}'}(\lambda')^*\mathcal{M}_{\mathrm{V}\to f\bar{f}'}(\lambda) = \Gamma_{\mathrm{V}\to f\bar{f}'}\,\delta_{\lambda'\lambda}, \qquad \text{(A.7)}
$$

where $\Gamma_{\mathrm{V}\to f\bar{f}'}$ is the partial decay width. Inserting this result into (A.6), yields the usual narrow-width approximation for the cross section,

$$
\begin{aligned}
\sigma_{ab\to\mathrm{V}X\to f\bar{f}'X} &\xrightarrow{\Gamma_\mathrm{V}\to 0} \frac{1}{2s_{ab}}\int \mathrm{d}\Phi_{\mathrm{V}X}(\hat{k})\sum_{\lambda=0,\pm1}|\mathcal{M}_{ab\to\mathrm{V}X}(\lambda)|^2\,\mathrm{BR}_{\mathrm{V}\to f\bar{f}'} \\
&= \sigma_{ab\to\mathrm{V}X}\,\mathrm{BR}_{\mathrm{V}\to f\bar{f}'}, \qquad \text{(A.8)}
\end{aligned}
$$

with $\sigma_{ab\to\mathrm{V}X}$ denoting the production cross section for unpolarized vector bosons V and $\mathrm{BR}_{\mathrm{V}\to f\bar{f}'} = \Gamma_{\mathrm{V}\to f\bar{f}'}/\Gamma_\mathrm{V}$ denoting the branching ratio for the decay of V into the $f\bar{f}'$ pair.

If the decay fermions are not integrated over the full phase space $\Phi_{f\bar{f}'}$, i.e. if cuts on the fermions are applied or if distributions in the fermion kinematics are considered, it is convenient to introduce the "decay correlation matrix"

$$
\Delta_{\lambda'\lambda}^{\mathrm{V}\to f\bar{f}'}(\hat{k}_1,\hat{k}_2) = \frac{\Phi_{f\bar{f}'}}{2M_\mathrm{V}\Gamma_{\mathrm{V}\to f\bar{f}'}}\,\mathcal{M}_{\mathrm{V}\to f\bar{f}'}(\lambda')^*\mathcal{M}_{\mathrm{V}\to f\bar{f}'}(\lambda), \qquad \text{(A.9)}
$$

so that the full cross section takes the form

$$\sigma_{ab\to \mathrm{V}X\to f\bar{f}'X} \;\widetilde{\Gamma_{\mathrm{V}}\to 0}\; \frac{1}{2s_{ab}}\int \mathrm{d}\Phi_{\mathrm{V}X}(\hat{k}) \sum_{\lambda,\lambda'=0,\pm 1} \mathcal{M}_{ab\to \mathrm{V}X}(\lambda')^* \mathcal{M}_{ab\to \mathrm{V}X}(\lambda)$$
$$\times \mathrm{BR}_{\mathrm{V}\to f\bar{f}'} \int \frac{\mathrm{d}\Phi_{f\bar{f}'}(\hat{k}_1,\hat{k}_2)}{\Phi_{f\bar{f}'}} \Delta^{\mathrm{V}\to f\bar{f}'}_{\lambda'\lambda}(\hat{k}_1,\hat{k}_2), \tag{A.10}$$

where $\Phi_{f\bar{f}'}$ is the volume of the $f\bar{f}'$ phase space $\int \mathrm{d}\Phi_{f\bar{f}'}(\hat{k}_1,\hat{k}_2)$. The matrix $\Delta^{\mathrm{V}\to f\bar{f}'}$ is widely independent of the production process. Only the V helicity states entering $\Delta^{\mathrm{V}\to f\bar{f}'}$ must be the same as in the production. The explicit calculation of $\Delta^{\mathrm{V}\to f\bar{f}'}$ is conveniently performed in the rest frame of V. Defining the momentum and the polarization vectors of V in the CM frame Σ of ab by[5]

$$\begin{aligned}
\hat{k}^\mu &= E_{\mathrm{V}}(1,\beta_{\mathrm{V}}\cos\phi_{\mathrm{V}}\sin\theta_{\mathrm{V}},\beta_{\mathrm{V}}\sin\phi_{\mathrm{V}}\sin\theta_{\mathrm{V}},\beta_{\mathrm{V}}\cos\theta_{\mathrm{V}}), \quad \beta_{\mathrm{V}} = \sqrt{1-M_{\mathrm{V}}^2/E_{\mathrm{V}}^2},\\
\varepsilon^\mu_{\mathrm{V}}(\pm 1) &= \frac{\mathrm{e}^{\mp \mathrm{i}\phi_{\mathrm{V}}}}{\sqrt{2}}(0,-\cos\phi_{\mathrm{V}}\cos\theta_{\mathrm{V}} \pm \mathrm{i}\sin\phi_{\mathrm{V}}, -\sin\phi_{\mathrm{V}}\cos\theta_{\mathrm{V}} \mp \mathrm{i}\cos\phi_{\mathrm{V}},\sin\theta_{\mathrm{V}}),\\
\varepsilon^\mu_{\mathrm{V}}(0) &= \gamma_{\mathrm{V}}(\beta_{\mathrm{V}},\cos\phi_{\mathrm{V}}\sin\theta_{\mathrm{V}},\sin\phi_{\mathrm{V}}\sin\theta_{\mathrm{V}},\cos\theta_{\mathrm{V}}), \quad \gamma_{\mathrm{V}} = 1/\sqrt{1-\beta_{\mathrm{V}}^2} = E_{\mathrm{V}}/M_{\mathrm{V}},
\end{aligned} \tag{A.11}$$

we transform them into the rest frame $\tilde{\Sigma}$ of V with the Lorentz transformation matrix

$$\left(\Lambda^\mu{}_\nu\right) = \begin{pmatrix} \gamma_{\mathrm{V}} & 0 & 0 & -\beta_{\mathrm{V}}\gamma_{\mathrm{V}} \\ 0 & 1 & 0 & 0 \\ 0 & 0 & 1 & 0 \\ -\beta_{\mathrm{V}}\gamma_{\mathrm{V}} & 0 & 0 & \gamma_{\mathrm{V}} \end{pmatrix} \begin{pmatrix} 1 & 0 & 0 & 0 \\ 0 & \cos\phi_{\mathrm{V}}\cos\theta_{\mathrm{V}} & \sin\phi_{\mathrm{V}}\cos\theta_{\mathrm{V}} & -\sin\theta_{\mathrm{V}} \\ 0 & -\sin\phi_{\mathrm{V}} & \cos\phi_{\mathrm{V}} & 0 \\ 0 & \cos\phi_{\mathrm{V}}\sin\theta_{\mathrm{V}} & \sin\phi_{\mathrm{V}}\sin\theta_{\mathrm{V}} & \cos\theta_{\mathrm{V}} \end{pmatrix}, \tag{A.12}$$

which is factorized into a rotation in Σ (rotating $\mathbf{k}$ to the z axis) and a boost along the new V direction. The explicit results for the considered vectors $\tilde{a}^\mu = \Lambda^\mu{}_\nu a^\nu$ in $\tilde{\Sigma}$ are

$$\tilde{\hat{k}}^\mu = (M_{\mathrm{V}},0,0,0), \quad \tilde{\varepsilon}^\mu_{\mathrm{V}}(\pm 1) = \frac{\mathrm{e}^{\mp \mathrm{i}\phi_{\mathrm{V}}}}{\sqrt{2}}(0,-1,\mp\mathrm{i},0), \quad \tilde{\varepsilon}^\mu_{\mathrm{V}}(0) = (0,0,0,1). \tag{A.13}$$

In $\tilde{\Sigma}$ the decay momenta $\tilde{\hat{k}}_{1,2}$ are distributed isotropically and parametrized by

$$\tilde{\hat{k}}_1^\mu = \frac{M_{\mathrm{V}}}{2}(1,\cos\tilde{\phi}_1\sin\tilde{\theta}_1,\sin\tilde{\phi}_1\sin\tilde{\theta}_1,\cos\tilde{\theta}_1), \quad \tilde{\hat{k}}_2^\mu = \tilde{\hat{k}}^\mu - \tilde{\hat{k}}_1^\mu. \tag{A.14}$$

Equipped with these kinematical definitions we evaluate the decay matrix elements

$$\mathcal{M}^\sigma_{\mathrm{V}\to f\bar{f}'}(\lambda) = e g^\sigma_{\mathrm{V}ff'} \bar{u}_f(\tilde{\hat{k}}_1) \tilde{\not{\varepsilon}}(\lambda) \omega_\sigma v_{\bar{f}'}(\tilde{\hat{k}}_2), \tag{A.15}$$

where we made the chirality $\sigma = \pm$ explicit (which coincides with the sign of the helicity of f) and used an obvious notation for the Dirac spinors $\bar{u}_f$, $v_{\bar{f}'}$ and the chirality projectors $\omega_\pm =$

[5] For $\varepsilon^\mu_{\mathrm{V}}(\lambda)$ this choice follows the phase convention of Ref. [43].

$(1\pm\gamma_5)/2$. The chiral couplings $g^{\sigma}_{\mathrm{V}ff'}$ are defined as in (4.5). Ordering the λ values according to $(+,0,-)$, the decay amplitudes can be written as

$$\begin{aligned}
\mathcal{M}^{+}_{\mathrm{V}\to f\bar{f}'}(\lambda) &= e g^{+}_{\mathrm{V}ff'} M_{\mathrm{V}} \left(+\tfrac{1}{\sqrt{2}} \mathrm{e}^{\mathrm{i}(\tilde{\phi}_1-\phi_{\mathrm{V}})}(1+\cos\tilde{\theta}_1), \sin\tilde{\theta}_1, -\tfrac{1}{\sqrt{2}} \mathrm{e}^{-\mathrm{i}(\tilde{\phi}_1-\phi_{\mathrm{V}})}(1-\cos\tilde{\theta}_1) \right), \\
\mathcal{M}^{-}_{\mathrm{V}\to f\bar{f}'}(\lambda) &= e g^{-}_{\mathrm{V}ff'} M_{\mathrm{V}} \left(-\tfrac{1}{\sqrt{2}} \mathrm{e}^{\mathrm{i}(\tilde{\phi}_1-\phi_{\mathrm{V}})}(1-\cos\tilde{\theta}_1), \sin\tilde{\theta}_1, +\tfrac{1}{\sqrt{2}} \mathrm{e}^{-\mathrm{i}(\tilde{\phi}_1-\phi_{\mathrm{V}})}(1+\cos\tilde{\theta}_1) \right).
\end{aligned} \tag{A.16}$$

Inserting these amplitudes into (A.9) and summing over fermion helicities, we obtain for the (hermitian) decay correlation matrix

$$\begin{aligned}
\Delta^{\mathrm{V}\to f\bar{f}'} = {} & 3c^{+}_{\mathrm{V}ff'} \begin{pmatrix} \frac{1}{4}(1+\cos\tilde{\theta}_1)^2 & * & * \\ \frac{\mathrm{e}^{\mathrm{i}(\tilde{\phi}_1-\phi_{\mathrm{V}})}}{2\sqrt{2}}(1+\cos\tilde{\theta}_1)\sin\tilde{\theta}_1 & \frac{1}{2}\sin^2\tilde{\theta}_1 & * \\ -\frac{\mathrm{e}^{2\mathrm{i}(\tilde{\phi}_1-\phi_{\mathrm{V}})}}{4}\sin^2\tilde{\theta}_1 & -\frac{\mathrm{e}^{\mathrm{i}(\tilde{\phi}_1-\phi_{\mathrm{V}})}}{2\sqrt{2}}(1-\cos\tilde{\theta}_1)\sin\tilde{\theta}_1 & \frac{1}{4}(1-\cos\tilde{\theta}_1)^2 \end{pmatrix} \\
& + 3c^{-}_{\mathrm{V}ff'} \begin{pmatrix} \frac{1}{4}(1-\cos\tilde{\theta}_1)^2 & * & * \\ -\frac{\mathrm{e}^{\mathrm{i}(\tilde{\phi}_1-\phi_{\mathrm{V}})}}{2\sqrt{2}}(1-\cos\tilde{\theta}_1)\sin\tilde{\theta}_1 & \frac{1}{2}\sin^2\tilde{\theta}_1 & * \\ -\frac{\mathrm{e}^{2\mathrm{i}(\tilde{\phi}_1-\phi_{\mathrm{V}})}}{4}\sin^2\tilde{\theta}_1 & \frac{\mathrm{e}^{\mathrm{i}(\tilde{\phi}_1-\phi_{\mathrm{V}})}}{2\sqrt{2}}(1+\cos\tilde{\theta}_1)\sin\tilde{\theta}_1 & \frac{1}{4}(1+\cos\tilde{\theta}_1)^2 \end{pmatrix},
\end{aligned} \tag{A.17}$$

where we used the shorthand

$$c^{\sigma}_{\mathrm{V}ff'} = \frac{(g^{\sigma}_{\mathrm{V}ff'})^2}{(g^{+}_{\mathrm{V}ff'})^2 + (g^{-}_{\mathrm{V}ff'})^2}, \qquad c^{+}_{\mathrm{V}ff'} + c^{-}_{\mathrm{V}ff'} = 1. \tag{A.18}$$

From this result it is obvious that the full integration of the decay phase space yields

$$\int \frac{\mathrm{d}\Phi_{f\bar{f}'}(\hat{k}_1,\hat{k}_2)}{\Phi_{f\bar{f}'}} \Delta^{\mathrm{V}\to f\bar{f}'}(\hat{k}_1,\hat{k}_2) = \int \frac{\mathrm{d}\tilde{\Omega}_f}{4\pi} \Delta^{\mathrm{V}\to f\bar{f}'}(\tilde{\hat{k}}_1,\tilde{\hat{k}}_2) = \mathbf{1}, \tag{A.19}$$

as it should be for an isotropic decay in the rest frame of V.

B Benchmark numbers for the virtual corrections

In order to facilitate a comparison to our calculation, we provide explicit numbers on the squared LO amplitude and the corresponding virtual corrections for a single non-exceptional phase-space point. The set of momenta for $ab \to \mathrm{W}^+(\to \nu_{\mathrm{e}}\mathrm{e}^+)\mathrm{W}^-(\to \mu^-\bar{\nu}_{\mu})c$ with the explicit partonic reactions $\mathrm{q}\bar{\mathrm{q}}\to \mathrm{W}^+\mathrm{W}^-\mathrm{g}$, $\mathrm{q}\bar{\mathrm{g}}\to \mathrm{W}^+\mathrm{W}^-\mathrm{q}$, and $\mathrm{g}\bar{\mathrm{q}}\to \mathrm{W}^+\mathrm{W}^-\bar{\mathrm{q}}$ is chosen as

$$\begin{aligned}
p_a &= (250,0,0,250), \\
p_b &= (250,0,0,-250), \\
p_{\nu_{\mathrm{e}}} &= (49.43764668100422,-18.32747340442861,-42.74042990560614,16.77618190917520), \\
p_{\mathrm{e}^+} &= (175.4405115231198,-125.7805594116281,-26.45739027367693,119.4095073999478), \\
p_{\mu^-} &= (32.78781503058663,-29.71117802999691,7.333312535152912,-11.76899493633845), \\
p_{\bar{\nu}_{\mu}} &= (81.55218598686336,45.19373677627630,61.86450764413016,-27.94759183511103), \\
p_c &= (160.7818407784260,128.6254740697773,0,-96.46910253767348),
\end{aligned} \tag{A.1}$$

with the obvious notation $p = (p^0, p^1, p^2, p^3)$ and all the components given in GeV. Note that the presented results are calculated using the improved NWA, i.e. with the W bosons on-shell, but with their spin information kept.

Factoring out the couplings for the Born amplitude, we define

$$\frac{1}{4}\frac{1}{N_c}\sum_{\text{spin,colour}} |\mathcal{M}_{\text{LO}}|^2 = e^4 g_s^2 a_0, \tag{A.2}$$

where

$$|\mathcal{M}_{\text{LO}}|^2 = \sum_{\lambda_+,\lambda'_+,\lambda_-,\lambda'_-=0,\pm1} \mathcal{M}_{ab\to \text{W}^+\text{W}^- c}(\lambda'_+,\lambda'_-)^* \mathcal{M}_{ab\to \text{W}^+\text{W}^- c}(\lambda_+,\lambda_-) \times \Delta^{\text{W}^+\to \nu_\text{e}\text{e}^+}_{\lambda'_+\lambda_+}(\hat{k}_{\nu_\text{e}},\hat{k}_{\text{e}^+})\Delta^{\text{W}^-\to \mu^-\bar{\nu}_\mu}_{\lambda'_-\lambda_-}(\hat{k}_{\mu^-},\hat{k}_{\bar{\nu}_\mu}) \tag{A.3}$$

with the definitions of App. A. The factor $1/N_c$ is due to the average over the incoming colour. For the channel $\text{q}\bar{\text{q}}$, qg, $\text{g}\bar{\text{q}}$ we have$N_c = 9, 24, 24$, respectively.

The finite remainder of the virtual amplitudes after renormalization and addition of the $\mathcal{I}$ operator defines the relative correction c_0 according to

$$\frac{1}{4}\frac{1}{N_c}\sum_{\text{spin,colour}} 2\text{Re}\left(\left(\mathcal{M}_{\text{virt}} + \mathcal{M}_{\text{ct}} + \mathcal{M}_{\mathcal{I}-\text{op}}\right)^* \mathcal{M}_{\text{LO}}\right) = e^4 g_s^2 a_0\, c_0, \tag{A.4}$$

where $\mathcal{M}_{\text{virt}}$, $\mathcal{M}_{\text{ct}}$, and $\mathcal{M}_{\mathcal{I}-\text{op}}$ are defined in analogy to (A.3).

The results of our independent calculations at the sample phase-space point (A.1) are collected in Table 5 in terms of a_0 and c_0, namely for the six different partonic insertions for *a*, *b*, and *c*.

For the LO amplitudes we find an agreement of at least 14 digits—as expected from a calculation using 64bit double precision. For the finite remainder of the one-loop corrections we find an agreement of at least 8 digits.

C Tables for histograms

In this appendix we present the tables corresponding to the differential distributions presented in Section 5.3.2. For each distribution, we list all predictions for the LO cross section and for both definitions of NLO cross sections—namely NLO (excl) and NLO (incl)—with the scale choice $\mu = \mu_{\text{ren}} = \mu_{\text{fact}} = M_\text{W}$. The given errors result from the Monte Carlo integration. The bin is specified by its central value. The bin width—which we chose constant for the entire histogram—is obtained from the distance of two neighboring bin positions.

References

[1] C. Buttar *et al.* [QCD, EW, and Higgs Working Group], arXiv:hep-ph/0604120.

[2] J. M. Campbell, J. W. Huston and W. J. Stirling, Rept. Prog. Phys. **70** (2007) 89 [arXiv:hep-ph/0611148].

[3] Z. Bern *et al.* [NLO Multileg Working Group], arXiv:0803.0494 [hep-ph].

	$a_0[\mathrm{GeV}^{-2}]$	c_0
$u\bar{u} \to W^+(\to \nu_e e^+)W^-(\to \mu^- \bar{\nu}_\mu)g$		
Version 1	$0.1543423047392003 \cdot 10^{-4}$	-0.01279611285522559
Version 2	$0.1543423047392000 \cdot 10^{-4}$	-0.01279611284828043
$d\bar{d} \to W^+(\to \nu_e e^+)W^-(\to \mu^- \bar{\nu}_\mu)g$		
Version 1	$0.9381083061358519 \cdot 10^{-6}$	0.02297241368680441
Version 2	$0.9381083061358457 \cdot 10^{-6}$	0.02297241372542423
$ug \to W^+(\to \nu_e e^+)W^-(\to \mu^- \bar{\nu}_\mu)u$		
Version 1	$0.2766898219323333 \cdot 10^{-5}$	-0.04800046567722612
Version 2	$0.2766898219323326 \cdot 10^{-5}$	-0.04800046570175944
$dg \to W^+(\to \nu_e e^+)W^-(\to \mu^- \bar{\nu}_\mu)d$		
Version 1	$0.1995963102379381 \cdot 10^{-6}$	-0.08921487131748859
Version 2	$0.1995963102379386 \cdot 10^{-6}$	-0.08921487141443678
$g\bar{u} \to W^+(\to \nu_e e^+)W^-(\to \mu^- \bar{\nu}_\mu)\bar{u}$		
Version 1	$0.1351044519951966 \cdot 10^{-4}$	-0.2945621757876244
Version 2	$0.1351044519951967 \cdot 10^{-4}$	-0.2945621758243954
$g\bar{d} \to W^+(\to \nu_e e^+)W^-(\to \mu^- \bar{\nu}_\mu)\bar{d}$		
Version 1	$0.4409954556585700 \cdot 10^{-5}$	-0.08497157067204103
Version 2	$0.4409954556585692 \cdot 10^{-5}$	-0.08497157060895164

Table 5: Colour and spin averaged LO matrix elements squared and virtual corrections.

[4] A. Bredenstein, A. Denner, S. Dittmaier and S. Pozzorini, JHEP **0808** (2008) 108 [arXiv:0807.1248 [hep-ph]] and arXiv:0905.0110 [hep-ph];
G. Bevilacqua, M. Czakon, C. G. Papadopoulos, R. Pittau and M. Worek, arXiv:0907.4723 [hep-ph].

[5] R. K. Ellis, W. T. Giele, Z. Kunszt, K. Melnikov and G. Zanderighi, JHEP **0901** (2009) 012 [arXiv:0810.2762 [hep-ph]];
R. K. Ellis, K. Melnikov and G. Zanderighi, JHEP **0904** (2009) 077 [arXiv:0901.4101 [hep-ph]] and arXiv:0906.1445 [hep-ph];
C. F. Berger *et al.*, Phys. Rev. Lett. **102** (2009) 222001 [arXiv:0902.2760 [hep-ph]] and arXiv:0907.1984 [hep-ph].

[6] A. van Hameren, C. G. Papadopoulos and R. Pittau, arXiv:0903.4665 [hep-ph].

[7] B. Mellado, W. Quayle and S. L. Wu, Phys. Rev. D **76** (2007) 093007 [arXiv:0708.2507 [hep-ph]].

[8] G. Chachamis, M. Czakon and D. Eiras, JHEP **0812** (2008) 003 [arXiv:0802.4028 [hep-ph]] and arXiv:0806.3043 [hep-ph].

Table 6: Distribution of $p_{\mathrm{T,jet}}$ and $p_{\mathrm{T,miss}}$ at the LHC with $\mu = \mu_{\mathrm{ren}} = \mu_{\mathrm{fact}} = M_{\mathrm{W}}$.

$p_{\mathrm{T,miss}}$[GeV]	$\frac{d\sigma_{\mathrm{LO}}}{dp_{\mathrm{T,miss}}}\left[\frac{\mathrm{pb}}{\mathrm{GeV}}\right]$	$\frac{d\sigma_{\mathrm{NLO,excl}}}{dp_{\mathrm{T,miss}}}\left[\frac{\mathrm{pb}}{\mathrm{GeV}}\right]$	$\frac{d\sigma_{\mathrm{NLO,incl}}}{dp_{\mathrm{T,miss}}}\left[\frac{\mathrm{pb}}{\mathrm{GeV}}\right]$
27.5	1.10787(34)	1.1683(35)	1.5232(31)
32.5	1.21978(36)	1.2943(38)	1.6798(31)
37.5	1.28976(37)	1.3484(33)	1.7642(28)
42.5	1.32096(37)	1.3665(37)	1.7964(31)
47.5	1.31712(37)	1.3687(38)	1.8037(27)
52.5	1.28158(36)	1.3103(34)	1.7481(27)
57.5	1.22095(35)	1.2395(30)	1.6677(26)
62.5	1.14291(33)	1.1372(30)	1.5551(26)
67.5	1.06101(31)	1.0611(28)	1.4507(25)
72.5	0.97356(30)	0.9470(26)	1.3188(23)
77.5	0.88876(28)	0.8481(24)	1.1929(20)
82.5	0.80514(26)	0.7572(22)	1.0743(18)
87.5	0.72506(24)	0.6524(30)	0.9513(25)
92.5	0.64875(23)	0.5764(35)	0.8452(23)
97.5	0.57792(21)	0.4942(25)	0.7419(20)
102.5	0.51221(20)	0.4267(23)	0.6576(20)
107.5	0.45154(18)	0.3666(19)	0.5769(17)
112.5	0.39710(17)	0.3095(15)	0.5058(13)
117.5	0.34905(16)	0.2663(18)	0.4449(13)
122.5	0.30907(15)	0.2268(18)	0.3939(13)
127.5	0.27483(14)	0.1925(17)	0.3474(12)
132.5	0.24595(13)	0.1667(23)	0.3096(19)
137.5	0.22077(12)	0.1474(24)	0.2794(18)
142.5	0.19854(11)	0.1263(20)	0.2487(12)
147.5	0.17986(11)	0.1137(14)	0.2262(10)

$p_{\mathrm{T,jet}}$[GeV]	$\frac{d\sigma_{\mathrm{LO}}}{dp_{\mathrm{T,jet}}}\left[\frac{\mathrm{pb}}{\mathrm{GeV}}\right]$	$\frac{d\sigma_{\mathrm{NLO,excl}}}{dp_{\mathrm{T,jet}}}\left[\frac{\mathrm{pb}}{\mathrm{GeV}}\right]$	$\frac{d\sigma_{\mathrm{NLO,incl}}}{dp_{\mathrm{T,jet}}}\left[\frac{\mathrm{pb}}{\mathrm{GeV}}\right]$
55	1.47878(26)	1.7903(23)	1.8600(22)
65	1.19041(23)	1.3622(21)	1.5178(20)
75	0.98096(21)	1.0595(20)	1.2619(19)
85	0.82324(19)	0.8511(20)	1.0706(20)
95	0.70022(18)	0.6875(19)	0.9150(19)
105	0.60034(16)	0.5648(18)	0.7878(16)
115	0.51805(15)	0.4642(21)	0.6844(18)
125	0.45004(14)	0.3871(27)	0.5951(23)
135	0.39293(13)	0.3342(25)	0.5301(21)
145	0.34383(12)	0.2711(14)	0.4581(13)
155	0.30246(11)	0.2306(17)	0.4047(15)
165	0.26699(10)	0.1952(22)	0.3597(14)
175	0.236277(94)	0.1721(20)	0.3209(11)
185	0.209810(88)	0.1448(10)	0.28598(99)
195	0.186526(82)	0.11976(96)	0.25141(95)
205	0.166336(77)	0.1070(10)	0.23005(96)
215	0.148596(72)	0.0883(12)	0.20236(95)
225	0.133168(67)	0.0796(13)	0.1853(10)
235	0.119463(63)	0.0666(11)	0.1643(12)
245	0.107421(59)	0.05777(98)	0.1487(10)
255	0.096866(56)	0.05028(86)	0.13439(82)
265	0.087248(52)	0.04629(82)	0.12439(81)
275	0.078964(49)	0.03675(67)	0.11029(65)
285	0.071329(46)	0.03121(58)	0.09900(50)
295	0.064789(44)	0.02906(56)	0.09203(49)

Table 7: Distribution of p_{T,e^+} and p_{T,μ^-} at the LHC with $\mu = \mu_{ren} = \mu_{fact} = M_W$.

p_{T,μ^-} [GeV]	$\frac{d\sigma_{LO}}{dp_{T,\mu^-}}\left[\frac{pb}{GeV}\right]$	$\frac{d\sigma_{NLO,excl}}{dp_{T,\mu^-}}\left[\frac{pb}{GeV}\right]$	$\frac{d\sigma_{NLO,incl}}{dp_{T,\mu^-}}\left[\frac{pb}{GeV}\right]$	p_{T,e^+} [GeV]	$\frac{d\sigma_{LO}}{dp_{T,e^+}}\left[\frac{pb}{GeV}\right]$	$\frac{d\sigma_{NLO,excl}}{dp_{T,e^+}}\left[\frac{pb}{GeV}\right]$	$\frac{d\sigma_{NLO,incl}}{dp_{T,e^+}}\left[\frac{pb}{GeV}\right]$
27.5	1.75438(39)	1.7529(22)	2.3634(20)	27.5	2.21854(59)	2.1958(33)	3.0506(27)
32.5	1.72719(38)	1.7365(37)	2.3444(34)	32.5	2.08923(52)	2.0766(38)	2.8827(28)
37.5	1.63647(37)	1.6451(33)	2.2317(31)	37.5	1.89828(46)	1.8785(32)	2.6195(30)
42.5	1.51599(36)	1.5200(22)	2.0711(20)	42.5	1.69226(41)	1.6640(27)	2.3308(25)
47.5	1.38745(35)	1.3796(26)	1.8914(21)	47.5	1.49414(37)	1.4507(26)	2.0407(23)
52.5	1.25864(34)	1.2391(24)	1.7103(22)	52.5	1.31341(34)	1.2568(24)	1.7847(22)
57.5	1.13443(32)	1.0967(22)	1.5288(20)	57.5	1.15140(31)	1.0901(23)	1.5565(22)
62.5	1.01762(31)	0.9754(24)	1.3693(20)	62.5	1.00791(28)	0.9346(21)	1.3457(21)
67.5	0.91166(29)	0.8638(24)	1.2242(19)	67.5	0.88205(25)	0.8052(18)	1.1693(18)
72.5	0.81508(28)	0.7534(22)	1.0821(19)	72.5	0.77219(23)	0.6910(19)	1.0169(17)
77.5	0.72755(26)	0.6632(22)	0.9638(19)	77.5	0.67635(21)	0.5999(20)	0.8876(16)
82.5	0.65001(25)	0.5885(21)	0.8634(21)	82.5	0.59413(20)	0.5165(20)	0.7754(14)
87.5	0.58101(24)	0.5157(18)	0.7657(16)	87.5	0.52221(18)	0.4458(16)	0.6764(13)
92.5	0.51887(22)	0.4477(24)	0.6805(19)	92.5	0.45992(17)	0.3870(12)	0.5926(11)
97.5	0.46488(21)	0.3969(23)	0.6081(18)	97.5	0.40599(15)	0.3320(13)	0.5189(12)
102.5	0.41717(20)	0.3471(21)	0.5405(18)	102.5	0.35941(14)	0.2878(12)	0.4557(10)
107.5	0.37503(19)	0.3020(32)	0.4837(26)	107.5	0.31924(13)	0.2541(12)	0.40510(99)
112.5	0.33748(18)	0.2761(29)	0.4415(27)	112.5	0.28390(12)	0.2169(11)	0.35378(99)
117.5	0.30427(17)	0.2373(29)	0.3903(21)	117.5	0.25330(12)	0.1941(11)	0.31802(98)
122.5	0.27497(16)	0.2180(31)	0.3534(17)	122.5	0.22633(11)	0.1665(10)	0.27950(77)
127.5	0.24876(15)	0.1870(16)	0.3175(13)	127.5	0.20244(10)	0.1481(11)	0.24936(85)
132.5	0.22548(14)	0.1671(13)	0.2866(11)	132.5	0.181856(95)	0.13194(98)	0.22408(80)
137.5	0.20467(13)	0.1502(13)	0.2609(11)	137.5	0.163585(88)	0.11121(72)	0.19703(67)
142.5	0.18639(13)	0.1313(13)	0.2340(11)	142.5	0.147512(83)	0.10190(72)	0.17995(69)
147.5	0.16965(12)	0.1176(13)	0.2136(12)	147.5	0.133188(78)	0.08883(82)	0.16071(71)

Table 8: Distribution of η_{e^+} and η_{μ^-} at the LHC with $\mu = \mu_{ren} = \mu_{fact} = M_W$.

η_{μ^-}	$\frac{d\sigma_{LO}}{d\eta_{\mu^-}}$ [pb]	$\frac{d\sigma_{NLO,excl}}{d\eta_{\mu^-}}$ [pb]	$\frac{d\sigma_{NLO,incl}}{d\eta_{\mu^-}}$ [pb]	η_{e^+}	$\frac{d\sigma_{LO}}{d\eta_{e^+}}$ [pb]	$\frac{d\sigma_{NLO,excl}}{d\eta_{e^+}}$ [pb]	$\frac{d\sigma_{NLO,incl}}{d\eta_{e^+}}$ [pb]
−2.4	11.8284(58)	10.997(56)	15.461(42)	−2.4	13.6439(77)	12.462(66)	17.890(69)
−2.2	13.7789(61)	12.593(65)	18.033(73)	−2.2	15.4666(77)	14.058(74)	20.255(64)
−2	15.7736(63)	14.326(85)	20.574(48)	−2	17.1745(76)	15.362(55)	22.547(42)
−1.8	17.7086(66)	15.974(63)	23.258(51)	−1.8	18.7412(74)	16.866(62)	24.688(43)
−1.6	19.5103(68)	17.584(61)	25.653(47)	−1.6	20.1160(71)	17.900(69)	26.546(45)
−1.4	21.1445(70)	18.862(81)	27.866(51)	−1.4	21.3037(69)	18.923(73)	28.009(46)
−1.2	22.5806(71)	20.112(61)	29.951(46)	−1.2	22.3357(67)	19.83(11)	29.498(51)
−1	23.8165(72)	21.145(60)	31.538(41)	−1	23.1671(66)	20.620(60)	30.737(43)
−0.8	24.7995(72)	21.871(59)	32.946(38)	−0.8	23.8414(64)	21.168(77)	31.588(46)
−0.6	25.5677(72)	22.640(67)	34.059(41)	−0.6	24.3613(63)	21.733(51)	32.389(37)
−0.4	26.1199(72)	23.078(63)	34.710(41)	−0.4	24.7380(62)	22.134(64)	32.918(37)
−0.2	26.4622(73)	23.332(86)	35.232(50)	−0.2	24.9600(62)	22.213(67)	33.193(39)
0	26.5492(72)	23.442(54)	35.368(44)	0	25.0380(62)	22.397(68)	33.450(62)
0.2	26.4622(73)	23.457(80)	35.242(46)	0.2	24.9600(62)	22.253(68)	33.187(55)
0.4	26.1199(72)	23.089(64)	34.800(46)	0.4	24.7380(62)	22.121(65)	32.998(43)
0.6	25.5677(72)	22.662(67)	34.004(44)	0.6	24.3613(63)	21.697(53)	32.355(42)
0.8	24.7995(72)	21.937(70)	32.954(44)	0.8	23.8414(64)	21.189(65)	31.653(43)
1	23.8165(72)	21.132(65)	31.538(39)	1	23.1671(66)	20.550(56)	30.653(42)
1.2	22.5806(71)	20.187(66)	29.956(47)	1.2	22.3357(67)	19.716(90)	29.496(56)
1.4	21.1445(70)	18.763(72)	27.798(45)	1.4	21.3037(69)	18.996(73)	28.069(49)
1.6	19.5103(68)	17.552(66)	25.651(54)	1.6	20.1160(71)	17.926(64)	26.477(50)
1.8	17.7086(66)	16.061(68)	23.201(64)	1.8	18.7412(74)	16.845(66)	24.663(50)
2	15.7736(63)	14.322(84)	20.606(45)	2	17.1745(76)	15.363(57)	22.498(41)
2.2	13.7789(61)	12.597(68)	18.044(44)	2.2	15.4666(77)	13.978(67)	20.250(51)
2.4	11.8284(58)	11.051(47)	15.473(37)	2.4	13.6439(77)	12.439(67)	17.922(47)

$m_{e^+\mu^-}$ [GeV]	$\frac{d\sigma_{LO}}{dm_{e^+\mu^-}}\left[\frac{pb}{GeV}\right]$	$\frac{d\sigma_{NLO,excl}}{dm_{e^+\mu^-}}\left[\frac{pb}{GeV}\right]$	$\frac{d\sigma_{NLO,incl}}{dm_{e^+\mu^-}}\left[\frac{pb}{GeV}\right]$
5	0.013441(30)	0.01412(22)	0.01878(20)
15	0.139490(90)	0.13426(44)	0.18829(40)
25	0.24176(12)	0.22708(55)	0.32658(51)
35	0.32454(14)	0.30439(67)	0.43912(58)
45	0.40439(15)	0.38108(76)	0.54827(68)
55	0.50351(17)	0.48153(84)	0.68487(77)
65	0.60746(19)	0.5910(10)	0.82857(89)
75	0.68007(20)	0.6630(11)	0.92526(99)
85	0.70790(21)	0.68676(98)	0.95872(91)
95	0.69651(21)	0.6692(12)	0.9389(10)
105	0.65662(20)	0.6262(12)	0.8842(11)
115	0.60452(19)	0.5627(11)	0.8069(10)
125	0.54407(18)	0.5029(11)	0.72856(98)
135	0.48520(17)	0.4442(11)	0.64768(98)
145	0.42969(16)	0.3878(10)	0.57187(85)
155	0.37823(15)	0.3324(10)	0.49878(89)
165	0.33284(14)	0.29197(93)	0.44035(85)
175	0.29239(13)	0.25088(80)	0.38384(66)
185	0.25692(12)	0.21939(68)	0.33748(62)
195	0.22613(11)	0.18817(69)	0.29434(58)
205	0.19882(10)	0.16401(68)	0.25841(62)
215	0.175524(94)	0.14363(70)	0.22748(62)
225	0.155052(87)	0.12328(63)	0.19853(56)
235	0.137434(81)	0.10832(51)	0.17566(46)
245	0.121948(76)	0.09545(49)	0.15595(46)

η_{jet}	$\frac{d\sigma_{LO}}{d\eta_{jet}}$ [pb]	$\frac{d\sigma_{NLO,excl}}{d\eta_{jet}}$ [pb]	$\frac{d\sigma_{NLO,incl}}{d\eta_{jet}}$ [pb]
−4.32	0.15890(34)	0.2762(36)	0.3316(37)
−3.96	0.50253(69)	0.7129(77)	0.8899(75)
−3.6	1.1812(11)	1.463(16)	1.891(13)
−3.24	2.3948(16)	2.654(15)	3.574(14)
−2.88	4.3033(22)	4.382(22)	6.085(22)
−2.52	6.9684(29)	6.676(29)	9.489(26)
−2.16	10.3269(35)	9.476(34)	13.772(32)
−1.8	14.2214(41)	12.626(51)	18.683(44)
−1.44	18.2536(47)	16.030(49)	23.865(38)
−1.08	21.9552(52)	19.196(57)	28.692(41)
−0.72	24.9131(55)	21.607(62)	32.554(46)
−0.36	26.8378(57)	23.234(60)	34.975(43)
0	27.4891(58)	23.82(11)	35.877(60)
0.36	26.8378(57)	23.238(63)	35.063(54)
0.72	24.9131(55)	21.608(62)	32.531(49)
1.08	21.9552(52)	19.171(62)	28.672(39)
1.44	18.2536(47)	16.002(54)	23.846(46)
1.8	14.2214(41)	12.664(52)	18.653(51)
2.16	10.3269(35)	9.480(36)	13.773(32)
2.52	6.9684(29)	6.681(29)	9.502(23)
2.88	4.3033(22)	4.386(22)	6.085(18)
3.24	2.3948(16)	2.649(14)	3.575(13)
3.6	1.1812(11)	1.452(14)	1.888(13)
3.96	0.50253(69)	0.7123(76)	0.8883(67)
4.32	0.15890(34)	0.2760(35)	0.3309(35)

Table 9: Distribution of η_{jet} and $m_{e^+\mu^-}$ at the LHC with $\mu = \mu_{ren} = \mu_{fact} = M_W$.

Table 10: Distribution of $\cos\theta_{e^+\mu^-}$ and $\varphi_{e^+\mu^-}$ at the LHC with $\mu = \mu_{ren} = \mu_{fact} = M_W$.

$\varphi_{e^+\mu^-}$	$\frac{d\sigma_{LO}}{d\varphi_{e^+\mu^-}}$ [pb]	$\frac{d\sigma_{NLO,excl}}{d\varphi_{e^+\mu^-}}$ [pb]	$\frac{d\sigma_{NLO,incl}}{d\varphi_{e^+\mu^-}}$ [pb]
0.062831855	21.1649(87)	17.523(65)	28.681(51)
0.18849556	23.3692(90)	19.185(66)	31.436(52)
0.31415927	24.5298(93)	20.322(80)	33.167(58)
0.43982297	24.6116(92)	20.398(67)	33.105(55)
0.56548668	24.7017(94)	20.686(72)	33.341(59)
0.69115039	24.8908(93)	21.067(83)	33.678(58)
0.81681409	25.1940(94)	21.478(87)	34.057(70)
0.94247777	25.5753(95)	21.942(79)	34.515(67)
1.0681415	26.0338(97)	22.562(80)	35.248(80)
1.1938053	26.6636(98)	23.28(12)	36.045(66)
1.319469	27.3938(99)	24.404(96)	37.224(61)
1.4451327	28.293(10)	25.319(97)	38.249(66)
1.5707963	29.363(10)	26.56(13)	39.692(82)
1.69646	30.595(11)	27.62(10)	41.299(74)
1.8221238	32.037(11)	29.20(13)	43.273(86)
1.9477875	33.644(11)	30.99(14)	45.258(81)
2.0734512	35.538(11)	32.51(13)	47.443(84)
2.1991148	37.658(12)	34.63(14)	50.073(96)
2.3247785	39.973(12)	36.82(13)	52.736(97)
2.4504423	42.582(12)	39.30(14)	55.74(10)
2.5761059	45.274(13)	41.53(15)	58.68(11)
2.7017697	47.992(13)	43.90(15)	61.631(96)
2.8274333	50.626(13)	46.54(14)	64.58(13)
2.9530971	52.935(14)	48.63(15)	66.89(11)
3.0787608	54.506(14)	49.86(22)	68.44(11)

$\cos\theta_{e^+\mu^-}$	$\frac{d\sigma_{LO}}{d\cos\theta_{e^+\mu^-}}$ [pb]	$\frac{d\sigma_{NLO,excl}}{d\cos\theta_{e^+\mu^-}}$ [pb]	$\frac{d\sigma_{NLO,incl}}{d\cos\theta_{e^+\mu^-}}$ [pb]
−0.96	49.745(16)	48.56(13)	66.057(93)
−0.88	43.269(15)	41.75(16)	58.03(14)
−0.8	40.279(14)	38.59(14)	54.24(10)
−0.72	38.446(14)	36.85(23)	51.78(14)
−0.64	37.272(13)	35.21(20)	50.40(17)
−0.56	36.580(13)	34.52(16)	49.37(14)
−0.48	36.217(13)	33.49(20)	48.74(14)
−0.4	36.137(13)	33.93(22)	48.85(13)
−0.32	36.306(13)	33.55(17)	48.85(12)
−0.24	36.707(13)	33.78(17)	49.43(13)
−0.16	37.307(14)	33.87(19)	50.07(12)
−0.08	38.142(14)	34.87(23)	51.31(15)
0	39.220(14)	35.49(22)	52.32(13)
0.08	40.626(14)	36.29(24)	53.91(15)
0.16	42.353(15)	37.99(16)	56.45(12)
0.24	44.441(15)	39.50(18)	58.95(12)
0.32	47.056(16)	42.28(28)	62.46(13)
0.4	50.318(16)	44.80(18)	66.58(11)
0.48	54.494(17)	47.72(18)	71.83(12)
0.56	59.959(18)	52.68(22)	78.87(18)
0.64	67.158(20)	58.82(19)	88.13(17)
0.72	77.089(22)	67.12(18)	100.91(14)
0.8	91.694(24)	78.82(25)	118.88(18)
0.88	112.407(28)	95.56(19)	145.38(14)
0.96	118.601(28)	96.50(17)	153.08(17)

Table 11: Distribution of $p_{T,jet}$ and $p_{T,miss}$ at the Tevatron with $\mu = \mu_{ren} = \mu_{fact} = M_W$.

$p_{T,miss}$[GeV]	$\frac{d\sigma_{LO}}{dp_{T,miss}}\left[\frac{pb}{GeV}\right]$	$\frac{d\sigma_{NLO,excl}}{dp_{T,miss}}\left[\frac{pb}{GeV}\right]$	$\frac{d\sigma_{NLO,incl}}{dp_{T,miss}}\left[\frac{pb}{GeV}\right]$
27.5	0.22486(12)	0.26071(41)	0.29070(40)
32.5	0.22916(12)	0.26346(38)	0.29475(38)
37.5	0.22730(12)	0.25967(42)	0.29130(41)
42.5	0.21985(11)	0.25002(38)	0.28133(36)
47.5	0.20813(11)	0.23658(42)	0.26677(42)
52.5	0.19202(10)	0.21661(33)	0.24525(33)
57.5	0.172431(93)	0.19402(36)	0.22024(35)
62.5	0.150144(84)	0.16747(28)	0.19098(28)
67.5	0.126317(75)	0.13992(24)	0.16047(25)
72.5	0.102584(65)	0.11164(24)	0.12928(25)
77.5	0.081294(56)	0.08633(21)	0.10102(20)
82.5	0.062423(47)	0.06500(21)	0.07693(19)
87.5	0.045999(38)	0.04640(14)	0.05614(13)
92.5	0.032865(30)	0.031666(87)	0.039498(86)
97.5	0.023546(23)	0.021567(68)	0.027789(68)
102.5	0.017363(19)	0.014919(50)	0.019946(52)
107.5	0.013125(16)	0.010781(42)	0.014759(40)
112.5	0.010179(14)	0.007943(40)	0.011207(34)
117.5	0.007999(12)	0.006024(30)	0.008648(30)
122.5	0.006360(10)	0.004588(26)	0.006727(26)
127.5	0.0051262(87)	0.003589(36)	0.005334(35)
132.5	0.0041637(78)	0.002807(18)	0.004260(17)
137.5	0.0034107(68)	0.002229(17)	0.003421(17)
142.5	0.0028220(62)	0.001784(15)	0.002783(14)
147.5	0.0023492(55)	0.001410(14)	0.002263(13)

$p_{T,jet}$[GeV]	$\frac{d\sigma_{LO}}{dp_{T,jet}}\left[\frac{pb}{GeV}\right]$	$\frac{d\sigma_{NLO,excl}}{dp_{T,jet}}\left[\frac{pb}{GeV}\right]$	$\frac{d\sigma_{NLO,incl}}{dp_{T,jet}}\left[\frac{pb}{GeV}\right]$
25	0.38977(12)	0.49226(78)	0.51143(76)
35	0.214392(77)	0.25162(56)	0.28034(60)
45	0.133866(56)	0.14689(38)	0.17183(41)
55	0.089710(43)	0.09317(33)	0.11298(29)
65	0.063002(34)	0.06205(22)	0.07802(20)
75	0.045775(28)	0.04275(21)	0.05562(18)
85	0.034102(23)	0.03022(16)	0.04059(14)
95	0.025834(19)	0.02171(20)	0.02992(13)
105	0.019880(16)	0.01599(11)	0.02268(13)
115	0.015488(14)	0.01182(10)	0.01727(11)
125	0.012117(12)	0.009083(79)	0.013355(82)
135	0.009580(10)	0.006684(69)	0.010184(72)
145	0.0075986(91)	0.005089(91)	0.007916(67)
155	0.0060508(79)	0.004025(52)	0.006279(38)
165	0.0048493(69)	0.002966(56)	0.004837(49)
175	0.0038996(61)	0.002313(35)	0.003824(34)
185	0.0031335(53)	0.001824(38)	0.003053(36)
195	0.0025325(47)	0.001419(38)	0.002369(30)
205	0.0020389(41)	0.000985(62)	0.001861(43)
215	0.0016544(36)	0.000903(30)	0.001537(37)
225	0.0013444(32)	0.000639(17)	0.001148(17)
235	0.0010868(28)	0.000527(13)	0.000950(14)
245	0.0008872(25)	0.000398(14)	0.000729(14)
255	0.0007201(21)	0.000306(18)	0.000580(19)
265	0.0005831(19)	0.000256(13)	0.000473(13)

Table 12: Distribution of p_{T,e^+} and p_{T,μ^-} at the Tevatron with $\mu = \mu_{ren} = \mu_{fact} = M_W$.

p_{T,μ^-} [GeV]	$\frac{d\sigma_{LO}}{dp_{T,\mu^-}}\left[\frac{pb}{GeV}\right]$	$\frac{d\sigma_{NLO,excl}}{dp_{T,\mu^-}}\left[\frac{pb}{GeV}\right]$	$\frac{d\sigma_{NLO,incl}}{dp_{T,\mu^-}}\left[\frac{pb}{GeV}\right]$
27.5	0.30973(16)	0.35406(48)	0.39974(48)
32.5	0.30491(14)	0.35174(44)	0.39591(45)
37.5	0.27515(13)	0.31884(49)	0.35935(49)
42.5	0.23554(11)	0.26988(49)	0.30501(47)
47.5	0.195422(96)	0.22188(45)	0.25183(43)
52.5	0.159132(84)	0.17840(26)	0.20373(26)
57.5	0.128552(74)	0.14200(28)	0.16308(26)
62.5	0.103607(65)	0.11224(22)	0.12977(23)
67.5	0.083574(58)	0.08928(25)	0.10379(27)
72.5	0.067426(51)	0.07061(24)	0.08269(25)
77.5	0.054683(45)	0.05642(16)	0.06644(16)
82.5	0.044524(40)	0.04495(15)	0.05324(13)
87.5	0.036523(36)	0.03607(23)	0.04300(20)
92.5	0.029974(32)	0.02967(22)	0.03551(21)
97.5	0.024674(29)	0.023881(94)	0.028747(94)
102.5	0.020515(26)	0.019219(88)	0.023307(87)
107.5	0.017003(23)	0.015744(86)	0.019181(86)
112.5	0.014195(21)	0.012863(68)	0.015729(67)
117.5	0.011881(19)	0.010706(63)	0.013152(64)
122.5	0.009974(17)	0.008755(49)	0.010832(52)
127.5	0.008367(16)	0.007244(48)	0.009042(53)
132.5	0.007092(14)	0.006093(39)	0.007605(39)
137.5	0.006007(13)	0.004931(36)	0.006200(36)
142.5	0.005081(12)	0.004208(33)	0.005308(36)
147.5	0.004332(11)	0.003622(38)	0.004554(39)

p_{T,e^+} [GeV]	$\frac{d\sigma_{LO}}{dp_{T,e^+}}\left[\frac{pb}{GeV}\right]$	$\frac{d\sigma_{NLO,excl}}{dp_{T,e^+}}\left[\frac{pb}{GeV}\right]$	$\frac{d\sigma_{NLO,incl}}{dp_{T,e^+}}\left[\frac{pb}{GeV}\right]$
27.5	0.30969(16)	0.35540(53)	0.40097(53)
32.5	0.30476(14)	0.35176(47)	0.39624(46)
37.5	0.27514(12)	0.31748(41)	0.35780(41)
42.5	0.23547(11)	0.27055(38)	0.30585(37)
47.5	0.195342(96)	0.22209(32)	0.25213(33)
52.5	0.159304(85)	0.17864(32)	0.20402(31)
57.5	0.128438(74)	0.14141(25)	0.16253(25)
62.5	0.103669(66)	0.11270(25)	0.13015(23)
67.5	0.083655(58)	0.08918(20)	0.10373(19)
72.5	0.067429(51)	0.07026(24)	0.08238(26)
77.5	0.054722(46)	0.05676(21)	0.06667(20)
82.5	0.044628(41)	0.04505(14)	0.05339(14)
87.5	0.036517(36)	0.03602(11)	0.04290(11)
92.5	0.029963(33)	0.02940(10)	0.03518(10)
97.5	0.024763(29)	0.02358(10)	0.028413(98)
102.5	0.020480(26)	0.019326(99)	0.023401(98)
107.5	0.017023(24)	0.015724(80)	0.019199(83)
112.5	0.014164(21)	0.012928(72)	0.015834(66)
117.5	0.011861(19)	0.010682(67)	0.013163(68)
122.5	0.009959(17)	0.008731(52)	0.010833(52)
127.5	0.008412(16)	0.007133(66)	0.008860(68)
132.5	0.007077(14)	0.006146(67)	0.007656(66)
137.5	0.006009(13)	0.005094(46)	0.006365(45)
142.5	0.005095(12)	0.004191(34)	0.005288(33)
147.5	0.004309(11)	0.003517(34)	0.004450(34)

Table 13: Distribution of η_{e^+} and η_{μ^-} at the Tevatron with $\mu = \mu_{ren} = \mu_{fact} = M_W$.

η_{μ^-}	$\frac{d\sigma_{LO}}{d\eta_{\mu^-}}$ [pb]	$\frac{d\sigma_{NLO,excl}}{d\eta_{\mu^-}}$ [pb]	$\frac{d\sigma_{NLO,incl}}{d\eta_{\mu^-}}$ [pb]	η_{e^+}	$\frac{d\sigma_{LO}}{d\eta_{e^+}}$ [pb]	$\frac{d\sigma_{NLO,excl}}{d\eta_{e^+}}$ [pb]	$\frac{d\sigma_{NLO,incl}}{d\eta_{e^+}}$ [pb]
−2.4	0.27168(42)	0.3040(16)	0.3409(16)	−2.4	0.27124(43)	0.3139(20)	0.3443(19)
−2.2	0.46828(63)	0.5228(60)	0.5895(62)	−2.2	0.43757(56)	0.5046(25)	0.5550(25)
−2	0.74839(87)	0.8256(40)	0.9343(40)	−2	0.66082(71)	0.7610(37)	0.8416(33)
−1.8	1.1136(11)	1.2392(57)	1.4061(57)	−1.8	0.94463(87)	1.0770(39)	1.1947(39)
−1.6	1.5503(15)	1.6979(98)	1.948(10)	−1.6	1.2805(10)	1.4555(44)	1.6258(44)
−1.4	2.0437(17)	2.2547(85)	2.5763(89)	−1.4	1.6640(12)	1.8749(53)	2.1066(53)
−1.2	2.5502(20)	2.8151(98)	3.218(10)	−1.2	2.0764(14)	2.3277(59)	2.6312(62)
−1	3.0353(22)	3.3262(83)	3.8198(86)	−1	2.4991(16)	2.7865(63)	3.1675(63)
−0.8	3.4528(24)	3.782(13)	4.367(12)	−0.8	2.9163(17)	3.2388(74)	3.6926(85)
−0.6	3.7761(25)	4.130(12)	4.768(10)	−0.6	3.2962(19)	3.6422(73)	4.1724(88)
−0.4	3.9845(25)	4.345(12)	5.019(12)	−0.4	3.6215(21)	3.9869(91)	4.5880(85)
−0.2	4.0658(25)	4.442(12)	5.135(12)	−0.2	3.8654(23)	4.2419(91)	4.8908(88)
0	4.0259(24)	4.4000(97)	5.0760(97)	0	4.0231(24)	4.397(11)	5.082(11)
0.2	3.8716(23)	4.244(12)	4.903(12)	0.2	4.0651(25)	4.4434(96)	5.1421(99)
0.4	3.6187(21)	3.9915(95)	4.583(10)	0.4	3.9837(25)	4.335(10)	5.025(10)
0.6	3.2972(19)	3.6443(82)	4.1792(86)	0.6	3.7760(25)	4.133(15)	4.776(15)
0.8	2.9122(17)	3.2341(71)	3.6921(68)	0.8	3.4522(24)	3.788(10)	4.364(10)
1	2.5006(15)	2.7948(62)	3.1792(64)	1	3.0365(22)	3.3306(98)	3.8285(93)
1.2	2.0766(13)	2.3340(57)	2.6390(58)	1.2	2.5526(20)	2.812(14)	3.213(12)
1.4	1.6645(12)	1.8748(68)	2.1021(68)	1.4	2.0468(17)	2.2697(98)	2.5971(95)
1.6	1.2817(10)	1.4585(44)	1.6349(48)	1.6	1.5535(14)	1.7213(84)	1.9599(84)
1.8	0.94199(84)	1.0699(34)	1.1884(33)	1.8	1.1129(11)	1.2313(55)	1.3990(55)
2	0.66057(69)	0.7577(31)	0.8373(31)	2	0.74748(84)	0.8308(60)	0.9351(55)
2.2	0.43742(55)	0.5046(26)	0.5544(27)	2.2	0.46781(60)	0.5242(31)	0.5901(30)
2.4	0.27079(42)	0.3175(21)	0.3468(21)	2.4	0.27187(41)	0.3043(17)	0.3419(17)

Table 14: Distribution of η_{jet} and $m_{e^+\mu^-}$ at the Tevatron with $\mu = \mu_{\text{ren}} = \mu_{\text{fact}} = M_W$.

$m_{e^+\mu^-}$ [GeV]	$\frac{d\sigma_{\text{LO}}}{dm_{e^+\mu^-}}\left[\frac{\text{pb}}{\text{GeV}}\right]$	$\frac{d\sigma_{\text{NLO,excl}}}{dm_{e^+\mu^-}}\left[\frac{\text{pb}}{\text{GeV}}\right]$	$\frac{d\sigma_{\text{NLO,incl}}}{dm_{e^+\mu^-}}\left[\frac{\text{pb}}{\text{GeV}}\right]$
5	0.002587(10)	0.003042(64)	0.003389(59)
15	0.016720(24)	0.018743(67)	0.021646(66)
25	0.028051(32)	0.031663(92)	0.036463(91)
35	0.039593(38)	0.04497(12)	0.05156(12)
45	0.052892(45)	0.06066(14)	0.06926(14)
55	0.073373(54)	0.08432(17)	0.09572(17)
65	0.093311(59)	0.10709(21)	0.12126(21)
75	0.100353(59)	0.11545(21)	0.13094(21)
85	0.096957(56)	0.11012(20)	0.12545(20)
95	0.087873(51)	0.09854(19)	0.11277(19)
105	0.076902(46)	0.08558(16)	0.09817(16)
115	0.065851(41)	0.07263(16)	0.08357(16)
125	0.055874(37)	0.06115(13)	0.07047(13)
135	0.047015(33)	0.05058(14)	0.05842(14)
145	0.039484(30)	0.04268(16)	0.04919(15)
155	0.033171(27)	0.03519(12)	0.04060(12)
165	0.027827(25)	0.029571(97)	0.034151(97)
175	0.023336(23)	0.024458(88)	0.028257(87)
185	0.019641(21)	0.02064(11)	0.02381(11)
195	0.016627(19)	0.017056(93)	0.019698(93)
205	0.013979(18)	0.014438(92)	0.016646(91)
215	0.011843(16)	0.011997(72)	0.013844(69)
225	0.010019(15)	0.010061(62)	0.011623(63)
235	0.008489(14)	0.008514(58)	0.009808(58)
245	0.007250(13)	0.007370(52)	0.008465(52)

η_{jet}	$\frac{d\sigma_{\text{LO}}}{d\eta_{\text{jet}}}$ [pb]	$\frac{d\sigma_{\text{NLO,excl}}}{d\eta_{\text{jet}}}$ [pb]	$\frac{d\sigma_{\text{NLO,incl}}}{d\eta_{\text{jet}}}$ [pb]
−2.4	0.57315(68)	0.6833(78)	0.7509(86)
−2.2	0.78791(83)	0.901(11)	1.005(11)
−2	1.0390(10)	1.221(16)	1.346(16)
−1.8	1.3276(12)	1.533(19)	1.711(13)
−1.6	1.6330(13)	1.866(18)	2.083(13)
−1.4	1.9453(15)	2.166(14)	2.483(15)
−1.2	2.2666(17)	2.523(13)	2.875(14)
−1	2.5753(18)	2.815(15)	3.218(17)
−0.8	2.8418(19)	3.072(15)	3.572(16)
−0.6	3.0669(20)	3.326(20)	3.838(24)
−0.4	3.2377(21)	3.488(25)	4.097(32)
−0.2	3.3455(21)	3.592(25)	4.174(19)
0	3.3903(22)	3.630(28)	4.219(21)
0.2	3.3544(22)	3.586(21)	4.191(18)
0.4	3.2405(22)	3.482(18)	4.070(19)
0.6	3.0610(21)	3.307(17)	3.829(18)
0.8	2.8506(21)	3.111(20)	3.582(21)
1	2.5775(19)	2.816(17)	3.240(17)
1.2	2.2677(18)	2.480(19)	2.841(17)
1.4	1.9445(16)	2.180(16)	2.482(16)
1.6	1.6339(15)	1.833(13)	2.086(13)
1.8	1.3294(13)	1.516(12)	1.700(13)
2	1.0412(11)	1.195(13)	1.338(11)
2.2	0.78676(95)	0.9427(94)	1.0262(85)
2.4	0.57316(77)	0.6867(89)	0.7516(84)

Table 15: Distribution of $\cos\theta_{e^+\mu^-}$ and $\varphi_{e^+\mu^-}$ at the Tevatron with $\mu = \mu_{ren} = \mu_{fact} = M_W$.

$\varphi_{e^+\mu^-}$	$\frac{d\sigma_{LO}}{d\varphi_{e^+\mu^-}}$ [pb]	$\frac{d\sigma_{NLO,excl}}{d\varphi_{e^+\mu^-}}$ [pb]	$\frac{d\sigma_{NLO,incl}}{d\varphi_{e^+\mu^-}}$ [pb]
0.062831855	1.5811(19)	1.7284(86)	2.0408(86)
0.18849556	1.7229(20)	1.8614(80)	2.2075(80)
0.31415927	1.8202(20)	1.9833(98)	2.340(10)
0.43982297	1.8724(21)	2.036(14)	2.405(13)
0.56548668	1.9321(21)	2.1060(73)	2.4815(72)
0.69115039	2.0126(21)	2.2103(85)	2.5944(84)
0.81681409	2.1161(22)	2.3300(99)	2.719(10)
0.94247777	2.2367(22)	2.4762(94)	2.8831(90)
1.0681415	2.3776(23)	2.6276(98)	3.048(10)
1.1938053	2.5414(23)	2.8411(95)	3.2849(99)
1.319469	2.7318(24)	3.0415(96)	3.5011(98)
1.4451327	2.9411(26)	3.299(11)	3.782(11)
1.5707963	3.1711(26)	3.584(20)	4.082(18)
1.69646	3.4213(27)	3.850(11)	4.394(11)
1.8221238	3.6860(27)	4.135(12)	4.710(11)
1.9477875	3.9508(28)	4.436(12)	5.052(12)
2.0734512	4.2263(29)	4.722(12)	5.368(11)
2.1991148	4.5080(30)	5.053(15)	5.727(15)
2.3247785	4.7721(31)	5.309(12)	6.023(12)
2.4504423	5.0090(32)	5.540(12)	6.288(13)
2.5761059	5.2482(33)	5.821(14)	6.590(14)
2.7017697	5.4610(34)	5.983(13)	6.782(13)
2.8274333	5.6843(34)	6.205(12)	7.041(12)
2.9530971	5.9002(35)	6.390(13)	7.240(12)
3.0787608	6.0086(36)	6.479(12)	7.339(12)

$\cos\theta_{e^+\mu^-}$	$\frac{d\sigma_{LO}}{d\cos\theta_{e^+\mu^-}}$ [pb]	$\frac{d\sigma_{NLO,excl}}{d\cos\theta_{e^+\mu^-}}$ [pb]	$\frac{d\sigma_{NLO,incl}}{d\cos\theta_{e^+\mu^-}}$ [pb]
−0.96	8.9561(59)	9.712(22)	10.986(21)
−0.88	8.0391(55)	8.789(26)	9.964(23)
−0.8	7.4532(53)	8.214(24)	9.309(27)
−0.72	7.0061(50)	7.726(29)	8.794(26)
−0.64	6.6385(49)	7.319(24)	8.324(23)
−0.56	6.3402(47)	7.054(26)	8.024(29)
−0.48	6.0737(46)	6.717(33)	7.674(30)
−0.4	5.8496(45)	6.478(33)	7.353(32)
−0.32	5.6578(44)	6.269(21)	7.179(22)
−0.24	5.4969(44)	6.139(31)	7.015(29)
−0.16	5.3424(43)	5.932(37)	6.787(31)
−0.08	5.2193(42)	5.801(29)	6.658(26)
0	5.0918(41)	5.647(20)	6.489(25)
0.08	4.9873(40)	5.577(34)	6.387(34)
0.16	4.9043(40)	5.447(23)	6.256(22)
0.24	4.8156(39)	5.350(30)	6.168(30)
0.32	4.7384(38)	5.249(21)	6.041(21)
0.4	4.6672(37)	5.175(18)	5.955(18)
0.48	4.5956(36)	5.078(22)	5.847(21)
0.56	4.5262(36)	5.003(18)	5.764(19)
0.64	4.4354(35)	4.905(18)	5.663(19)
0.72	4.3315(34)	4.780(20)	5.534(23)
0.8	4.1823(32)	4.581(16)	5.311(16)
0.88	3.9323(31)	4.308(13)	5.018(13)
0.96	3.2732(27)	3.539(12)	4.151(12)

[9] S. Dittmaier, S. Kallweit and P. Uwer, Phys. Rev. Lett. **100** (2008) 062003 [arXiv:0710.1577 [hep-ph]].

[10] J. M. Campbell, R. Keith Ellis and G. Zanderighi, JHEP **0712** (2007) 056 [arXiv:0710.1832 [hep-ph]].

[11] G. Sanguinetti and S. Karg, arXiv:0806.1394 [hep-ph];
T. Binoth, J.-P. Guillet, S. Karg, N. Kauer and G. Sanguinetti, in preparation.

[12] T. Kobayashi, Prog. Theor. Phys. **49** (1973) 282.

[13] N. Cabibbo, Phys. Rev. Lett. **10** (1963) 531.

[14] C. Neu [CDF Collaboration], FERMILAB-CONF-06-162-E.

[15] K. Hanagaki [D0 Collaboration], FERMILAB-CONF-05-647-E.

[16] T. Wright [CDF and D0 Collaboration], arXiv:0707.1712 [hep-ex].

[17] A. Wildauer and F. Akesson, in "Interlaken 2004, Computing in high energy physics and nuclear physics," 419-422.

[18] M. Lehmacher, arXiv:0809.4896 [hep-ex].

[19] A. Denner, S. Dittmaier, M. Roth and D. Wackeroth, Nucl. Phys. B **560** (1999) 33 [arXiv:hep-ph/9904472].

[20] A. Denner, S. Dittmaier, M. Roth and L. H. Wieders, Nucl. Phys. B **724** (2005) 247 [arXiv:hep-ph/0505042].

[21] A. Brandenburg and P. Uwer, Nucl. Phys. B **515**, 279 (1998) [arXiv:hep-ph/9708350].

[22] A. Banfi, G. P. Salam and G. Zanderighi, Eur. Phys. J. C **47** (2006) 113 [arXiv:hep-ph/0601139].

[23] W. Beenakker, S. Dittmaier, M. Krämer, B. Plümper, M. Spira and P. M. Zerwas, Nucl. Phys. B **653** (2003) 151 [arXiv:hep-ph/0211352].

[24] S. Dittmaier, P. Uwer and S. Weinzierl, Phys. Rev. Lett. **98** (2007) 262002 [arXiv:hep-ph/0703120] and Eur. Phys. J. C **59** (2009) 625 [arXiv:0810.0452 [hep-ph]].

[25] J. Küblbeck, M. Böhm and A. Denner, Comput. Phys. Commun. **60** (1990) 165.

[26] S. Dittmaier, Nucl. Phys. B **675** (2003) 447 [arXiv:hep-ph/0308246].

[27] A. Denner and S. Dittmaier, Nucl. Phys. B **658** (2003) 175 [arXiv:hep-ph/0212259].

[28] G. Passarino and M. J. G. Veltman, Nucl. Phys. B **160** (1979) 151.

[29] G. 't Hooft and M. J. G. Veltman, Nucl. Phys. B **153**, 365 (1979).

[30] W. Beenakker and A. Denner, Nucl. Phys. B **338** (1990) 349.

[31] A. Denner, U. Nierste and R. Scharf, Nucl. Phys. B **367**, 637 (1991).

[32] A. Denner and S. Dittmaier, Nucl. Phys. B **734**, 62 (2006) [arXiv:hep-ph/0509141].

[33] T. Binoth, J. P. Guillet, G. Heinrich, E. Pilon and C. Schubert, JHEP **0510** (2005) 015 [arXiv:hep-ph/0504267].

[34] W. Giele, E. W. N. Glover and G. Zanderighi, Nucl. Phys. Proc. Suppl. **135** (2004) 275 [arXiv:hep-ph/0407016];
R. K. Ellis, W. T. Giele and G. Zanderighi, Phys. Rev. D **73** (2006) 014027 [arXiv:hep-ph/0508308].

[35] T. Hahn, Comput. Phys. Commun. **140** (2001) 418 [arXiv:hep-ph/0012260].

[36] T. Hahn and M. Perez-Victoria, Comput. Phys. Commun. **118** (1999) 153 [arXiv:hep-ph/9807565].

[37] G. J. van Oldenborgh and J. A. M. Vermaseren, Z. Phys. C **46**, 425 (1990).

[38] G. J. van Oldenborgh, Comput. Phys. Commun. **66** (1991)

[39] Z. Bern, L. J. Dixon and D. A. Kosower, Nucl. Phys. B **412** (1994) 751 [arXiv:hep-ph/9306240].

[40] G. 't Hooft and M. J. G. Veltman, Nucl. Phys. B **44** (1972) 189;
P. Breitenlohner and D. Maison, Commun. Math. Phys. **52** (1977) 39.

[41] F. Jegerlehner, Eur. Phys. J. C **18** (2001) 673 [arXiv:hep-th/0005255].

[42] S. Catani and M. H. Seymour, Nucl. Phys. B **485** (1997) 291 [Erratum-ibid. B **510** (1998) 503] [arXiv:hep-ph/9605323].

[43] S. Dittmaier, Phys. Rev. D **59** (1999) 016007 [arXiv:hep-ph/9805445].

[44] F. A. Berends, R. Pittau and R. Kleiss, Nucl. Phys. B **424** (1994) 308 [arXiv:hep-ph/9404313].

[45] R. Kleiss and R. Pittau, Comput. Phys. Commun. **83**, 141 (1994) [arXiv:hep-ph/9405257].

[46] M. Roth, doctoral thesis, DISS-ETH-13363, 1999, arXiv:hep-ph/0008033.

[47] W. Kilian, T. Ohl and J. Reuter, arXiv:0708.4233 [hep-ph].

[48] T. Gleisberg, S. Höche, F. Krauss, A. Schälicke, S. Schumann and J. C. Winter, JHEP **0402** (2004) 056 [arXiv:hep-ph/0311263].

[49] S. Kallweit, diploma thesis (in German), LMU Munich, 2006.

[50] T. Stelzer and W. F. Long, Comput. Phys. Commun. **81** (1994) 357 [arXiv:hep-ph/9401258].

[51] S. Eidelman *et al.* [Particle Data Group], Phys. Lett. B **592** (2004) 1.

[52] A. Djouadi, J. Kalinowski and M. Spira, Comput. Phys. Commun. **108** (1998) 56 [hep-ph/9704448].

[53] S. Dittmaier and M. Krämer, Phys. Rev. D **65** (2002) 073007 [arXiv:hep-ph/0109062].

[54] C. Amsler *et al.* [Particle Data Group], Phys. Lett. B **667** (2008) 1.

[55] S. Dittmaier, S. Kallweit and P. Uwer, PoS **RADCOR2007** (2007) 009 [arXiv:0712.3163 [hep-ph]].

[56] S. Dittmaier, S. Kallweit and P. Uwer, Nucl. Phys. Proc. Suppl. **183** (2008) 279 [arXiv:0807.0708 [hep-ph]].

[57] R. K. Ellis, W. J. Stirling, B. R. Webber, "QCD and Collider Physics," *Cambridge University Press, 1996*.

[58] J. Pumplin, D. R. Stump, J. Huston, H. L. Lai, P. Nadolsky and W. K. Tung, JHEP **0207** (2002) 012 [arXiv:hep-ph/0201195].

[59] D. Stump, J. Huston, J. Pumplin, W. K. Tung, H. L. Lai, S. Kuhlmann and J. F. Owens, JHEP **0310** (2003) 046 [arXiv:hep-ph/0303013].

[60] A. D. Martin, W. J. Stirling and R. S. Thorne, Phys. Lett. B **636** (2006) 259 [arXiv:hep-ph/0603143].

[61] S. D. Ellis and D. E. Soper, Phys. Rev. D **48** (1993) 3160 [arXiv:hep-ph/9305266].

[62] L. J. Dixon, Z. Kunszt and A. Signer, Phys. Rev. D **60** (1999) 114037 [arXiv:hep-ph/9907305].

[63] M. Dittmar and H. K. Dreiner, arXiv:hep-ph/9703401.